Microextrusion 3D-Printing of Solid Oxide Fuel Cell Components

by

Feroze Khan Baderuddin

Submitted in Partial Fulfillment of the Requirements

for the Degree of

Doctor of Philosophy
in the

Materials Science and Engineering

Program

YOUNGSTOWN STATE UNIVERSITY

December, 2016

Microextrusion 3D-Printing of Solid Oxide Fuel Cell Components

Feroze Khan Baderuddin

I hereby release this dissertation to the public. I understand that this dissertation will be made available from the OhioLINK ETD Center and the Maag Library Circulation Desk for public access. I also authorize the University or other individuals to make copies of this dissertation as needed for scholarly research.

Signature:

Feroze Khan Baderuddin, Student Date

Approvals:

Clovis A. Linkous, Dissertation Advisor Date

Dr. Sherri Lovelace-Cameron, Committee Member Date

Dr. Tim Wagner, Committee Member Date

Dr. Guha Manogharan, Committee Member Date

Dr. Brett Conner, Committee Member Date

Dr. Salvatore A. Sanders, Dean of Graduate Studies Date

ABSTRACT

The aim of this research was to investigate microextrusion 3d printing which is a type of Additive Manufacturing (AM) technique for the fabrication of a solid oxide fuel cell.

The solid oxide fuel cell or SOFC is a fuel cell for which the electrolyte consists of an O^{2-}-conducting metal oxide. They have proven to be an efficient and cost effective method for conversion for a wide variety of fuels such as hydrocarbons, coal gas and gasified carbonaceous solids into electricity. An SOFC typically is operated from around 600-1000 ^{0}C, hence, its needed to be made of ceramic components. Current ceramic technologies of fabrication limit SOFC design options and ultimate efficiencies. On the other hand, 3D printing technology enables intricate geometries which could provide higher levels of performance. An SOFC consists of three main components: electrolyte, cathode and an anode. The respective materials of choice were 8%Y_2O_3-ZrO_2 (YSZ), Sr-doped $LaMnO_3$ blended with 50 % YSZ and (40%)Ni/(60%)YSZ cermet. Paste formulations were prepared for each of the SOFC components and test disks or buttons were 3d printed. Various printed layers of an SOFC were evaluated according to ionic conductivity, electronic conductivity, gas permeability, density and shrinkage. By varying the compositions of the pastes according to particle size, binder ratio and solvent paste viscosity and consistency was controlled.

The formulation pastes of all the components of the SOFC were designed to achieve uniform shrinkage upon cosintering at 1300 °C. The functionality of the 3d printed fuel cell was demonstrated by testing its galvanic performance and the microstructure was verified under an SEM.

Acknowledgements

First of all, I would like to thank my supervisor Professor Clovis Linkous for his active support, advice and guidance to complete this project.

I am very grateful to Dr. Timothy R.Wagner and Dr. Sanders for their support and advice throughout my stay at Youngstown State University.

I want to thank Dr. Brett Conner and Dr. Sherri Lovelace-Cameron for serving on my thesis committee.

I am also very grateful to Dr. Choi at Akron University for allowing me to use the equipment in his research lab without him this research project would not have been possible.

I want to acknowledge Raymond E. Hoff, Dr. Dingqiang Li and John Dodson for their help with instrumentation and equipment.

Lastly, I would like to express my gratitude to my family members and parents for their active support and encouragement to complete this project.

Table of Contents

List of figures

List of tables

CHAPTER 1

INTRODUCTION

1.1 ENERGY CRISIS

Every day the need for energy surges due to the increase in population and with limited resources, there is an immediate need to find an energy resource that is renewable and at the same time can fulfill the energy demands of our world. Most of the world's energy comes from our already depleted natural resources (Figure 1.1)

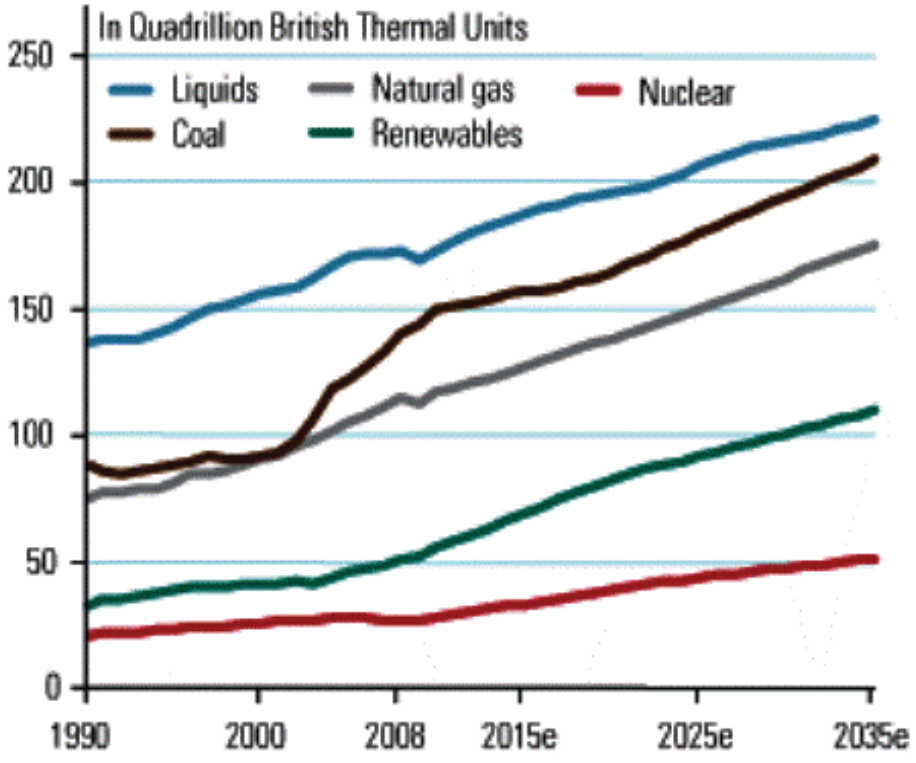

Figure 2.1 World electrical energy consumption by fuel type, 1990 – 2035[1]

Fossil fuels will remain our main sources of energy in the near future but our dependency on them will have to be reduced. Earlier studies had showed that oil would last until

about 2050, but a team from Sweden's University of Uppsala believes that total world's reserves are 80 percent less than are predicted to be. The Uppsala team suggested that the amount of oil and gas left in our reserves is the equivalent of around 3,500 billion barrels of oil, but the IPCC (Intergovernmental Panel on Climate Change) disagrees and projects it to be between 5,000 and 18,000 billion barrels. Regardless, non-fossil fuels must arrive much earlier than was anticipated [2].

The total global energy investment reached $1.8 trillion in 2015 (Figure 1.2). The focus on investing towards low carbon sources of energy also grew in 2015 as $313 billion went towards alternative forms of energy such as solar, wind and geothermal.

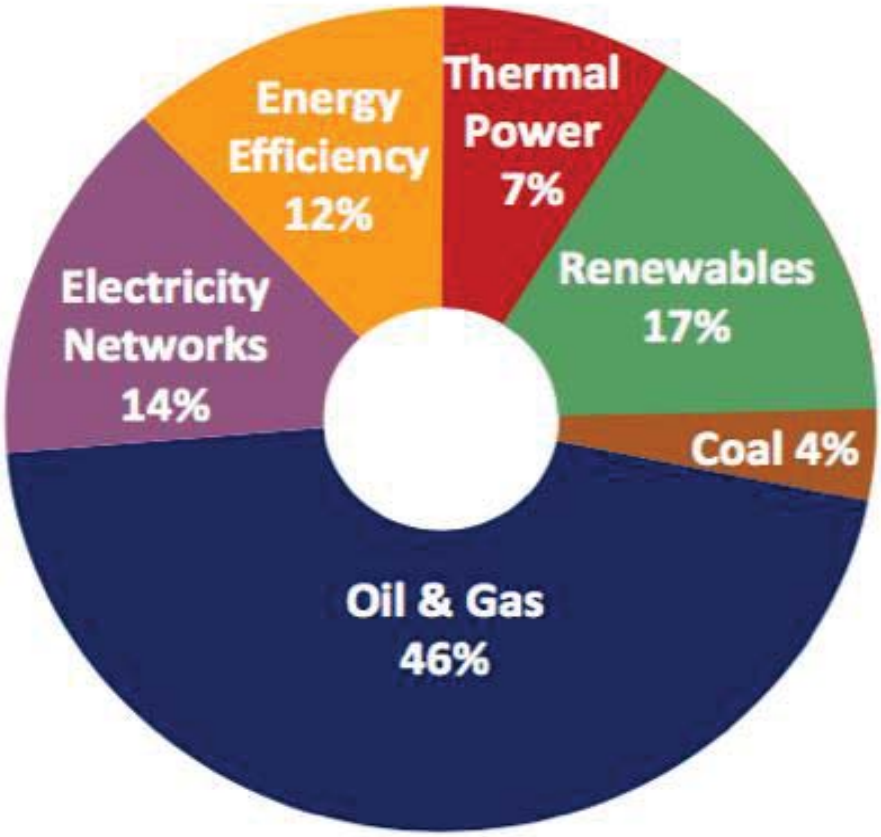

Figure 1.2 World energy investments in 2015 [3]

$ 221 billion was invested in increasing the energy efficiency technologies such as fuel cells. When it comes to energy, the main concern is electricity. Today, almost everything runs on electricity as it accounts for 40%, of the energy required, followed by transportation which is 28% and industrial processes account for about 22%. Most of the electricity is produced by coal-fired power plants but as we move forward, most of the coal based power plants are going to be retired and the next generation of electricity will be largely dependent on natural gas. The total energy consumption from natural gas increased to 23.7% up from 16% in 2011. Global gas production grew by 1.1% in 2013 [4]. Natural gas can be used to generate electricity in various ways, but the most basic natural gas-fired electric generation consists of a steam generation unit, where natural gas is combusted in a boiler to heat water, which produces steam that rotates a turbine to generate electricity. Although these basic steam units are more typical of large coal or nuclear generation facilities, they are also used with natural gas power systems. These basic steam generation units have fairly low energy efficiency. Typically, only 33 to 35% of the thermal energy used to generate the steam is converted into electrical energy [5].

1.2 GLOBAL WARMING

We are paying a huge price by generating power at such low efficiencies, as now the threat of global warming has been well established. The main cause of global warming is the emission of CO_2. It has been stated that during the last century the global surface temperature has increased by 0.6 °C (6). The alarming concern is that the temperature has been rising at a much faster rate in the last two decades, as seen in Figure 1.3.

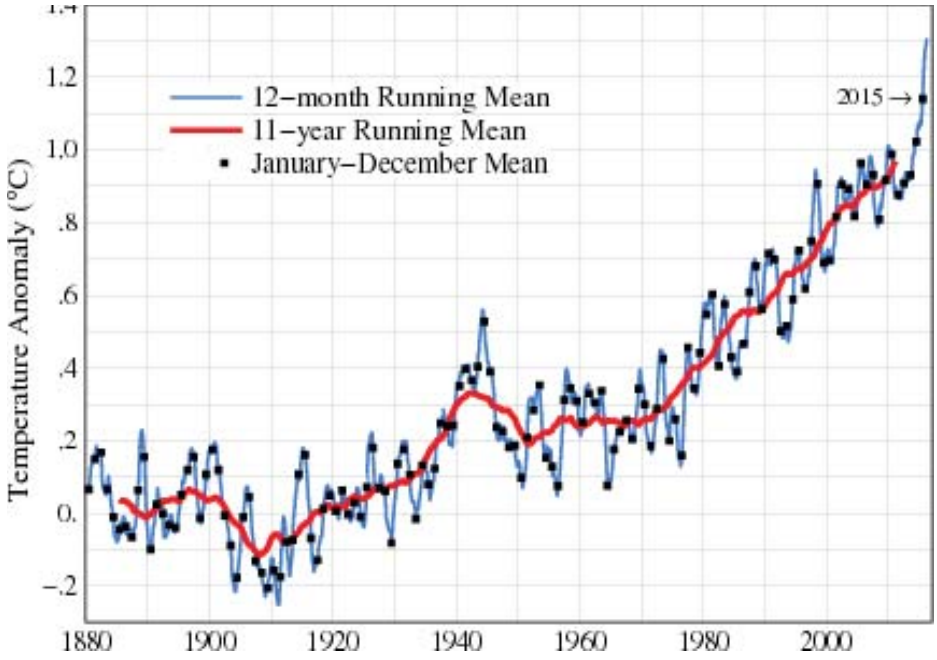

Figure 1.3 Global temperature rise [7]

If this threat is not addressed, it can prove to be disastrous for the human race and its existence on earth.

The world leaders have realized both these alarms which have led to the increased investments in fuel cells. A fuel cell is an electrochemical device that is capable of converting chemical energy directly into electrical energy. They provide a continuous source of energy as long as they are supplied with the fuel. Since these systems are not heat engines, they are not subject to the efficiency limits of a Carnot-cycle and hence they are able to provide higher efficiency than mechanical engines.

1.3 FUEL CELLS

Fuel cells were discovered more than 160 years ago. Alessandro Volta was the first person who is known to observe the electrochemical phenomenon. Sir Humphrey Davy

in 1802 created the first fuel cell, which was only capable of delivering a weak electric shock [8]. The discovery of a functional fuel cell has been credited to Sir William Grove who demonstrated the electrolytic water splitting reaction in 1839 [9]. We have come a long way since then. NASA spent millions of dollars conducting research on a hydrogen based fuel cell for their space shuttle Apollo in 1960. Fuel cells today power a wide variety of objects and have gained interest for large scale power generation.

There are five different commonly used fuel cells. These are listed in Table 1 with some of their main characteristics. There are other types of fuel cells that are usually employed to perform a specific function, for example, biochemical fuel cells, sodium amalgam cells, etc. The two most researched fuel cells are the Proton Exchange Membrane (PEM) and Solid Oxide Fuel Cells (SOFC). PEM cells operate at low temperatures (80-120 ^{o}C) and are very susceptible to minute impurities that may be present in the fuel and have a lower efficiency. SOFCs like Molten carbonate fuel cells (MCFC) involve higher temperate and are more tolerant of impurities that are maybe present in the fuel. Both SOFCs and MCFC's provide high efficiencies but the main disadvantage of MCFCs is the corrosion and creep instigated due to molten alkaline salts present in it [10]

Table 2.1 The five main types of fuel cells [10]

Fuel Cell Type	Electrolyte	Charge carrier	Fuel	Temperature	Efficiency
Solid oxide fuel cell (SOFC)	YSZ	O^{2-}	H_2, CH_4, CO	800-1000°C	60%
Alkaline FC	KOH	OH^-	Pure H_2	80°C	40%
Solid polymer proton conductor fuel cell	Nafion	H^+	Pure H_2, $(EtOH)^3$	80-260°C	40%
Phosphoric acid fuel cell	H_3PO_4	H^+	CO-free H_2	200°C	40%
Molten carbonate fuel cell	62% $Li_2CO_3^+$ 38% K_2CO_3	CO_3^{2-}	H_2, CH_4, CO	650°C	60%

SOFCs offer several advantages over other fuel cells:

- They are the most efficient (fuel input to electrical output)
- They are most suited for distributed power generation and hence can prevent transmission losses Figures 1.4 and 1.5.
- The high operating temperature of SOFCs generates heat which can be used for co-generation, which can further improve its efficiency.
- They can self-sustain once the operating temperature is reached (750 ^{0}C)
- They do not have any liquid electrolytes which usually are corrosive and difficult to handle
- They are tolerant to CO [11]
- SOFCs are expected to have a longer life expectancy of more than 40,000-80,000 h.

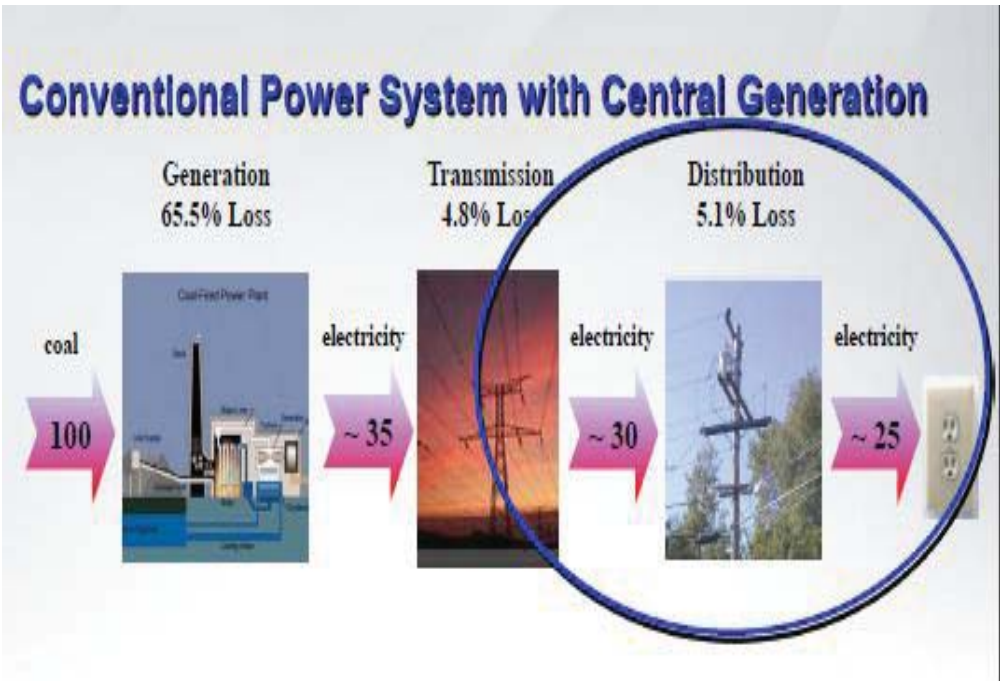

Figure 1.4 Transmission losses due to central power generation [12]

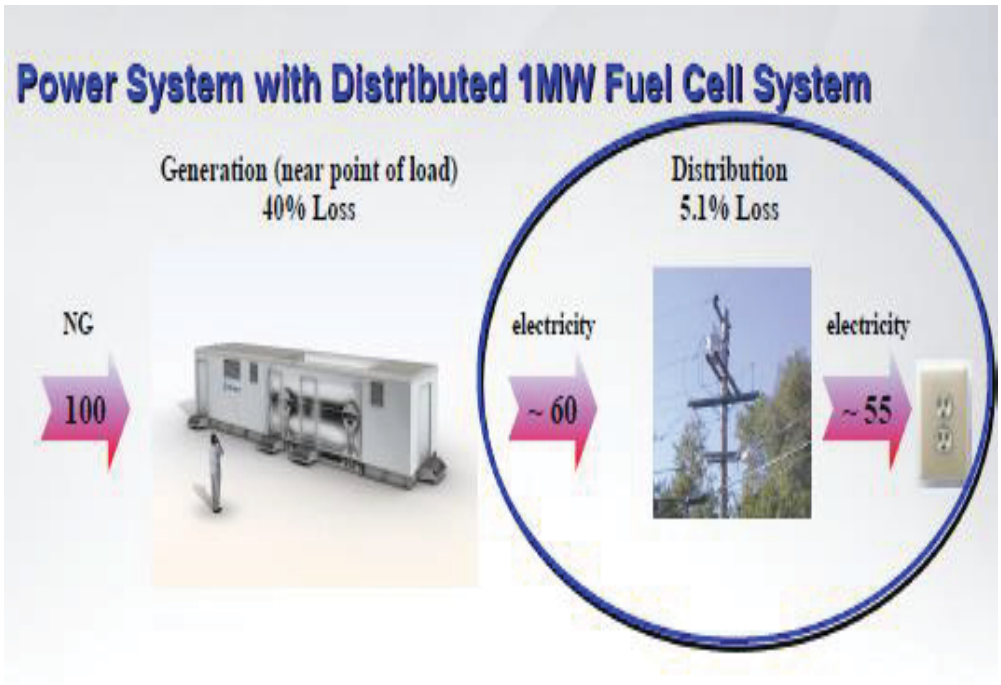

Figure 1.5.Transmission losses reduced by distributed power generation [12]

1.4 SOLID OXIDE FUEL CELLS

A solid oxide fuel cell, as the name itself indicates, is a fuel cell for which the electrolyte consists of a (ceramic) metal oxide. The basis of modern SOFCs was laid down by the German scientist Walther Nernst, who developed the "Nernst mass", which consisted of 85% zirconium oxide and 15% yttrium oxide. This composition has been altered and developed into an electrolyte with high oxide-ion conductivity [13]. A solid oxide fuel cell typically is operated at 600-1000 ^{0}C. Lowering the temperature can lead to a 6% increase in the efficiency of a solid oxide fuel cell [14]. For hybrid and cogeneration solid oxide fuel cell systems, efficiencies of higher than 80% have been predicted [15].

1.5 COMPONENTS OF A SOLID OXIDE FUEL CELL

The main components of an SOFC are the anode, the cathode and the electrolyte. In order to construct practical electric generators from SOFC's, multiple cells have to be stacked in-series. This can be done with an interconnect, which connects the anode of one cell to the cathode of the adjacent cell.

1.5.1 Electrolyte

The basic requirements for a material to be selected as an electrolyte for an SOFC electrolyte are [16].

1. High ionic conductivity and low electronic conductivity;
2. Stability in reducing and oxidizing environment;
3. Ability to be processed as a thin gas tight film;
4. Acceptable cost and availability.

The most common high temperature solid electrolytes are [17]:

- Yttria-stabilized zirconia, YSZ
- Gadolinium-doped ceria, GDC

The ceria based electrolytes have been studied extensively, as they have high oxide ion conductivity at lower temperatures (500 – 800 °C). The main disadvantage to them is the reduction of Ce^{4+} to Ce^{3+} at low partial pressures of oxygen, which makes them electronically conductive and leads to short circuits [18].

In this study we focused on using YSZ as the electrolyte. In its natural form, ZrO_2 is known to have three different crystal structures. ZrO_2 has a monoclinic structure at a room temperature, which then changes to tetragonal at 1170 °C, and then once the temperature reaches 2370 °C it converts to a cubic fluorite structure. The tetragonal/monoclinic phase transformation in ZrO_2 is thermodynamically reversible, but it is accompanied by a substantial volume change (3 to 5%). The cubic phase of ZrO_2, exists until the temperature reaches the melting point of ZrO_2 which is 2680 °C. The phase change in ZrO_2 can be prevented by the addition of certain oxides of which the most common ones are CaO, Y_2O_3 and MgO. The ability of these oxides to form solid solutions with ZrO_2 is very high [19]. The phase diagram for ZrO_2-Y_2O_3 is shown in Figure 1.6.

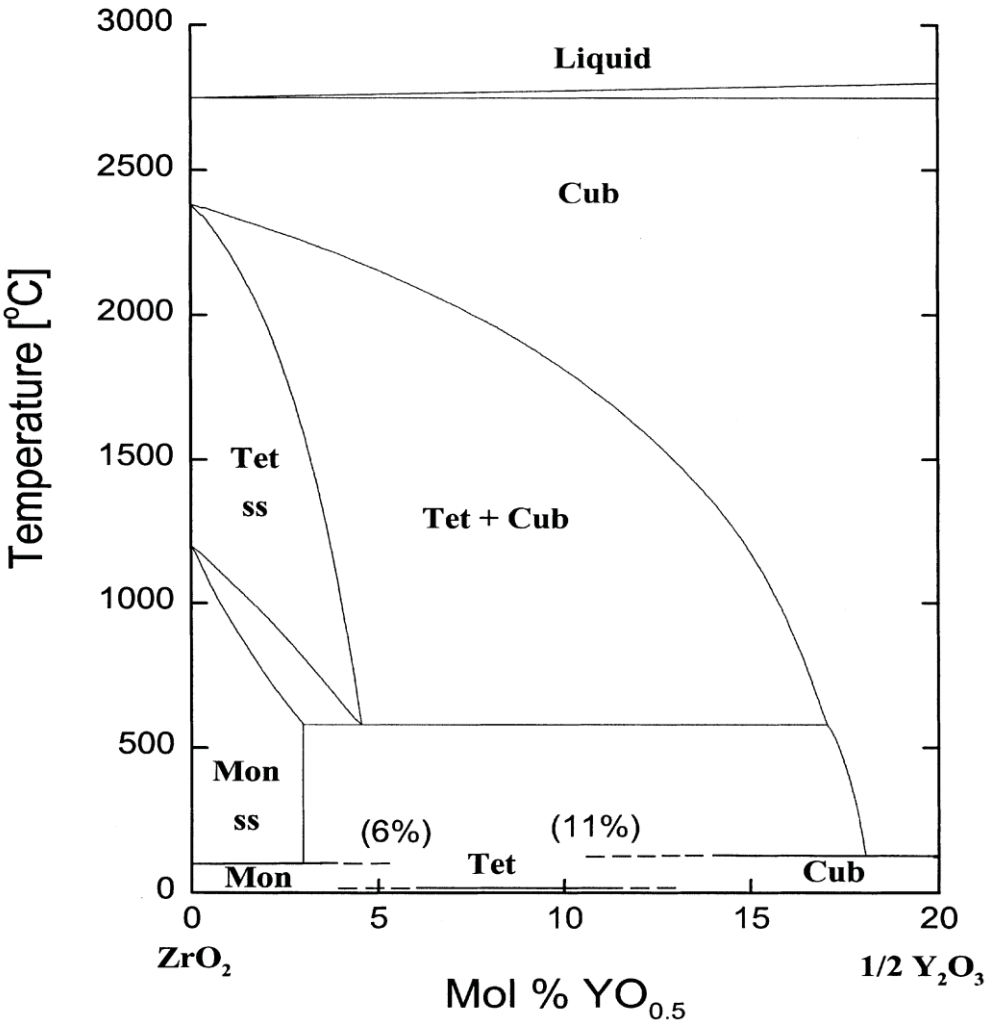

Figure 1.6 Phase diagram for ZrO_2-Y_2O_3 [19]

The composition that gives the highest conductivity to ZrO_2 is also usually the least amount that is required to stabilize the structure of ZrO_2. The substitution of Y^{3+} ions also creates additional oxygen vacancies required for SOFC operation, the ionic conductivity is the highest when 8 mol% of Y_2O_3 is added to ZrO_2. Figure 1.7 shows the creation of vacancies by the addition of Y_2O_3 [20]

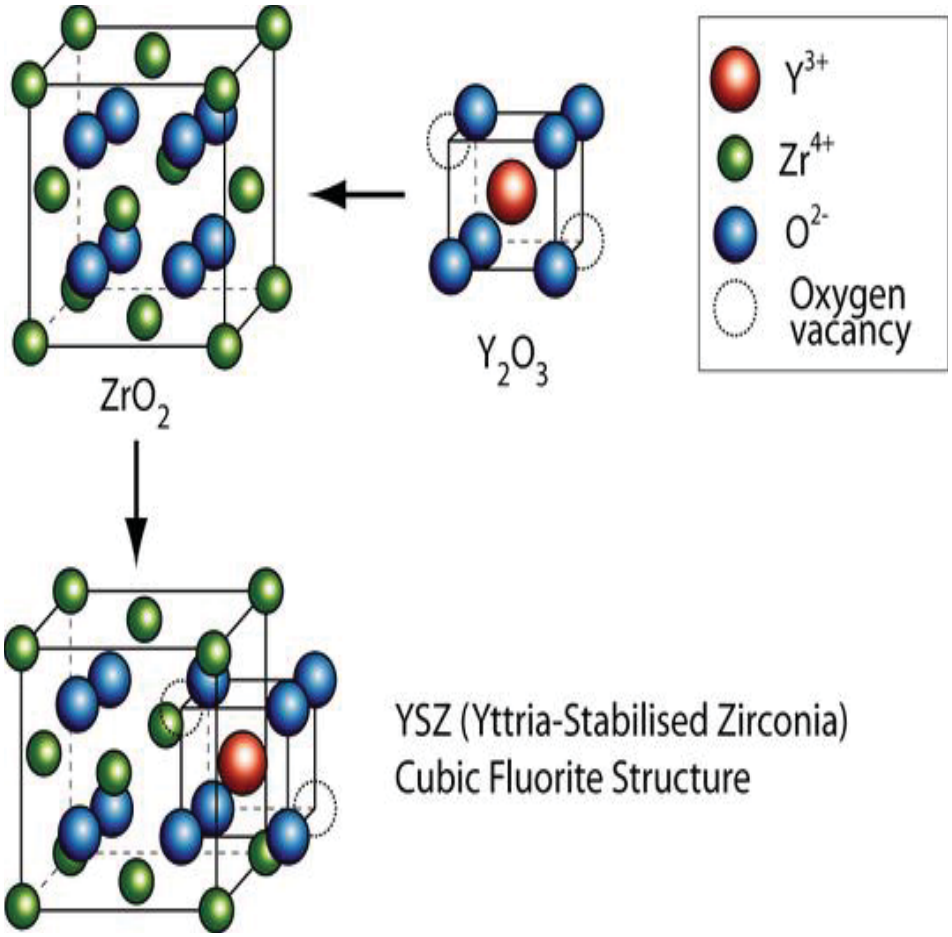

Figure 1.7.Oxygen vacancies created by the addition of Y_2O_3 [20]

1.5.2 Anode

The anode is the electrode where the fuel is oxidized. Its main role is to provide sites for fuel oxidation, and supply electrons to the external circuit. In anode supported cells it also acts as the cell mechanical support. The main requirements for an SOFC anode are [16], [21]:

1. Good electrical conduction;

2. High electrocatalytic activity;

3. Porous to gas inflow and outflow but mechanically resistant;

4. Thermal expansion coefficient close to neighboring components;

5. Low cost, especially when used as a mechanical support;

6. Stability at high temperatures in reducing atmosphere and to RedOx Cycles;

7. Capability to avoid coke deposition and tolerate sulfur in fuels.

Anodes are made of:

- Cermets of Ni-YSZ ,
- Cermets of Ni-SDC (Samarium doped Ceria)

The most popular material for anodes today is Ni-YSZ, and this is mainly due to the low cost of Ni when compared to Pt, Au etc. YSZ's main role is to maintain porosity of nickel for long periods of time as it inhibits coarsening of the particles at higher temperatures.

1.5.3 Cathode

The cathode/electrolyte interface is the area where the oxygen is reduced to O^{2-}. The basic requirements for a cathode are therefore [22], [23]:

1. High electronic and ionic conductivity;
2. High electrocatalytic activity for the cathode oxygen reduction;
3. Chemical stability in oxidizing atmosphere;
4. Similar expansion coefficient and good adherence to the solid electrolyte;
5. Porous structure that permits rapid mass transport of reactants, and
6. Product gases;

7. Low cost.

The cathode is composed of:

- Mixed ionic-electronic conductors (these consist of materials that conduct both ions and electron charge carriers or holes), such as (Sr doped) $LaMnO_3$, LSM [17].

$LaMnO_3$ is also has a cubic perovskite structure as shown in Figure 1.8. At room temperature undoped $LaMnO_3$ has an orthorhombic structure which changes to orthorhombic/rhombohedreal at 600 °C. The transformation is due to the oxidation of Mn^{3+} ions to Mn^{4+} ions [24].

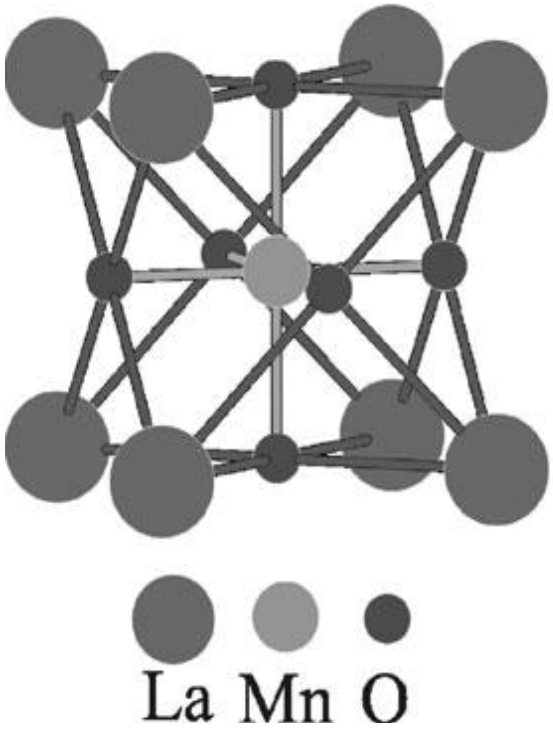

Figure 1.8 $LaMnO_3$ structure [25]

$LaMnO_3$ is a p-type conductor. The electrical conductivity of $LaMnO_3$ is around 10^{-4} Ω^{-1} cm^{-1} at room temperature and about 0.1 Ω^{-1} cm^{-1} at 700 °C. Hence, for it to be used as

cathode, its conductivity has to be enhanced by making a substitution at either A or B site by an atom of a lower valence electron. The most common doping elements are calcium and strontium [24].

Strontium enhances the electronic conductivity of $LaMnO_3$ by increasing the Mn^{4+} concentration [24].

$$LaMnO_3 \rightarrow \quad La_{1-x}^{3+}Sr_{x}^{2+}Mn_{1-x}^{3+}Mn_{x}^{4+}O_3 \qquad 1.1$$

1.5.4 Interconnect

The main function of an interconnect is to connect individual cells in series, Figure 1.9 shows an interconnect in a planar cell.

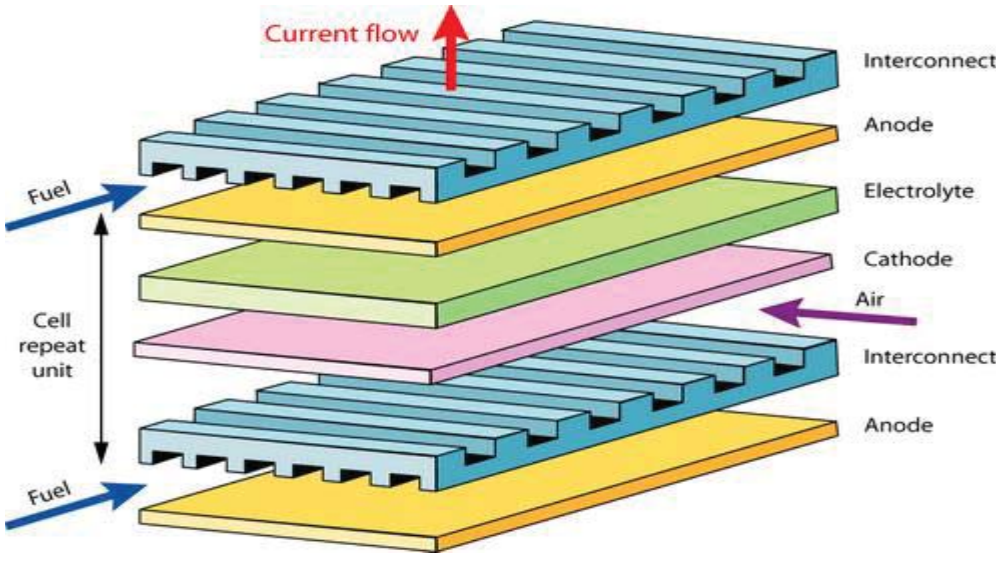

Figure 1.9 An example of interconnect in an SOFC [26].

There are many chemical and physical properties that an interconnect must possess. The interconnect must be [27]:

- Stable in both oxidizing and reducing environments, since it is connected from the anode of one cell to the cathode of the adjacent cell.
- Extremely stable in terms of its microstructure, chemistry and phase.
- Very dense and prevent any direct mixing of oxygen and reducing gases, particularly hydrogen, during the process.
- Crack resistant; its thermal expansion coefficient should match with the electrodes and electrolyte.
- Strong and also be creep resistant at elevated temperatures.
- Easy to fabricate and easily manufactured on a large scale to make commercialization possible.
- Resistant to oxidation and carburization.
- Resistant to inter-diffusion with the adjacent layers which could affect the overall performance of the cell.
- Electrically conductive to maintain low electrical resistance during cell operation to avoid decreased efficiency due to ohmic losses.

At present there are two different kinds of interconnects, metallic-based and ceramic-based. The main aspect of both these technologies is the presence of chromium. The key to the success of the chrome-based metallic materials is that the surface of the interconnect usually oxidizes, forming a chromia scale, which is a good conductor. Since the present work only deals with single SOFC units, developing and employing

compatible interconnects was unnecessary, but will become important when scaling up to make fuel cell stacks [27].

1.6 SOFC OPERATION

Figure 1.10 shows the basic operation of an SOFC. Air is fed into the cathode and fuel is fed into the anode. The cathode and anode are separated by an electrolyte. At the cathode the oxygen present in the air is reduced to produce oxide ions which are transferred through the electrolyte to the anode. The protons that are produced by the oxidation of fuel in the anode compartment reacts with the oxide ions to produce water and thereby generate an electric current.

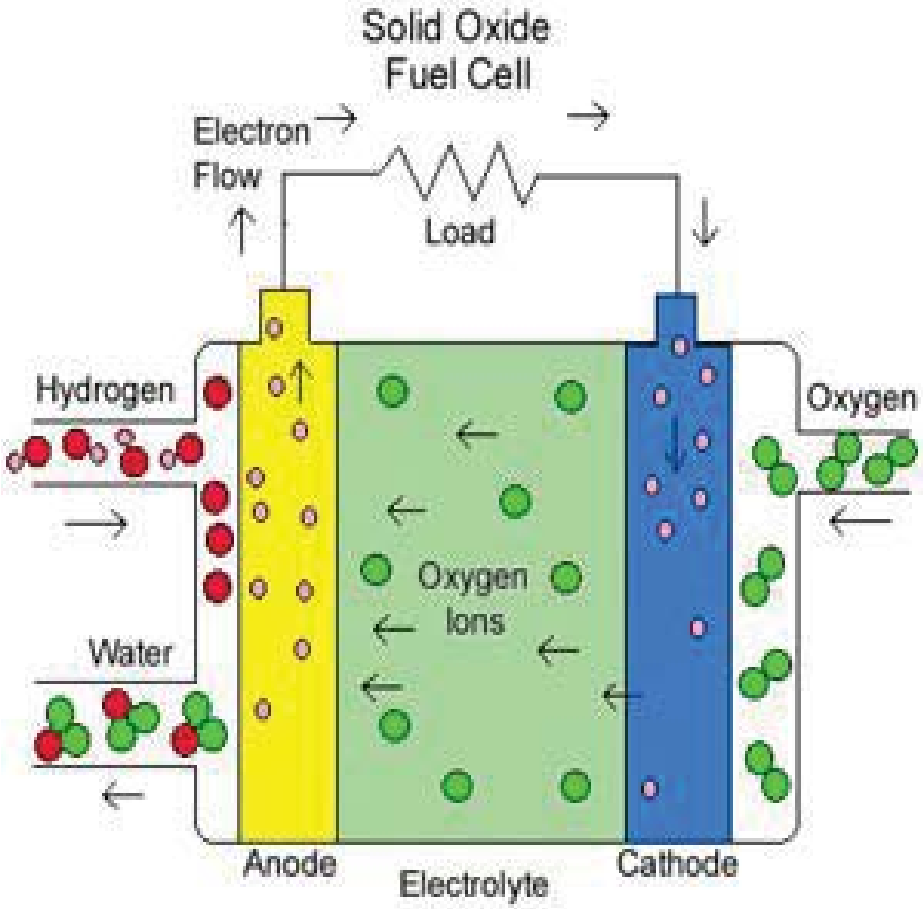

Figure 1.10 Solid oxide fuel cell operation [28]

The reactions in a solid oxide fuel cell occur at the Three-Phase Boundary (TPB) [29]. The TPB shown in Figure 1.11 is the point of contact between electrode, electrolyte and fuel or air.

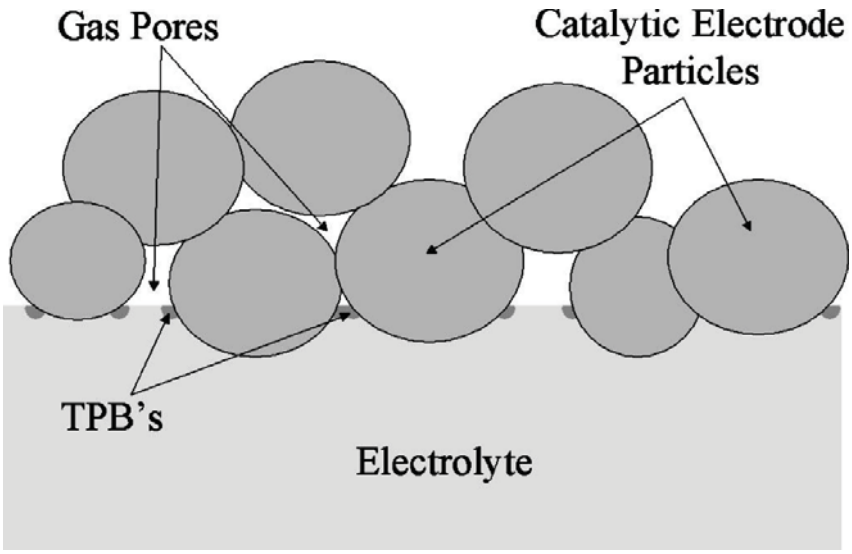

Figure 1.11 Three-Phase Boundary (TPB) [30]

The reactions that occur when one uses hydrogen as a fuel are as follows:

Cathode: $O_2 + 4\ e^- \rightarrow 2\ O^{2-}$

Anode: $2\ H_2 + 2\ O^{2-} \rightarrow 2\ H_2O + 4\ e^-$

Overall reaction: $2\ H_2 + O_2 \rightarrow 2\ H_2O$

Natural gas consists of methane and hence the reactions taking place in the SOFC are suggested to be [17]:

$CH_4 \rightleftharpoons C + 2\ H_2$ (Anode reaction)

$C + 2O^{2-} \rightleftharpoons CO_2 + 4\ e^-$ (Anode reaction)

$2\ H_2 + O^{2-} \rightleftharpoons 2\ H_2O + 4e^-$ (Anode reaction)

$O_2 + 4\ e^- \rightarrow 2\ O^{2-}$ (Cathode reaction)

1.6.1 Thermodynamics principles of an SOFC

The reaction that takes place at the cathode as mentioned before is as follows. Subscript (c) represents cathode [24]

$$O_{2(c)} + 4\ e^- \longrightarrow 2\ O_{(e)}^{2-}$$

The oxygen ions migrating to the anode gives us the following equation

$$2\ O_{(e)}^{2-} \longrightarrow O_{2\ (a)} + 4\ e^-$$

The subscript (a) denotes anode and hence the equation that controls the cell voltage can be written as:

$$O_{2(c)} = O_{2\ (a)}$$

Therefore SOFCs can be considered as oxygen concentration cells given by the Nernst equation

$$E_r = \frac{RT}{4F} ln \frac{PO2(c)}{PO2\ (a)} \qquad 1.2$$

Where E_r is the reversible voltage, R is the gas constant, T is the temperature, F is Faraday's constant and PO_2 is the partial pressure of the oxygen at the electrodes [24].

1.6.2 Polarization

The theoretical potential value of an SOFC is always higher than an actual performing cell which is due to the irreversible losses that occur in the system when current is drawn; this is called polarization or over-potential (η). It is governed by the following equation [24].

$$\eta = E - E_{th} \qquad 1.3$$

Where E is actual potential of the cell and E_{th} is the theoretical potential.

The three main types of polarization are:

- Activation polarization (η_{act})
- Ohmic polarization (η_{ohm})
- Concentration polarization (η_{conc})[31]

Activation polarization (η_{act}) is a direct result of the sluggishness of some electrodes; it is also related to the rate-determining step. The relationship of activation polarization and current density is given by Butler-Volmer equation:

$$\frac{i}{i_0} = \exp\left[\frac{(1-\alpha)nF\eta_{act}}{RT}\right] - \exp\left[\frac{(-\alpha)nF\eta_{act}}{RT}\right] \qquad 1.4$$

Where i is the charge transfer coefficient, i_0 is the exchange current density which can be determined by the extrapolation of log i vs η where $\eta = 0$.

This equation can further be simplified as Tafel equation below when the irreversibility is small.

$$\eta_{act} = a \pm b \log i \qquad 1.5$$

Where a and b are constants. The catalytic activity can be estimated by the Tafel slop (b), smaller the value of b better the catalytic activity.

The ohmic polarization is the result of resistance of electrons and ions; it is related to contact resistance among the various components of a cell as

$$\eta_{ohm} = i \text{ x } R \qquad 1.6$$

Where i is the current density and R is the total resistance of the cell. In order to ensure a low ohmic resistance a highly ionic conductive electrolyte and electrodes with high electronic conductivity have to be used. There also needs to be good adhesion between cell components [24].

The concentration polarization arises (η_{conc}) due to mass transfer or diffusion limitations. There has to be a steady flow of fuel to the electrodes in order for them to supply a steady current. When there is a reduction in mass transfer because of the lack of availability of abundant fuel, some of the available reaction energy has to be utilized to increase the mass transfer which may lead to the loss in output voltage. The concentration polarization can be obtained by the following equation [24]:

$$\eta_{\text{conc}} = \frac{RT}{nF} \ln\left(\frac{i_{l-i}}{i_i}\right) \qquad 1.7$$

Where i_l is the limiting current density at the electrode whose reaction is completely governed by mass transfer.

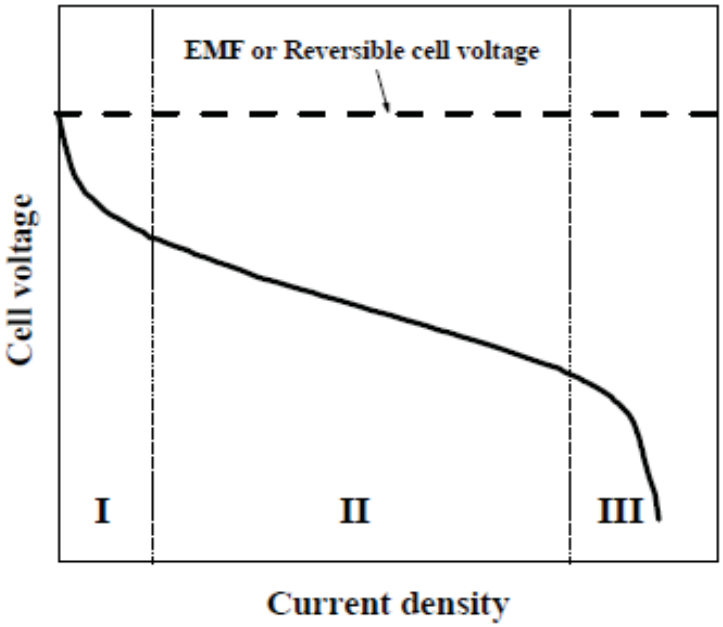

Figure 1.12 Regions of polarization [24]

These regions can be shown on an I-V curve of an SOFC which is shown in Figure 1.12 above. The activation polarization is prevalent at low current densities and hence it is in region one. The region two is governed by ohmic polarization losses where the voltage reduces linearly with an increase in current density. The concentration polarization can be found in region there where the cell voltage drop is at high current density.

1.7 MAJOR SOFC DESIGNS

A planar design is shown in Figure 1.13 below. Both square and circular designs have been employed.

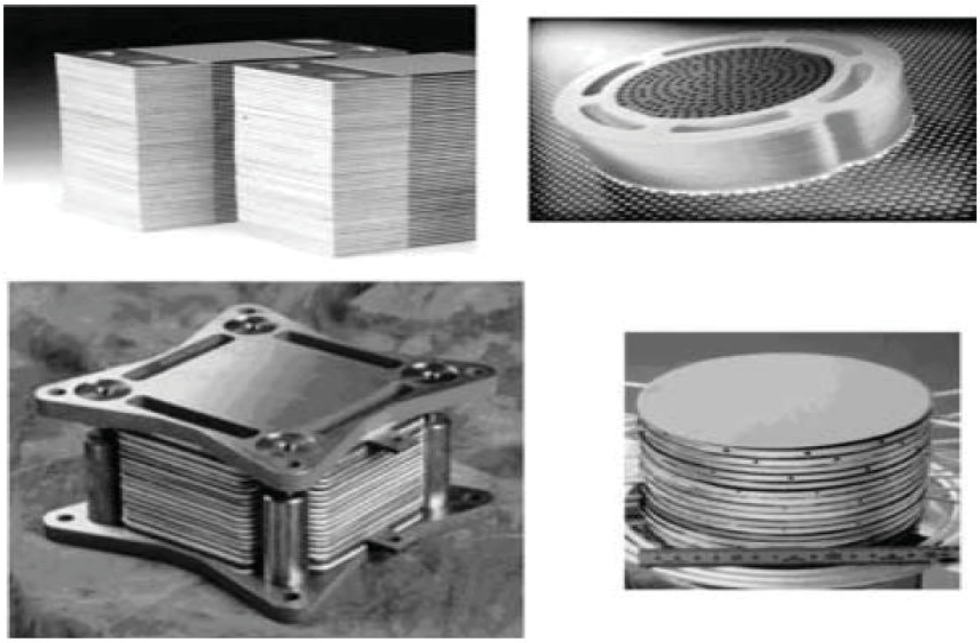

Figure 1.13 Planar design of an SOFC [32].

The tubular design is shown in Figure 1.14; it can be used to generate more power per unit area. It is also very easy to obtain a gas-tight seal for such a design. Planar tubes are easy to manufacture but achieving a gas tight seal is a huge obstacle. The tubular design is also regarded to be longer lasting but the cost of fabricating a tubular fuel cell is higher than a planar design.

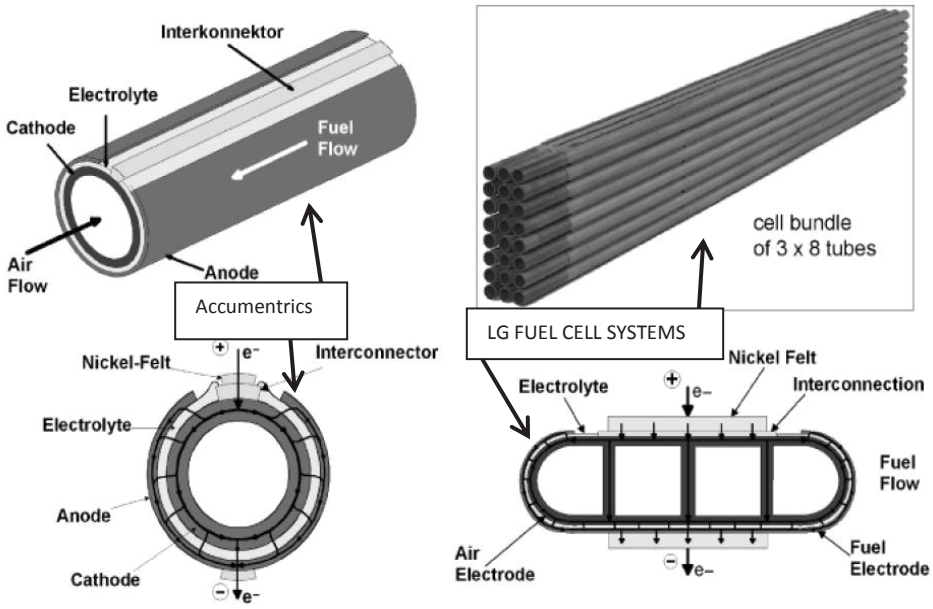

Figure 1.14 Microtubule tube design developed by Westinghouse and LGFCS and single tube design used by Accumentrics [32].

1.7.1 Monolithic Design

The Monolithic Solid Oxide Fuel Cell (MSOFC) design was developed in the 1980s by a team consisting of Argonne National Laboratory, Allied- Signal Aerospace and Combustion Engineering. The monolithic design is a concept where a complete SOFC stack that is made up of several single cells is fabricated as a single unit. The cell structure was fabricated using tape casting and hot roll calendaring. The power densities of MSOFC systems were calculated to be as much as 8 kW/kg for fuel efficiencies of over 50% and this was due to the small cell size and low resistivity losses in materials. The MSOFC operated at temperatures between 700 ^{0}C and 1000 ^{0}C. The electrode/electrolyte interfacial resistance for a MSOFC system was reported to be about 0.093 cm^2 for a cell with an electrolyte thickness of 50 microns. The design is capable of

achieving very high power densities due to it being compact and lightweight. This design has only been tested on a laboratory scale; it is presented in Figure 1.15[33].

Figure 1.15 Monolithic cell fabricated by tape casting [33]

The monolithic SOFC is made up of thin cell components which are formed into a corrugated structure. The gas flow in such designs can be manipulated to be either co-flow or cross-flow. In the co-flow design the fuel and air both flow parallel in adjacent channels which are formed by the laminated layers as seen in Figure 1.16 below.

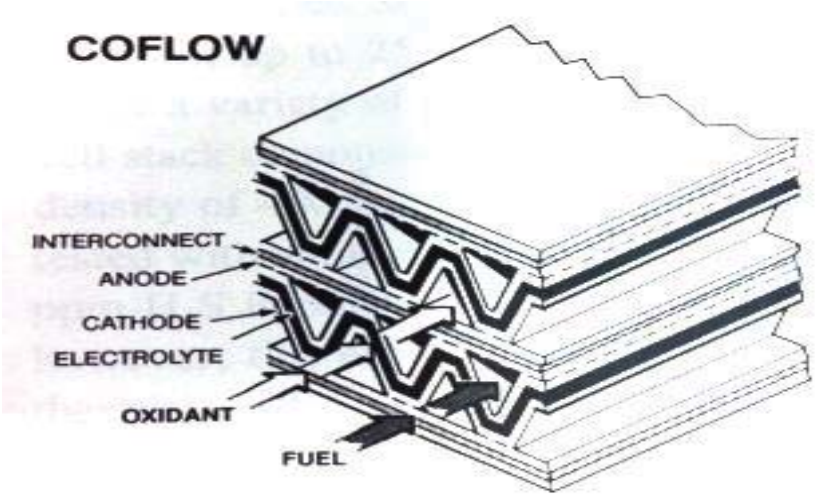

Figure 1.16 Monolithic design co-flow configuration [24].

In the cross flow design the anode and cathode are corrugated perpendicular to each other so, the fuel flows in from one side and air from the other side which can be seen in Figure 1.17 below.

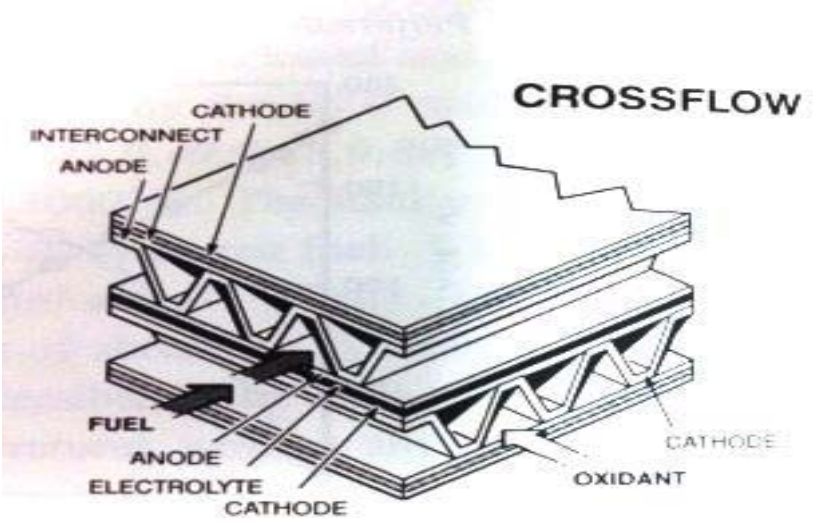

Figure 1.17 Monolithic design crossflow configuration [33]

The major differences between these two designs are power density and gas manifolds. The cross flow design demonstrates a lower power density when compared to the co-flow design. On the other hand the fabrication of a gas manifold for a cross flow design is much simpler than a co-flow design. The laminates in these designs consist of anode/electrolyte/cathode and anode/interconnect/cathode. The thickness of each cell laminate was kept below 200 microns. Accordingly, each cell component was held to 50-150 μm in thickness [24].

The corrugation height for both the systems co-flow and cross-flow was about 1-2 mm. The cells in a monolithic design are connected in a series. The current flows from the

anode of one cell to the cathode of another cell through the interconnect transversely. Then the current flows into the next cell and the process continues; this can be seen in Figure 1.18 below. Since the current path through the monolithic SOFC is very narrow, it reduces the voltage losses due to lessened internal resistance. The power density for a co-flow monolithic SOFC has been calculated to be about 8 kW/kg or 4 kW/L [34].

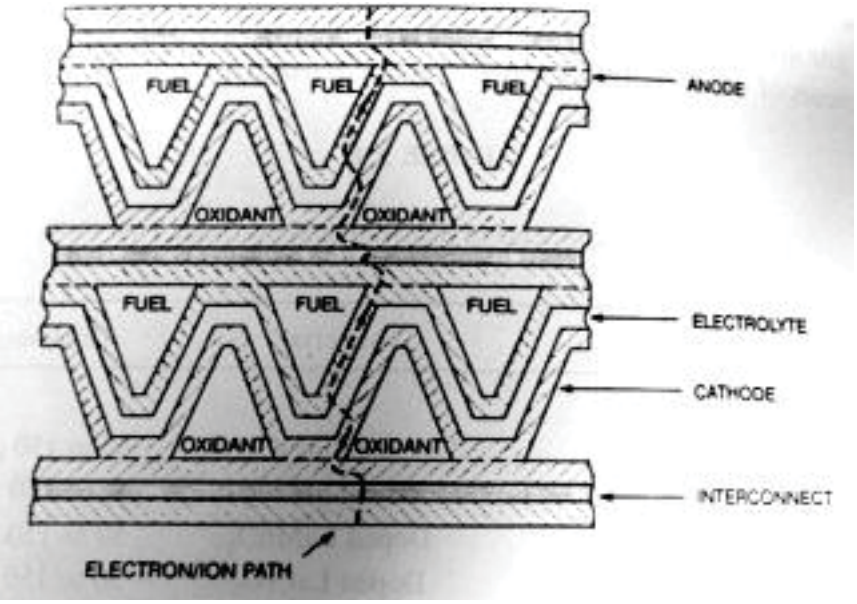

Figure 1.18 Current path in a monolithic SOFC [35]

1.7.2 Advantages and Disadvantages of Monolithic Design

One of the main features of the monolithic design is small cell dimensions and high power density. Since the cell size is very small, in a monolithic SOFC the active area or the triple phase boundary is higher. Also, since the internal resistance is low it allows monolithic SOFC designs to be operated at higher current densities while achieving the same output voltage. The monolithic SOFC design has the highest power output per unit mass or volume. The stack power density for a micro-tubular design manufactured by the

Japanese manufacturer TOTO were 478 W/L or 239 W/kg [35]. Molten carbonate fuel cells can only obtain between 30-86 W/kg [36]. It also has lower weight than other designs due to the absence of inactive structural supports.

One of the biggest hurdles that have prevented the commercialization of the monolithic SOFC was the difficulty of fabrication of the corrugated structure. Due to its unique structure, the complete monoclinic cell has to be co-fired. This requires that all four components of the cell have matching thermal expansion and similar firing shrinkages. Any mismatch of those properties would cause stress in the fired laminates which would lead to cracking during processing and operation. The cell structure of the monolithic design was originally fabricated using tape casting and hot roll calendaring. The tape casting process consists of spreading ceramic slurry uniformly onto a substrate such as glass or an organic film using doctor blading. Once the slip is dried the ceramic layer can be stripped off the substrate like a flexible tape. The hot-roll calendaring process consists of mixing ceramic powders with an organic binder and plasticizer and then rolled to form a very thin tape. This is shown in Figure 1.19. The green tapes are then cut to the required measurements and can be corrugated using a warm mold. On cooling the tape would retain the corrugated shape which can be then fired. Multiple layers can be formed by laminating the individual layers together before firing. The mechanical force that is applied in the following operation bonds the laminates together. The corrugations in the layers are made using a compression molding which involves the placement of a tape of the plastic mix between the platens of a shaped die and simultaneously applying uniaxial pressure until the tape deforms to the desired shape. For a uniform corrugated layer, uniform pressure and good material flow are required. The precise combination of

temperature, uniaxial pressure, press time and thickness of the green tape are required to have uniformity between the laminates. The firing temperature ranged between 1300 ^{0}C to 1400 ^{0}C to remove binder and sinter the structure [24].

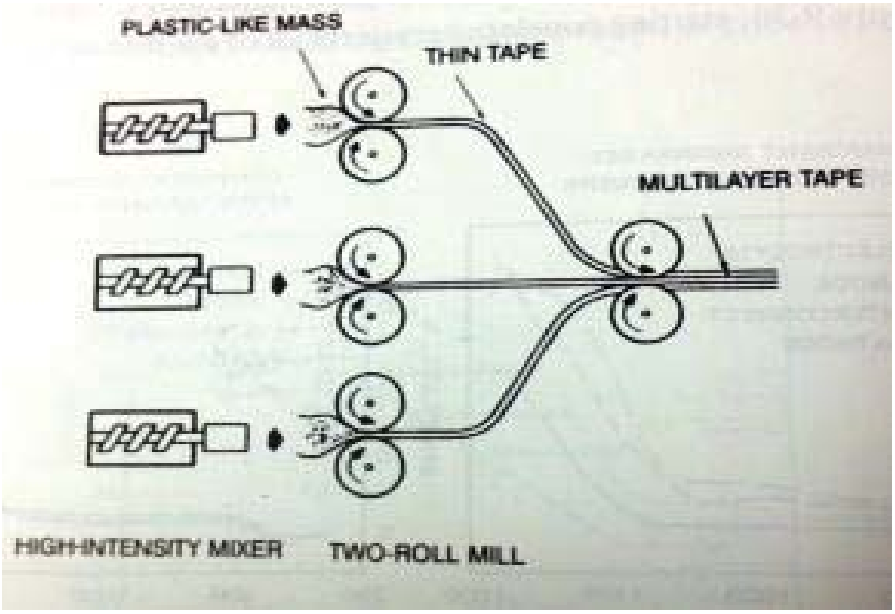

Figure 1.19 Tape Calendering process [24]

The success of the fabrication depends on several important factors such as powder characteristics, green state forming and firing. The starting powder characteristics is the most important factor, as surface area and the particle size influence sintering of a material in a major way. The powders for electrolyte and interconnect should have a small particle size and high surface area because these layers have to be sintered to near theoretical density. The shrinkage profiles of each layer can also be affected by the content of the organic binder as higher organic content would increase the overall shrinkage and so will the high surface area of the powder. Another parameter is the amount of solid loading (the amount of nonorganic material); high solids content would increase densification with less shrinkage. A high solid loading would also cause the

tapes to be less flexible and increase difficulty in lamination and corrugation. This was one of the issues faced when an SOFC was created using the tape calendaring method. The firing process is another important step required in the fabrication of a monolithic design. Usually there are two stages that are involved in the firing; first is observed at low temperature due to organic burnout. The shrinkage observed at this stage is very small compared to the second stage shrinkage which is observed during high temperature sintering of the material. The shrinkage in this stage is dependent on particle size, surface area and volume loading. The shrinkage profiles of all the laminated layers in a monolithic design should match each other or it would result in cracking and delamination. Figure 1.20 shows the cross section of a single cell obtained by tape calendaring.

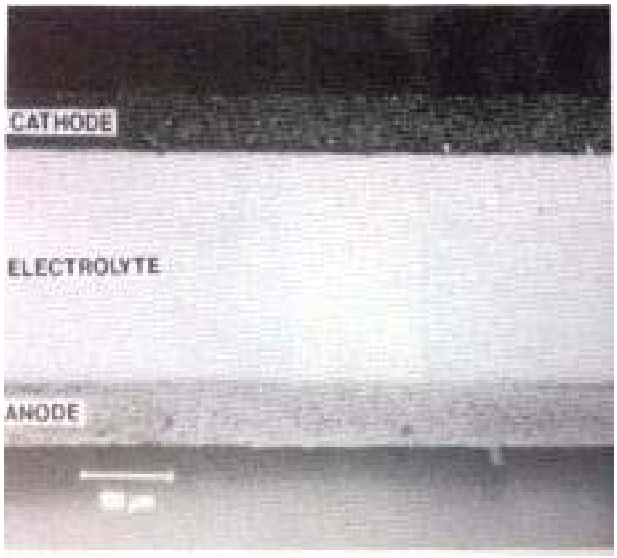

Figure 1.20 Cross section of a single cell made by calendaring (scale is 100 μm) [24].

1.8 3D PRINTING

3d printing, also known as additive manufacturing (AM), is a process for making three dimensional items from a digital file. The central idea involved in AM is the fabrication of objects via addition of material (building sequential layers) rather than subtraction from a larger piece, as is conventionally done with mills and lathes. The 3d printing technologies were developed in the 1980s but at the time they were referred to as Rapid Prototyping technologies. The first patent was filed by Dr. Kodama in Japan on May 1980 [37]. The variety of industries adopting AM technologies is presented in Figure 1.21.

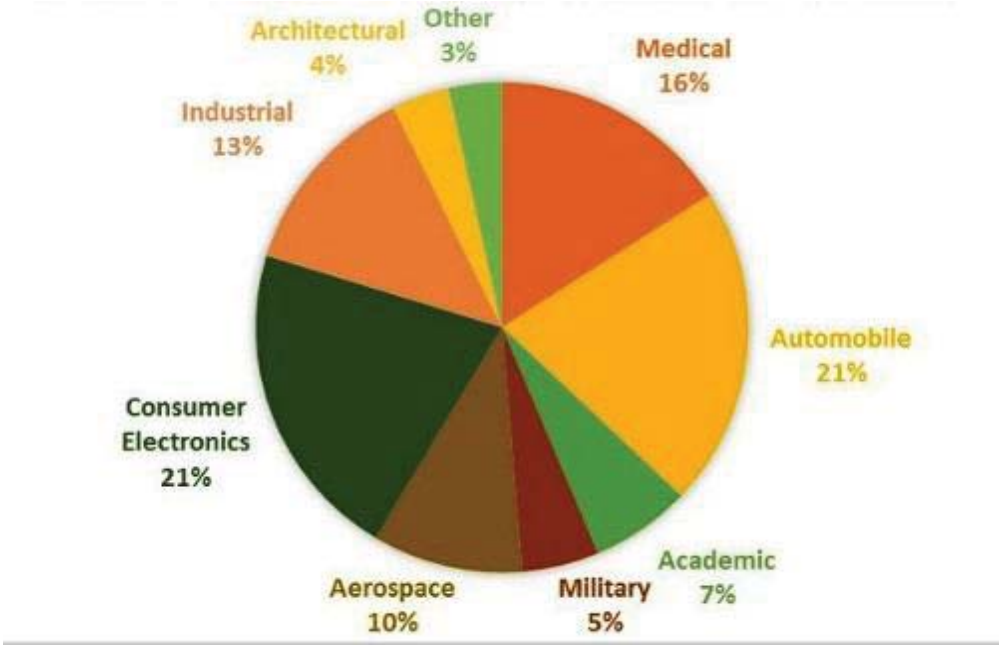

Figure 1.21 Industrial split of AM equipment customers [38]

The steps involved in an AM process are as follows [37]:

- Creating a computer assisted design (CAD) of the object that has to be fabricated

- The conversion of the developed CAD model into standard triangulation language (STL) format which is the language used to describe the entire object in terms of triangles
- Slicing the entire object into layers of a specified thickness
- Producing the entire object by the consecutive addition of 2d layers on top of each other
- Final processing of the object, which may include cleaning, removal of support structures, sintering etc.

The applications of AM can be categorized into three main types based on the use of the final product fabricated, which are rapid prototyping, rapid manufacturing and rapid tooling.

- Rapid Prototyping

The AM technologies can be used to develop various prototypes that can be used for design verification, real time testing and marketing. AM technologies can rapidly shorten development time and are also more cost effective compared to conventional methods [39]

- Rapid Manufacturing

AM technologies allow customers to rapidly develop their own parts rather than place orders with a manufacturer which can be time consuming [40].

- Rapid Tooling

AM technology can be used to produce a tool or a die. This process is known as Rapid Tooling (RP). RP can be further divided into direct tooling and indirect tooling. In direct tooling the AM technology can be used to directly produce the mold or die but in indirect tooling a pattern is produced via AM technology, which can be converted into a mold [41].

Figure 1.22 shows the number of AM machines that were sold each year. According to Wohlers, there were more than 278,000 3d printers sold in 2015. They claim that the compound annual growth rate for the entire AM industry in the last 27 years has been 26.2 percent.

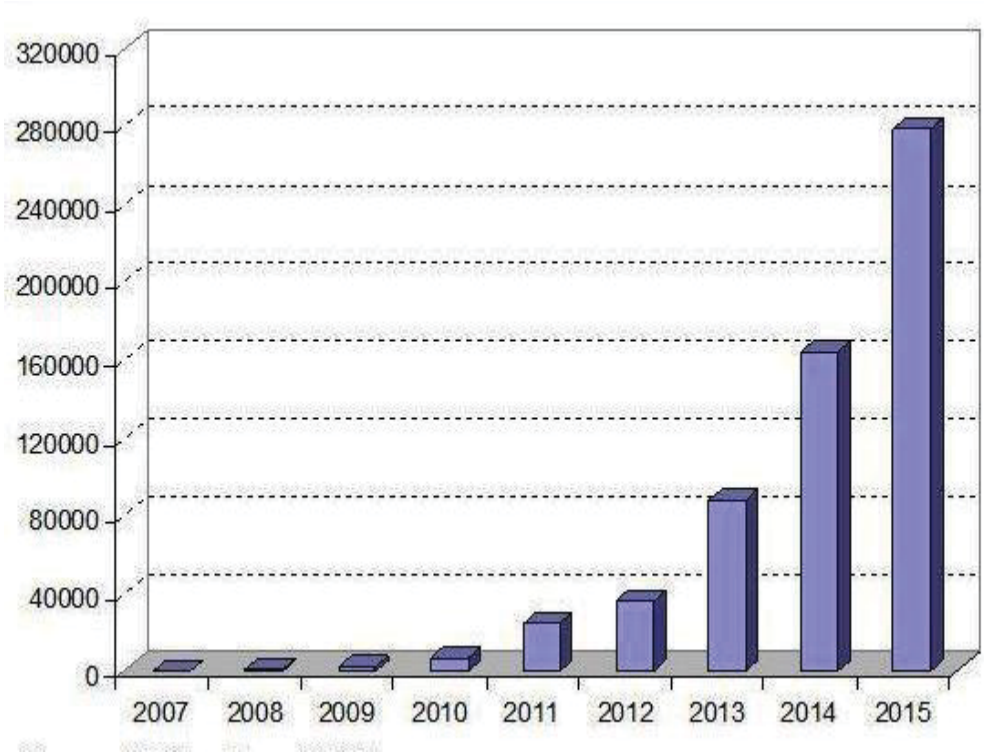

Figure 1.22 Number of AM Machines costing less than $5,000 Sold Each Year [42]

There are several different kinds of 3d printing technologies and all those available as of 2012 were additive. Selective laser sintering (SLS) and fused deposition modeling (FDM) technologies use methods that require melting or softening of materials to produce the layers. Another commonly used technique is called stereolithography (SLA). It is based on laying down liquid materials that are cured using different methods [37]

1.8.1 Stereolithography (SLA)

The first additive manufacturing process that was introduced in the market was known as Stereolithography or SLA. It was manufactured by 3D Systems in 1987 [43]. It is based on a photopolymer liquid resin contained inside a vat that can be solidified by an ultraviolet (UV) helium-cadmium or argon laser. The entire object is "sliced" into a sequence of thin layers and after each layer is drawn onto the support, it is solidified by scanning of the laser. The platform is then lowered and the process is repeated. After numerous iterations the entire object is fully fabricated. Some parts that require support structures are fabricated by the same process as the main object [44]. Once the complete part has been fabricated, the base plate can be raised to collect the part, which is then drainedand washed, and if it required support structures, they can be broken away. The SLA process is depicted in Figure 1.23.

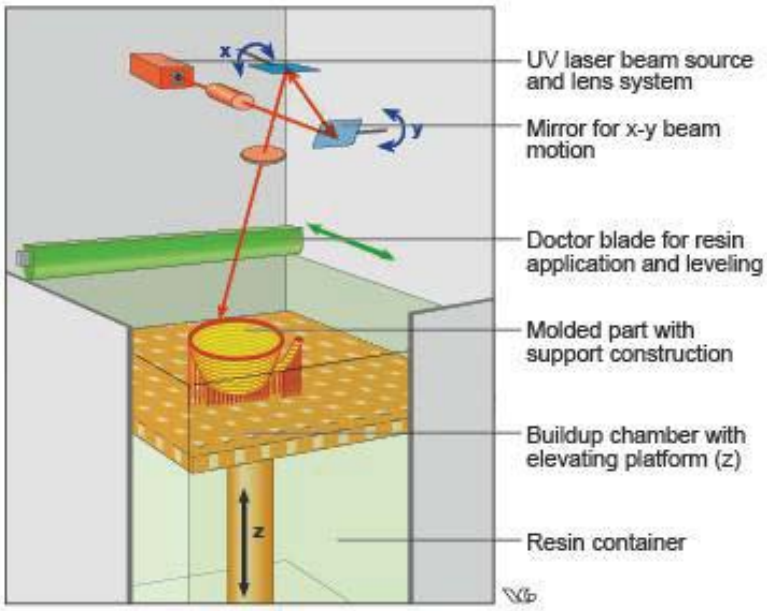

Figure 1.23 SLA process [45]

It is regarded to be one of the most accurate AM processes [46].

1.8.2 Selective Laser Sintering (SLS)

SLS uses a powerful laser that fuses or sinters particles of plastic, metal or ceramics. The laser selectively fuses the material by scanning after each layer has been laid down. SLS was developed and patented by Dr. Carl Decker at the University of Texas in mid 1980s. Figure 1.24 below shows the different steps involved in SLS technique. In this process the material powders are fused by a CO_2 laser to form each layer after which the bed it lowered and the cylindrical roller spreads a new layer of powder over the fused layer followed by the process of fusing using the CO_2 layer again. This process is repeated until the desired object is fabricated.

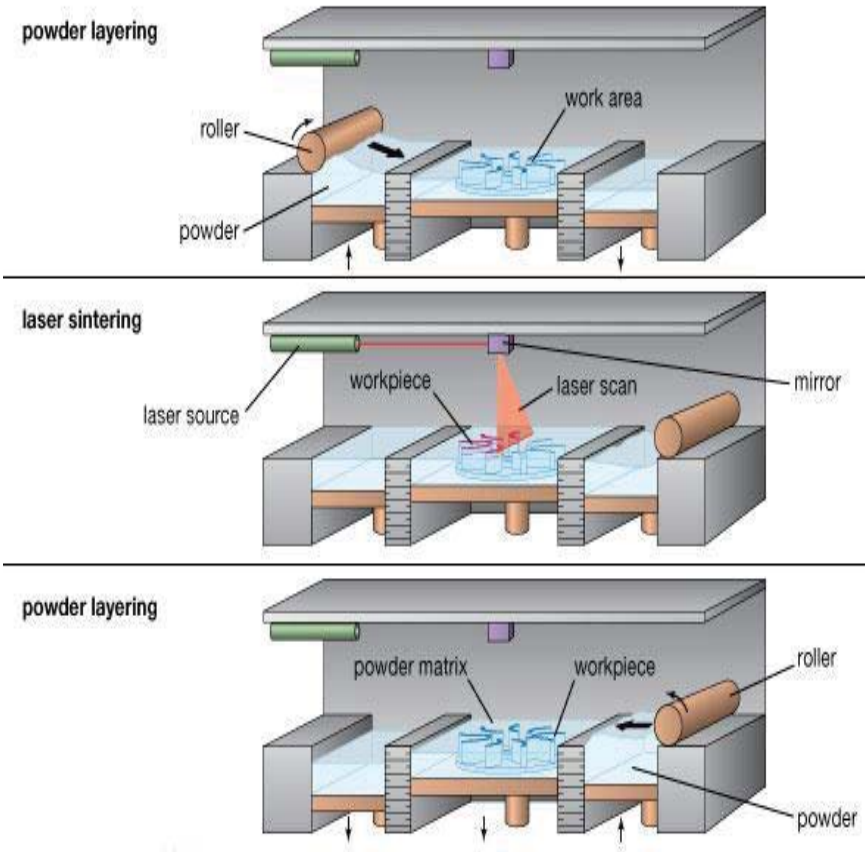

Figure 1.24 Selective Laser Sintering technique [47]

The SLS technique can be used to fabricate polyamide composites such as glass-filled or carbon-filled directly, but metals have to be developed indirectly. In the indirect process, first the polymer has to be sintered giving a green part which is followed by a second heat treatment cycle , in a furnace and its infiltration with bronze or copper to achieve a fully dense metal part [48].

1.8.3 Fused Deposition Modeling (FDM)

FDM technology uses a plastic filament or a metal wire that is passed through a heated extrusion nozzle which melts the material; the nozzle can be moved both horizontally and vertically as instructed by the computer aided manufacturing software package. The 3d

object is formed by the hardening of the material after extrusion from the nozzle. This technology was patented by Scott Crump in the late 1980s when he started his company, Stratasys. Figure 1.25 describes this technology.

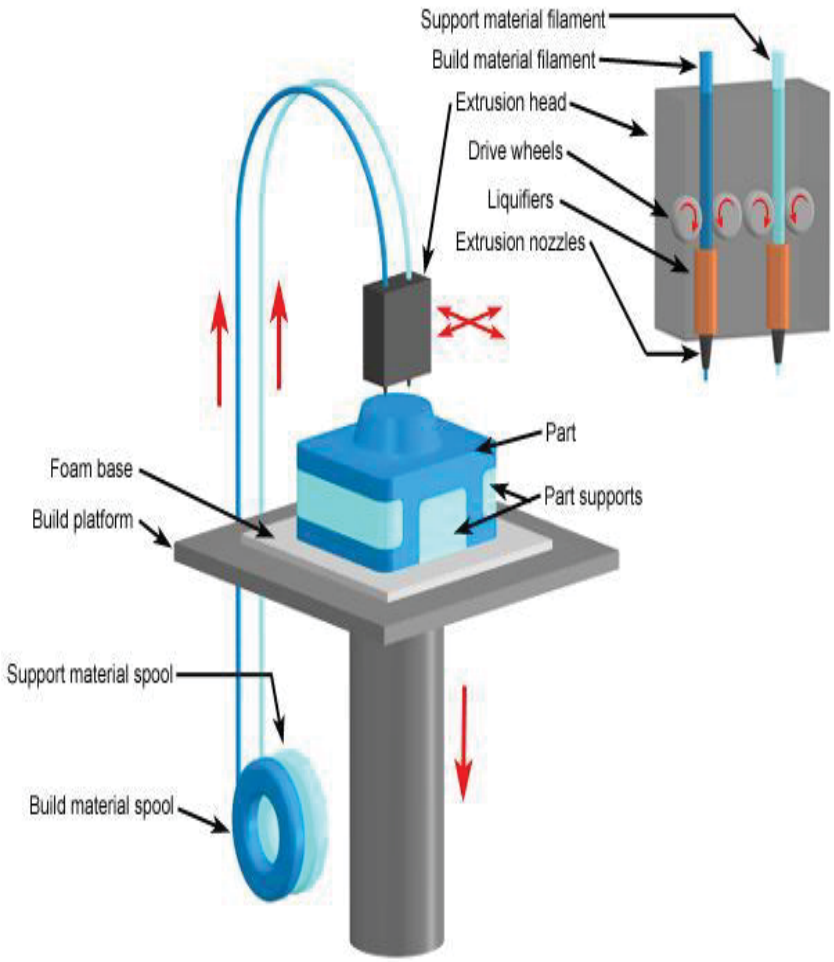

Figure 1.25 Fused Deposition Modeling technology [49]

FDM technology has several advantages, which include reliability, simplicity of fabrication and reduced cost. It has been widely used to print thermoplastic materials, which have a wide range of applications [50].

One main disadvantage to using this process is that parts manufactured through this process have reduced mechanical strengths, which is due to the uneven heating and cooling cycles involved [51]

1.8.4 Selective Laser Melting (SLM)

This technique is very similar to SLS, but in this process the laser is used to melt the powder but does not sinter it. This technique was developed by MTT Technologies group of Stone, UK, in 2003. The materials that can be used in this technique are stainless steel, aluminum alloys and titanium [52]. The main advantage of this technique is that fully dense structures can be fabricated directly by the use of this method [53].

1.8.4 3DP^{TM}

MIT developed a powder-based AM process called 3D printing (3DP^{TM}). This process involves fabrication of an object by spreading of powder over a surface of a powder bed. The layers are held together by a binder. The powder bed is lowered after the formation of each layer to allow the spread of a new layer. This process continues until the entire object has been fabricated [54]. This process is shown in Figure 1.26.

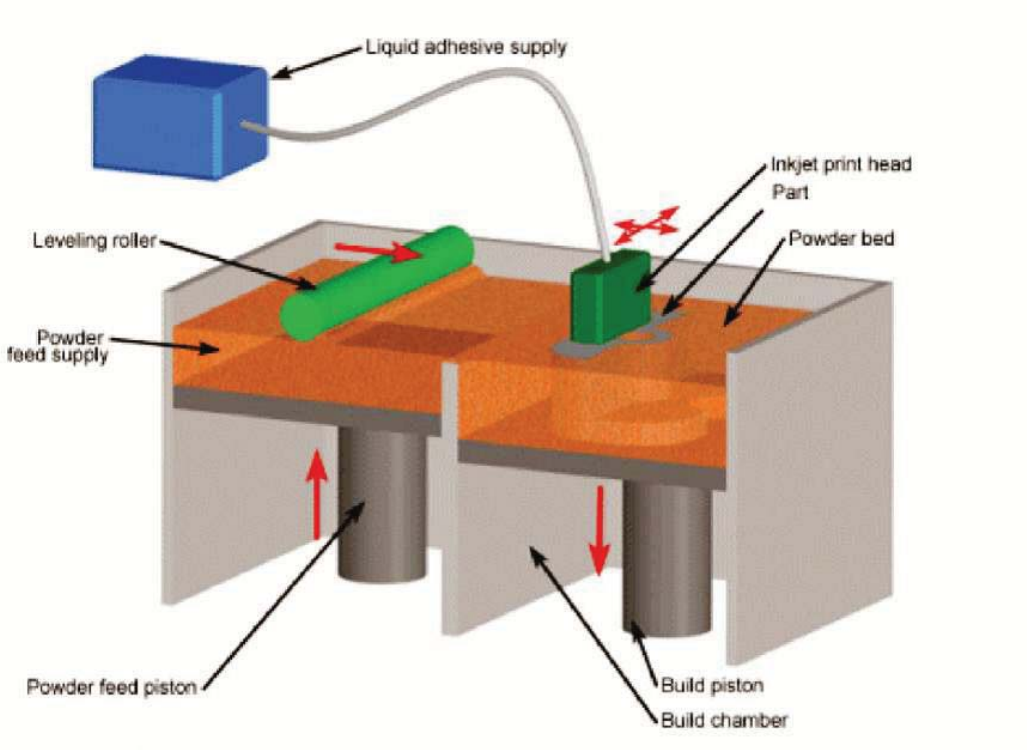

Figure 1.26 3DP Process [55].

The parts fabricated using this process are porous. One of the main advantages of this process is that it can reach definition of around 50 μm.

1.8.5 Ink-Jet

This process requires a jetting head that has 3 nozzles. The first nozzle is used to jet the thermoplastic material and the other two nozzles are used to deposit wax support. The layers are milled to have specific layer thickness. This process requires the utilization of drop on demand technology and high precision milling capability [56]. The ink-jet process is shown in Figure 1.27.

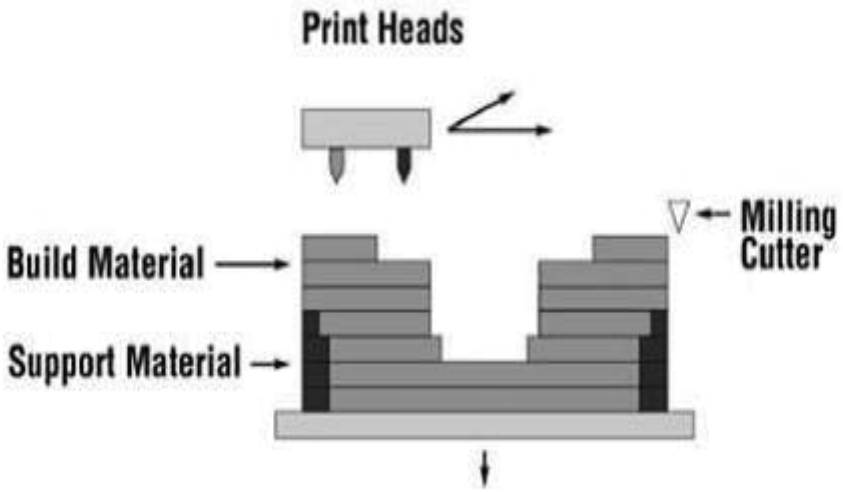

Figure 1.27 Ink-jet Process [64].

The main advantages of this process are low cost, reproducibility and the ability to deposit materials with different chemical and physical properties [56].

The disadvantages include longer processing time as it is a low speed process, the surface of finished parts is not very smooth and it is difficult to jet high temperature materials [56].

1.8.6 Laser Engineering Net Shape (LENS)

This process of AM requires the simultaneous deposition and fusion of material powders. It was developed by Sandia National Labs but was commercially made available by Optomec in 1997. This process is shown in Figure 1.28.

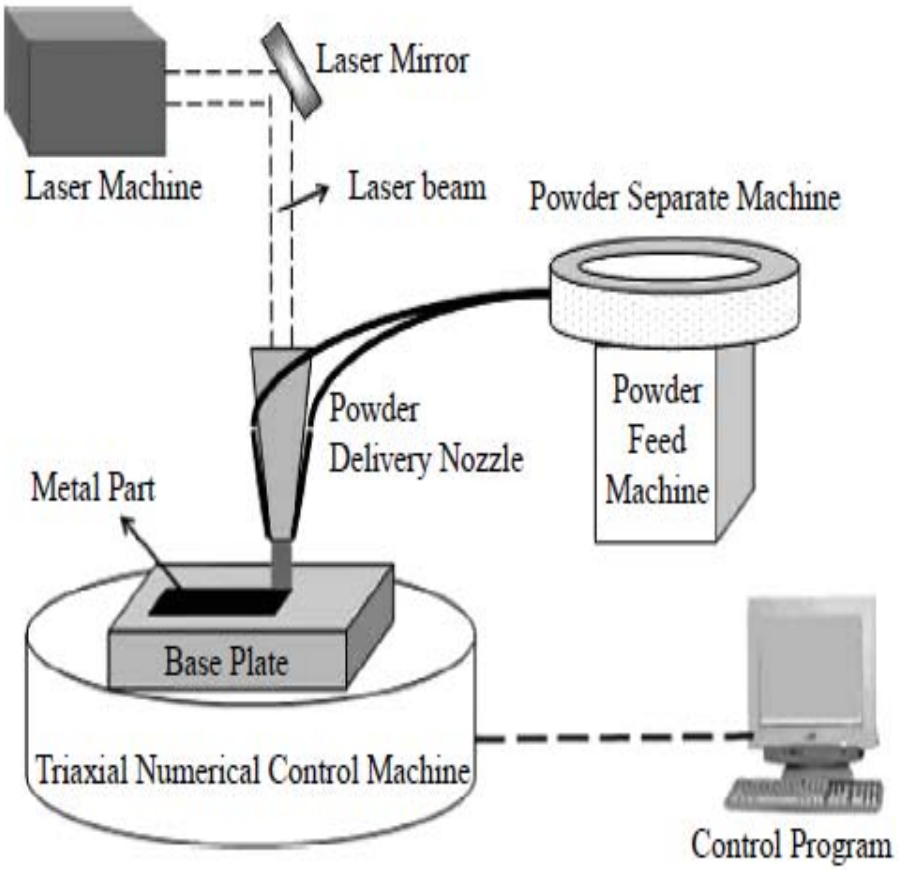

Figure 1.28 LENS Process [57].

The system consists of a head with a laser beam and two nozzles that feed the coaxial powder. The process is carried out in a controlled environment in the presence of argon. The high power laser is first focused on the metal part until it is melted, more powdered metal can be added through the nozzles to increase the volume. The table is allowed to move in X-Y direction and the head is capable of moving in the vertical direction which controls the part height.

This process has been used for the fabrication of nickel based alloys, steel and titanium. Fully dense parts can also be achieved through this process [58].

1.8.7 Electron Beam Melting (EBM)

This process was developed in 2005 by a Swedish company called Arcam AB. This process utilizes the concept that electrons that are generated by a gun can be focused and accelerated using an electromagnetic lens and then can be electro magnetically scanned via a CAD program [59].

In this process the first step spreading of the metal powder on the bed. The electron beam can then be used to melt the powder and thereby build the first layer. The bed can then be lowered to build another layer and the process is repeated until the desired object is obtained. The process of EBM is shown in Figure 1.29.

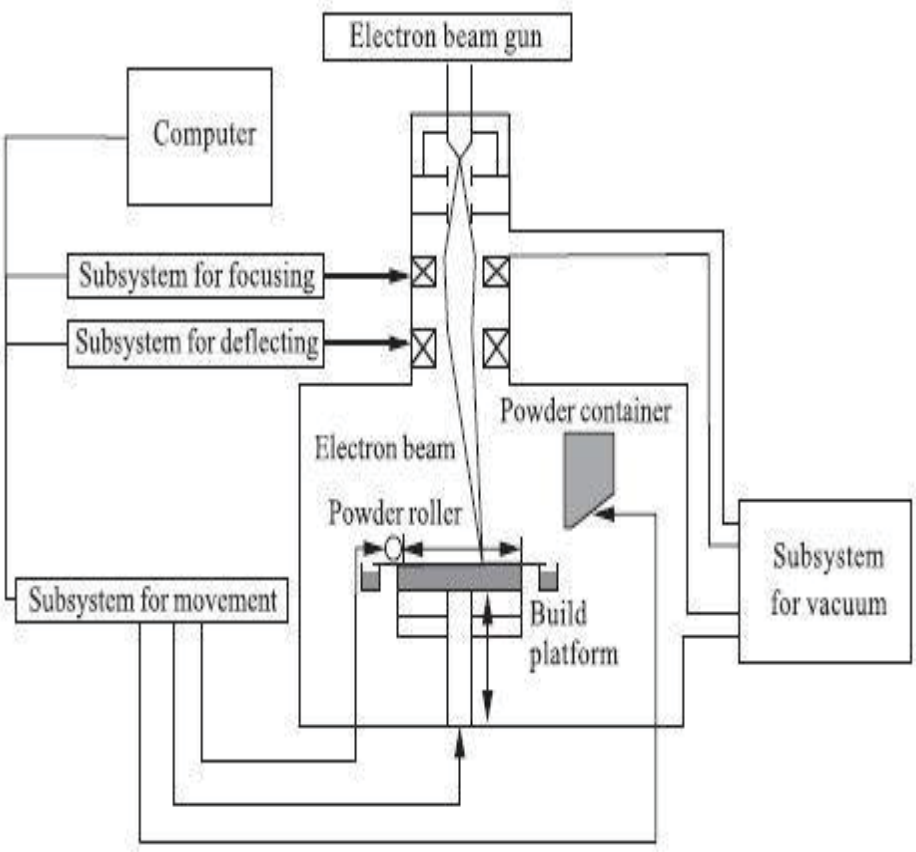

Figure 1.29 EBM Process [61]

The EBM process allows fabrication high quality parts since they are built in a controlled environment and there is an even distribution of temperature. This results in higher mechanical strength. The process is extremely fast and hence its productivity is high [60]

1.8.8 Microextrusion 3d printing

This AM technique was utilized in this project. In this process the material powders are formulated into a paste containing the required amount of binder, solvent, dispersant and lubricant. The paste is then extruded through a nozzle which is capable of moving horizontally. The height of each layer is dictated by the lowering of the bed and the diameter of the extrusion nozzle orifice. This process is repeated until the desired object is obtained. The particles in the layers are held together by the binder present in the paste. This process is shown in Figure 1.30.

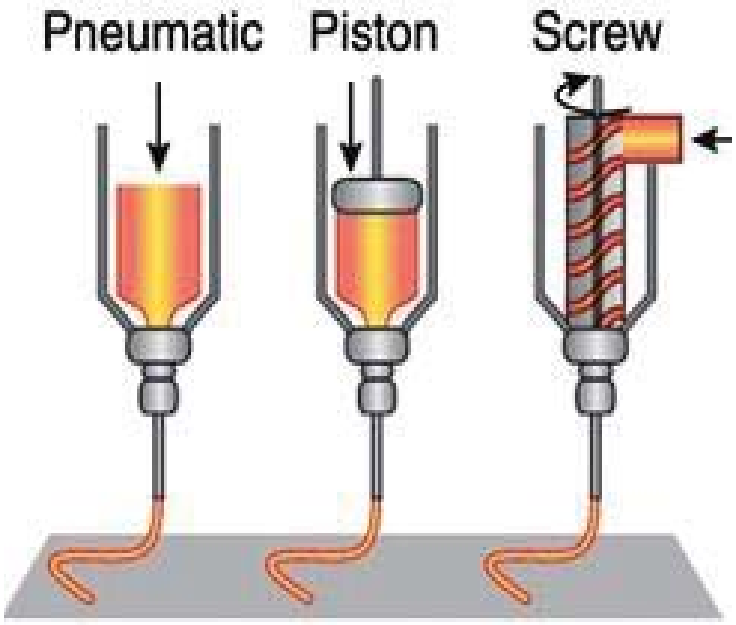

Figure1.30 Micro-extrusion 3d printing [62]

The paste is pushed through the nozzle via either pneumatic pressure or piston, or by a screw mechanism.

The main advantage of this technique is that several heads can be attached to each instrument containing different materials and be printed simultaneously. It is very cost effective, and since the process does not require long intervals or time, it has very high productivity.

1.9 STATEMENT OF PROBLEM

MSOFCs did not manage to go from lab scale to commercialization, even though they had the highest power density, because of two main reasons: MSOFCs were very difficult to fabricate using tape calendaring; and the migration of chromium from lanthanum chromite, the interconnect material adjoining the cathode, inhibited its performance. Also, lanthanum chromite can be densified when fired alone but it is very difficult to densify when it is co-fired with the other components. [24]

The issues Argonne Labs needed to overcome were: [24]

- Development of MSOFC fabrication procedure
- A more sinterable interconnect material
- Cathode material that would be stable at higher sintering temperatures and prevent densification
- Development of ancillary materials such as insulation and manifolds
- Development of quality control methods for improved reproducibility of results and development of nondestructive analysis methods for the MSOFC structure.

A 3d printer can help us to fabricate an MSOFC with less effort than by tape calendaring. It will have higher reproducibility. Since there are as many as five different materials comprising an SOFC, a 3dprinter with a paste extruder will be better suited for the fabrication. Also, since the particle size and solid loading have great effects on the density of the layers, it will be more manageable.

CHAPTER 1

REFERENCES

1) US Energy Information .Retrieved March 13, 2016, from http://beforeitsnews.com/economy/2011/09/world-running-low-on-its-energy-drink-1128439.html
2) BP Statistical Review of World Energy. (2012). Retrieved March13 ,2016 ,from http://edition.cnn.com/2003/WORLD/europe/10/02/global.warming/ 09/21/2011
3) World Energy Investment (2016). Retrieved March 13, 2016, from https://www.iea.org/investment/
4) BP Statistical Review of World Energy 2014, with Christof Ruhl, Chief Economist, BP. (2014). Retrieved March 13, 2016, from http://energypolicy.columbia.edu/events-calendar/bp-statistical-review-world-energy-2014-christof-ruhl-chief-economist-bp
5) NaturalGas.org. (2011). Retrieved March 20, 2016, from http://naturalgas.org/overview/uses-electrical/
6) DWH DIVER. (2015). Web Application: Deepwater Horizon Data Integration Visualization Exploration and Reporting Application, National Oceanic and Atmospheric Administration. Retrieved March 13 ,2016, from http://dwhdiver.orr.noaa.gov
7) User, S. (2010). Global Warming Update. Retrieved March 13, 2016, from https://www.CO_2.earth/global-warming-update

8) H. Davy, Nicholson, W. (1802). *A Journal of natural philosophy, chemistry and the arts.* London ,144

9) Grove, W. (1839). XXIV. On voltaic series and the combination of gases by platinum. *Philosophical Magazine Series 3, 14*(86), 3rd ser., 127-130. doi:10.1080/14786443908649684

10) Fuel Cells CHP. Retrieved May 13, 2016 from http://www.understandingchp.com/appguide/Chapters/Chap4/4-4_Fuel_Cells.htm#Introduction.

11) Solid oxide fuel cell. (2009). Retrieved March 13, 2016, from https://en.wikipedia.org/wiki/Solid_oxide_fuel_cell

12) Ohio Fuel Cell Coalition | Ohio Fuel Cell Symposium: Fuel Cells & The Natural Gas Revolution. (2013). Retrieved March 13, 2016, from http://www.jumpstartnetwork.org/events/2013/Ohio-Fuel-Cell-Symposium.aspx

13) Nerset. W. (1899). U.S. Patent No. US patent 685730. Washington, DC: U.S. Patent and Trademark Office.

14) Huang, K., & Goodenough, J. B. (2009). *Solid oxide fuel cell technology: Principles, performance and operations*. Cambridge, UK: Woodhead Pub.

15) Zink, F., Lu, Y., & Schaefer, L. (2007). A solid oxide fuel cell system for buildings. *Energy Conversion and Management, 48*(3), 809-818. doi:10.1016/j.enconman.2006.09.010

16) Singhal, S. C. (2003). *High-temperature solid oxide fuel cells: Fundamentals, design and applications*. Oxford: Elsevier. UK

17) Siengchum, T. (2009). *Electrochemical oxidation of methane on Ni-doped perovskite anode solid oxide fuel cell* (Master's thesis). Akron: Ohio.

18) Tuller, H. L., & Nowick, A. S. (1975). ChemInform Abstract: DOPED CERIA AS A SOLID OXIDE ELECTROLYTE. *Chemischer Informationsdienst, 6*(20). doi:10.1002/chin.197520021

19) Scott, H. G. (1975). Phase relationships in the zirconia-yttria system. *Journal of Materials Science, 10*(9), 1527-1535. doi:10.1007/bf01031853

20) Yttria-stabilized zirconia. (2009). Retrieved March 13, 2016, from https://en.wikipedia.org/wiki/Yttria-stabilized_zirconia

21) Atkinson, A., Barnett, S., Gorte, R. J., Irvine, J. T., Mcevoy, A. J., Mogensen, M., Vohs, J. (2004). Advanced anodes for high-temperature fuel cells. *Nature Materials, 3*(1), 17-27. doi:10.1038/nmat1040

22) Østergård, M., Clausen, C., Bagger, C., & Mogensen, M. (1995). Manganite-zirconia composite cathodes for SOFC: Influence of structure and composition. *Electrochimica Acta, 40*(12), 1971-1981. doi:10.1016/0013-4686(94)00332-u

23) Haanappel, V., Mertens, J., Rutenbeck, D., Tropartz, C., Herzhof, W., Sebold, D., & Tietz, F. (2005). Optimisation of processing and microstructural parameters of LSM cathodes to improve the electrochemical performance of anode-supported SOFCs. *Journal of Power Sources, 141*(2), 216-226. doi:10.1016/j.jpowsour.2004.09.016

24) Nguyen, Q. M., & Takahashi, T. (1995). *Science and technology of ceramic fuel cells*. Amsterdam: Elsevier Science.

25) DFT plane wave calculations of the atomic and electronic structure of LaMnO3 (001) surface. (2005). Retrieved March 23, 2016, from http://pubs.rsc.org/en/content/articlepdf/2005/cp/b503272e

26) DoITPoMS. (2015). Retrieved March 23, 2016, from http://www.doitpoms.ac.uk/tlplib/fuel-cells/printall.php.

27) Piccardo, P., & Amendola, R. (2009). SOFC's interconnects materials development. In *Proc. Internat. Workshop" Advances and inonvations in SOFCs*.

28) Solid Oxide Fuel Cells. (n.d.). Retrieved March 13, 2016, from http://mypages.iit.edu/~smart/garrear/fuelcells.htm

29) S Skinner, S. J. (2001). Recent advances in Perovskite-type materials for solid oxide fuel cell cathodes. International Journal of Inorganic Materials, 3(2), 113-121. doi:10.1016/s1466-6049(01)00004-6

30) Dhanda, A., Pitsch, H., & O'Hayre, R. (2011). Diffusion impedance element model for the triple phase boundary. *Journal of The Electrochemical Society*, *158*(8), B877-B884.

31) Lee, K. T., & Manthiram, A. (2006). LaSr3Fe3-yCoyO10-δ ($0 \leq y \leq 1.5$) Intergrowth Oxide Cathodes for Intermediate Temperature Solid Oxide Fuel Cells. *ChemInform, 37*(23). doi:10.1002/chin.200623017

32) Cologna, M. (2009). *Advances in the Production of Planar and Micro-Tubular Solid Oxide Fuel Cells* (Doctoral dissertation, University of Trento).

33) C.C. McPheeters, U. Balachandaran, D.W. Dees, S.E.Dorris, J.J. Heiberger, F.C. Mrazek, K.M. Myles, J.J Picciolo, and R.B. Poeppel,(1988) presented at the 33rd International power source symposium, june 13, 1988 Cherry Hill, NJ, Conference 880-665-4, U.S. Department of Energy, Washington , DC,

34) Carolan, M., & James N. Michaels Show more, J. (1990). Morphology of electrochemical vapor deposited yttria-stabilized zirconia thin films. *Solid State Ionics, 37*(2-3), 197-202. doi:10.1016/0167-2738(90)90243-k

35) Bansal, Narottam P., Andrew Wereszczak, and Edgar Lara-Curzio. (2007). Advances in Solid Oxide Fuel Cells II: A Collection of Papers Presented at the 30th International Conference on Advanced Ceramics and Composites, January 22-27, 2006, Cocoa Beach, Florida. Hoboken, NJ: Wiley,

36) Course Websites. (n.d). Retrieved March 13, 2016, from https://courses.engr.illinois.edu/npre201/coursematerial/fuel_cells_and_hydrogen/lecture13tables/Table13.2a.html

37) Https://www.facebook.com/3dprintingcom/. "What Is 3D Printing? How Does 3D Printing Work? Learn How to 3D Print." *3D Printing*. N.p., Web. March 13, 2016.

38) Wohlers, T. T. (2013). *Wohlers report 2013: Additive manufacturing and 3D printing state of the industry: Annual worldwide progress report*. Fort Collins, CO: Wohlers Associates.

39) Cheah, C. M., Chua, C. k., Lee, C. W., Feng, C. and Totong, K. (2005) 'Rapid prototyping and tooling techniques: a review of applications for rapid

investment casting', International Journal of Advanced Manufacturing Technology, Vol.25, pp. 308-320.

40) Armillotta, A. (2006). Assessment of surface quality on textured FDM prototypes. *Rapid Prototyping Journal, 12*(1), 35-41. doi:10.1108/13552540610637255

41) Hague, R., Mansour, S., & Saleh, N. (2003). Design opportunities with rapid manufacturing. *Assembly Automation, 23*(4), 346-356. doi:10.1108/01445150310698643

42) Wohlers, T. T. (2016). *Wohlers report 2013: Additive manufacturing and 3D printing state of the industry: Annual worldwide progress report*. Fort Collins, CO: Wohlers Associates.

43) Hopkinson, N., Hague, R. J., & Dickens, P. M. (2006). *Rapid manufacturing: An industrial revolution for the digital age*. Chichester, England: John Wiley.

44) Pham, D. T., & Dimov, S. S. (2003). Rapid prototyping and rapid tooling—the key enablers for rapid manufacturing. *Proceedings of the Institution of Mechanical Engineers, Part C: Journal of Mechanical Engineering Science, 217*(1), 1-23. doi:10.1243/095440603762554569

45) VG(2012) retrieved March 13, 2016 from http://www.vgkunst.de/en/information/dictionary/dictionary.html

46) Melchels, F. P., Feijen, J., & Grijpma, D. W. (2010). A review on stereolithography and its applications in biomedical engineering. *Biomaterials, 31*(24), 6121-6130. doi:10.1016/j.biomaterials.2010.04.050

47) MakePartsFast. (2013) "How Does 3D Printing - Laser Sintering - Work?" *Make Parts Fast*. N.p., Web. March 13, 2016.

48) Levy, G. N., Schindel, R., & Kruth, J. (2003). Rapid Manufacturing And Rapid Tooling With Layer Manufacturing (Lm) Technologies, State Of The Art And Future Perspectives. CIRP Annals - Manufacturing Technology, 52(2), 589-609. doi:10.1016/s0007-8506(07)60206-6

49) "Overviews." *Fused Deposition Modeling (FDM)*. N.p., n.d. Retrieved March 13, 2016 from http://www.custompartnet.com/wu/fused-deposition-modeling.

50) Grida, I., & Evans, J. R. (2003). Extrusion freeforming of ceramics through fine nozzles. *Journal of the European Ceramic Society, 23*(5), 629-635. doi:10.1016/s0955-2219(02)00163-2

51) Sood, A. K., Ohdar, R., & Mahapatra, S. (2010). Parametric appraisal of mechanical property of fused deposition modelling processed parts. *Materials & Design, 31*(1), 287-295. doi:10.1016/j.matdes.2009.06.016

52) Wohlers, T. (2010) Wohlers Report 2010:Additive Manufacturing state of the industry annual worldwide progress report. ISBN 978-0-9913332-2-6

53) Yves-Christian, H., Jan, W., Wilhelm, M., Konrad, W., & Reinhart, P. (2010). Net shaped high performance oxide ceramic parts by selective laser melting. *Physics Procedia, 5*, 587-594. doi:10.1016/j.phpro.2010.08.086

54) What is the 3DPTM Process? (2012). Retrieved May 13, 2016, from http://web.mit.edu/tdp/www/whatis3dp.html

55) Overviews. (2009). Retrieved March 13, 2016, from http://www.custompartnet.com/wu/3d-printing

56) Khalate, A. A., Bombois, X., Babuška, R., Wijshoff, H., & Waarsing, R. (2011). Performance improvement of a drop-on-demand inkjet printhead using an optimization-based feedforward control method. *Control Engineering Practice, 19*(8), 771-781. doi:10.1016/j.conengprac.2011.02.007

57) Fathi, S., Dickens, P., & Hague, R. (2011). Jetting stability of molten caprolactam in an additive inkjet manufacturing process. *The International Journal of Advanced Manufacturing Technology, 59*(1-4), 201-212. doi:10.1007/s00170-011-3500-6

58) Murr, L. E., Gaytan, S. M., Ramirez, D. A., Martinez, E., Hernandez, J., Amato, K. N., Wicker, R. B. (2012). Metal Fabrication by Additive Manufacturing Using Laser and Electron Beam Melting Technologies. *Journal of Materials Science & Technology, 28*(1), 1-14. doi:10.1016/s1005-0302(12)60016-4

59) Electron Beam Melting. (2012). Retrieved March 13, 2016, from https://sites.psu.edu/johnsedsgn100/2012/11/01/electron-beam-melting/

60) Hanemann, T., Bauer, W., Knitter, R. and Woias, P. (2006) "Rapid Prototyping and Rapid Tooling Techniques for the Manufacturing of Silicon, Polymer, Metal and Ceramic Micro devices. Chapter 4 in " MEMS/NEMS Handbook - Techniques and Applications. Volume 3. Leondes, Cornelius T (eds). Springer.

61) Zhao, J., Cao, W., Ge, C., Tan, Y., Zhang, Y., & Fei, Q. (2009). Research on laser engineered net shaping of thick-wall nickel-based alloy parts. *Rapid Prototyping Journal, 15*(1), 24-28. doi:10.1108/13552540910925036

62) V Murphy, S., & Atala, A. (2014). Components of inkjet, microextrusion and laser-assisted bioprinters. Retrieved March 13, 2016,from http://www.nature.com/nbt/journal/v32/n8/fig_tab/nbt.2958_F2.html

CHAPTER 2

THEORY

2.1 COMPOSITE CATHODE

The electrochemical reactions in a fuel cell take place, as discussed in Chapter 1, at the Three-Phase Boundary (TPB), where electrode, electrolyte and gaseous reagent meet. The most common cathode material used is lanthanum strontium manganite (LSM) [1]. The ionic conductivity of cathode can be enhanced by fabricating a composite cathode comprising of LSM and a material possessing high oxide ion conductivity, for example, YSZ [2].

There are several advantages for the addition of YSZ to the LSM electrode

- It prevents the coalescence of LSM grains, thus improving the long term stability of the electrode [3]. The YSZ particles interpose between the LSM particles and suppress sintering of LSM.
- LSM material used by itself does not adhere well to the electrolyte, thus addition of YSZ improves its adhesion and hence its performance.
- LSM-YSZ composite electrodes have higher performance as the TPB extends into the entire electrode rather than just the interface of the LSM and YSZ.

Figure 2.1 shows the performance for several ratios of LSM/YSZ. The fuel cell achieves highest performance when the composition is 50% LSM and 50 %YSZ.

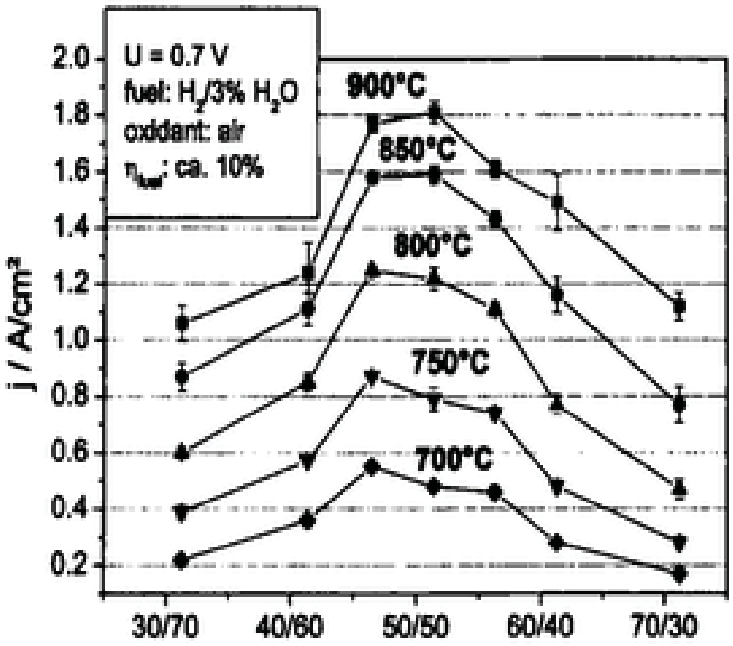

Figure 2.1. Performance based on the ratio of LSM/YSZ as the composite cathode [6]

Stoichiometric LSM has been known to react with YSZ at the interface to form a resistive layer over a wide range of sintering temperatures (1000 – 1400 °C), which reduces the performance of the cell [4]. A-site deficiency in LSM has been known for improved sinterability and enhances its lamination to the electrolyte. An A-site deficiency of 0.5 % can also prevent the insulating layer of lanthanum zirconate, $La_2Zr_2O_7$, from forming [5].

In this study, stoichiometric LSM was blended with 50% YSZ to fabricate the LSM/YSZ (50-50) composite cathode for enhanced lamination with the YSZ electrolyte and to increase the TPB.

2.2 POWDER CHARACTERISTICS

It is extremely important to know the characteristics of a metallic or ceramic powder as they have a strong influence on the particle packing homogeneity of the green sample and

eventually dictate the microstructural evolution during sintering. The main powder characteristics are listed in Table 2.1 [7].

Table 2.1 Powder characteristics that have a significantly affect ceramic processing [7]

Physical characteristics	**Chemical composition**	**Phase composition**	**Surface characteristics**
Particle size	Major elements	Structure (crystalline or amorphous)	Surface structure
Particle shape	Minor elements	Crystal structure	Surface composition
Degree of agglomeration	Trace elements	Phase composition	
Surface area			
Density and porosity			

A particle is a unique unit, which can either be a single crystal or made up of multiple crystals. The pores have to be isolated from each other. A particle cannot be broken down into smaller entities just by ultrasonication; such particles are better referred to as agglomerates [7].

- **Agglomerates**

When particles are held together by surface forces, an agglomerate is formed, which is a cluster of particles held together by a solid bridge or liquid. Agglomerates are usually porous and can be classified into two types [7]:

  - **Soft Agglomerates:** These are held together by weak forces and can be broken down by ultrasonication

- **Hard Agglomerates:** These have particles that are chemically bonded by solid bridges and therefore cannot be broken down. These are undesirable and can lead to microstructural flaws.

- **Particles**

They are made up of a group of small units that move together when the powder is agitated. They can be individual particles, hard agglomerates or even the combination of both. Figure 2.1 shows the different areas of an agglomerate [7].

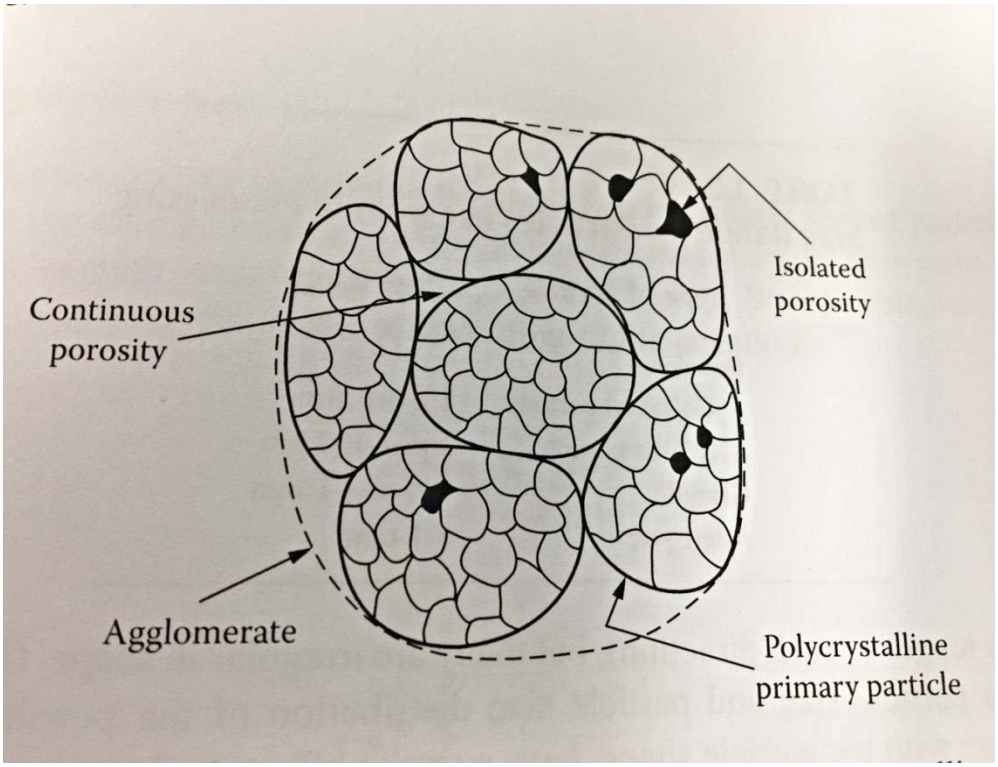

Figure 2.2 Diagram showing various areas of an agglomerate [7]

- **Granules**

These are large agglomerates which are intentionally created by the addition of binders to the powder. They improve the flow characteristics of the powder during processes such as extrusion [7].

- **Flocs**

Particles that are held together in a liquid are called flocs. These can be held together by either weak electrostatic forces or by organic polymers. These are undesirable as they reduce the packing homogeneity in a green sample [7].

- **Colloids**

A system that contains finely divided fine particles dispersed in a liquid is called a colloid. The particles in a colloid system range from 1nm to 1 μm [7].

- **Aggregates**

An aggregate is a mixture that contains fine particles called the bond. An example of an aggregate is concrete, which is constituted of pebbles, and the fine particles in it form the bond [H].

- **Particle size distribution**

Particles in a ceramic powder have a range of particle sizes. In order to get a narrow range of distribution of particle sizes, the powders have to be prepared under controlled conditions, for example, co-precipitation. For a broader range the powders can be milled

in a ball mill. Consolidation and sintering are greatly affected by particle size and particle size distribution [7].

- **Powder characteristics that affect sintering**

Ceramics have a very high melting point and hence their fabrication includes a heat treatment step after the powder has been formed into the required shape to convert it into a dense solid and fuse the particles together [7].

- **Particle size**

The most important aspect for sintering to take place is the particle size. The smaller particles will fuse into the neighboring particles to form a bigger particle. The process of sintering stops when the thermodynamic equilibrium is reached which is when:

$$dA_s / da_b = \gamma_b / \gamma_s \qquad 2.1$$

Where dA_s and da_b are the change in surface area of the grain and change in grain boundary area, respectively, γ_b is the surface energy associated with the creation of a new surface area (particle-pore) and γ_s is the surface energy associated with the creation of a new (grain-grain) boundary area [8].

- **Particle shape and distribution**

The particle shape becomes an important aspect only if it controls the packing of particles in a green system. Equiaxed (symmetrical shape and size) particles are much easier to be packed than non-equiaxed.

For a ceramic to obtain a fully dense state, the ceramic powders should have the following characteristics [9]:

- Smaller particle size (0.1 to 1.0 μm)
- Narrow particle size distribution, so the particles can be stacked better
- Equiaxed shape for easier packing in green state
- Nonagglomerated state as agglomerations can cause constrained sintering and lead to cracks

2.3 CERAMIC PASTE FORMULATIONS

In ceramic processing the additives can either be both organic and inorganic. When the green sample is exposed to heat, the first process that it undergoes is the loss of organic binders and solvents, followed by sintering. The green sample must be heated at a slow rate; the binder loss usually takes place around 400 -700 °C. The inorganic substances are usually not removed in this step and are therefore used in ceramics that do not have strict restrictions on property requirements [7].

- **Solvents**

The solvents that are added to form the paste can be classified into aqueous and organic. These are added to the system to make it more fluid in nature. The ceramic powder does not dissolve but it forms an unstable suspension called a slip that can flow [10].

  - Water is widely used in the ceramic industry. The main advantages of using water are its availability, its non-flammability and its environmental acceptability. Water does have its disadvantages, as it reacts with certain

ceramic powders such as barium titanate, etc. The addition of water also causes the slip to be too viscous and sometimes requires more heating to be removed than organic solvents [10].

- Organic solvents are used instead of water to prevent the issues mentioned above, but they can be flammable and require special procedures for disposable [10].

The solvent used in this study to formulate the extrusion paste was cyclohexanone, which is an excellent homogenizer. Its boiling point is 155.6 °C; solvents with lower boiling points evaporate too rapidly and hence cause cracks [11].

- **Lubricants**

Lubricants are added to ceramic pastes to prevent friction between particles or between particles and die wall. The most common ones are stearic acid, stearates and waxy substances. Polyalkylene glycols have been developed in the last 50 years and offer excellent protection against friction [12].

- **Dispersants**

Dispersants are added in order to stabilize the suspensions and prevent flocculation. The dispersants are added to the formulations in very small amounts. The dispersant functions to keep the ceramic particles suspended in the paste by steric hindrance or steric stabilization. The dispersant must allow the ceramic particles in the slurry to rearrange themselves to obtain a higher green density as the solvent evaporates. Therefore a dispersant ideally helps increase the green density of the ceramic body [13].

□-Terpineol has been documented to increase the green density of YSZ ceramic pastes and thus it was incorporated in this study to formulate the pastes [14].

- **Binders**

Binders are added to the paste formulations to provide strength to the green body, which it does by forming bridges between particles. These also provide plasticity to the material to help in the forming process. Binders are organic substances that are soluble either in water or organic solvents. The most common ones are vinyls, arcylics and ethylene oxides [11].

Binders should have the following qualities [11]:

- It should dissolve in the solvent
- It should burn out without leaving a carbon residue
- It should form a mechanically strong structure on drying

The binder used in this study was METHOCEL A4M (methylated cellulose), since it provided higher green density, which leads to higher sintered density as shown in Figure 2.3 [15]

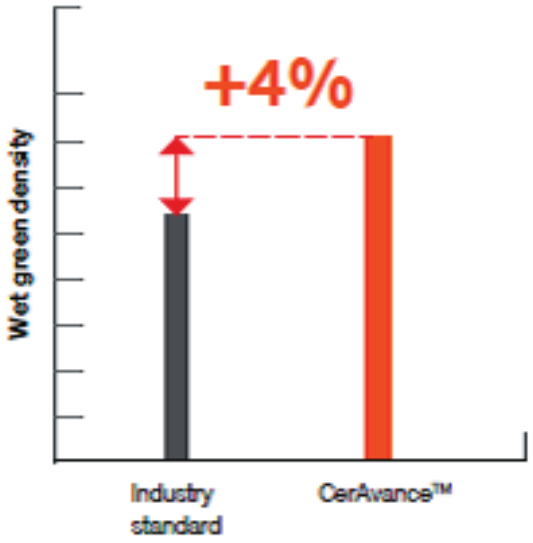

Figure 2.3 Higher green density provided by METHOCEL A4M (DOW CHEMICAL) [15]

- **Plasticizers**

Plasticizers are added to soften the binder in the dry state as they reduce the T_g (temperature at which the polymer transitions from a hard material to a soft material that can flow) of the binder and thus improve the flexibility of the sample in the green state. Because of this, they are very important to add to formulations made for tape casting. Plasticizers are organic substances that have a lower molecular weight than binders [7].

In this study, no plasticizers were added, as the need for flexibility was not a requirement for the extrusion of pastes.

For example, the formulation in Table 2 was used for co-extrusion by Powell et al, where near theoretical densities were obtained for YSZ [16]. The ratios of each constituent were used to derive a formulation for the pastes used in this research.

Table 2.2 A Binder Formulation for YSZ extrusion [16]

Constituents	Mass
Cyclohexanone (solvent)	25.50
Polyvinyl Butyral (binder)	22.50
Dibutyl phthalate (lubricant)	0.90
Stearic acid (surfactant)	0.45

2.3.1 DEBINDING

The process of removal of a binder from a ceramic is known as debinding. It also includes all other additives added to the slurry, such as plasticizer, surfactant, etc. There are two main techniques to perform this process [17]

- Solvent debinding: In this technique, the green sample is immersed in a solvent such as ethanol, heptane etc. to dissolve the binder constituents. This process is very time consuming
- Thermal debinding: This process involves heat treating the sample to decompose the binder. This is widely practiced, as it is very rapid. The heat rate has to be managed since a rapid increase in temperature can cause defects in the sample.

2.3.2 The effect of debinding on properties of fabricated ceramics

- **Shrinkage and Porosity**

The increase in content of high polymer binder in a ceramic paste formulation will reduce the ceramic powder fraction, which will lead to a lower green density and higher binder burnout, so that volume shrinkage also will be high [18].

For example, in work by Jiang *et al.*, Figure 2.4 shows the effect of binder ratio on shrinkage for fused silica mix and zircon mix. The trend is linear and the shrinkage of samples increases as the amount of binder is increased.

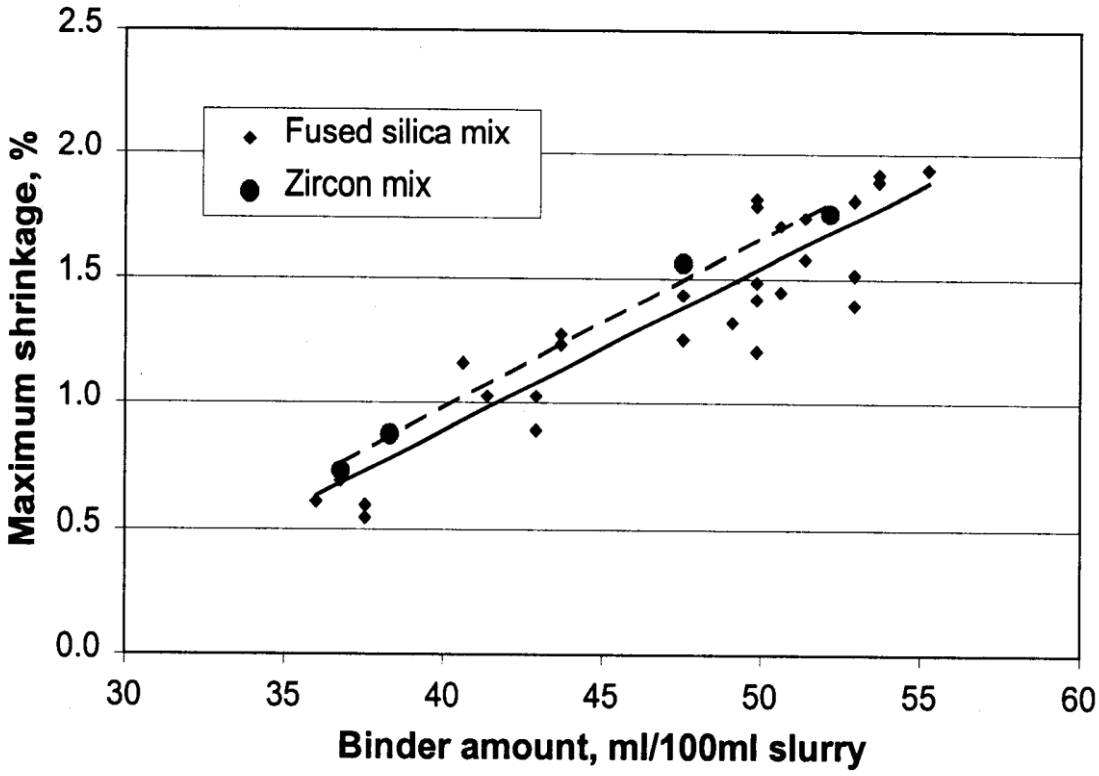

Figure 2.4. Increase in shrinkage of fused silica and zircon mixes with increase in binder ratio [19]

The thermal debinding process is modelled and is shown in Figure 2.5. The organic molecules decompose into smaller gas molecules such as CO_2, CH_4,etc., and escape from the ceramic body. The molecules are removed by either permeation or diffusion, depending on the mean free path of the escaping vapors. The mean free path is dependent up on pressure, molecular weight of gas and pore dimensions. Permeation will occur when pore sizes are large and vapor pressure is high but diffusion will be higher when the pores are small and the pressure is low [20].

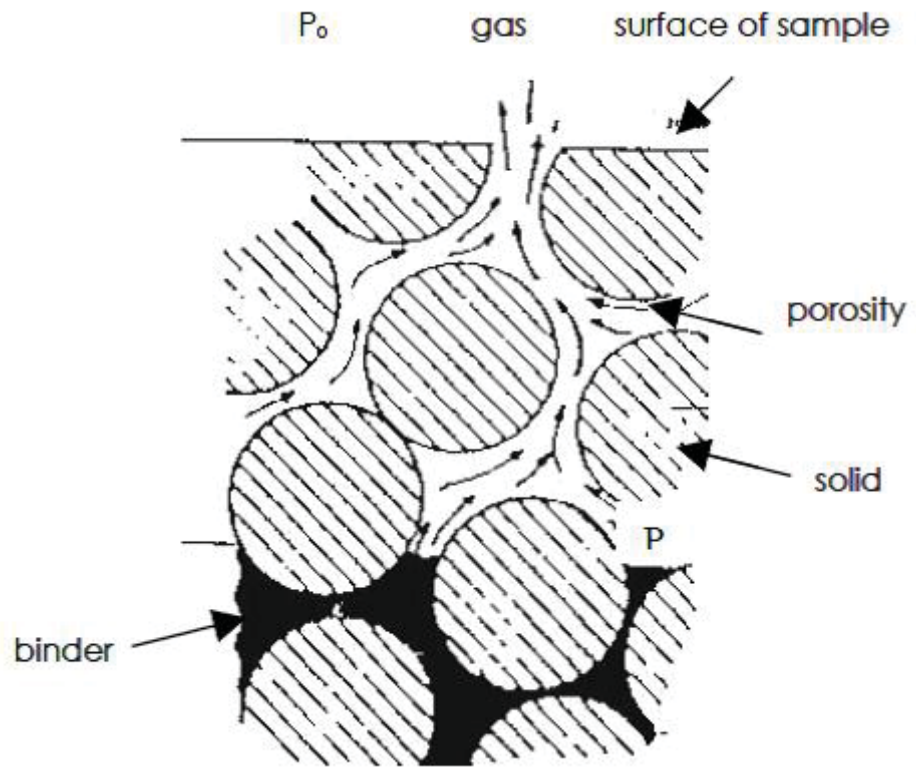

Figure 2.5 Schematic of model for thermal debinding

- **Permeability**

In 1856, Darcy conducted a series of experiments on packs of sand to derive an equation that governs the permeability of a porous substrate [21]. The apparatus used by Darcy is shown in Figure 2.6.

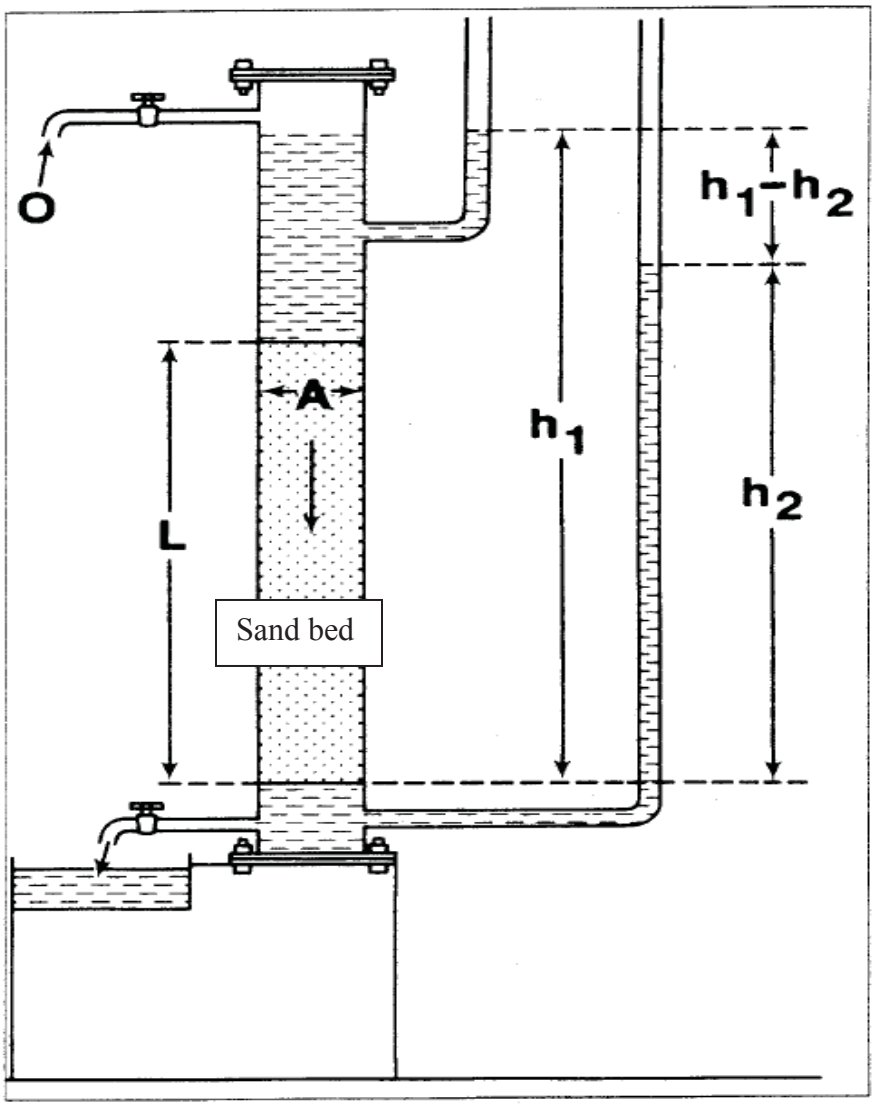

Figure 2.6. Darcy's permeability set-up [22]

Darcy's law states that the flow across two points is a function of pressure difference between the points,the distance between the points and the permeability coefficient of the material [21].

Using the apparatus shown in Figure 3.24 filled with sand, he described rate of water flow Q through the bed as directly proportional to the area of the sand bed, A, and the height difference Δx(in this case,h_1-h_2), which is proportional to the pressure between the inlet and outlet channels. It is inversely proportional to the thickness [21]. The working equation was

$$Q = \frac{CA\Delta x}{L} \qquad 2.2$$

Where Q is the flow rate, A is the area, while $\frac{\Delta x}{L}$ models the pressure gradient. C is a constant of proportionality, usually expressed as $\frac{k}{\mu}$ where μ is the dynamic viscosity and k is the permeability. The equation then becomes [22]:

$$Q = \frac{kA(Pi-Po)}{\mu L} \qquad 2.3$$

The common form equation for Darcy's law is written as

$$-\nabla p = \frac{\mu_g \varepsilon}{K} U_p \qquad 2.4$$

U_p is the velocity of flow, μ_g is the dynamic viscosity, ∇p is the pressure difference, ε is the porosity and K is the permeability. The fuel and airflow through porous electrodes in SOFCs have been described by the use of Darcy's law [23]. The flow is affected by temperature, so Darcy's equation had to be modified to account for the high temperature, which yields the equation below.

$$F = k\,(A / 2\mu l\, p_s)\,(T_s / T)\,(p_i + p_o)\,[p_i - p_o] \qquad 2.4$$

Where, F = gas flow rate in volume at STP, p_s is the standard pressure, T_s is standard temperature, k is the permeability constant for the material, A is the area, μ is dynamic viscosity of the working fluid, in this case argon gas, *l* is the thickness of the sample, T is the test temperature in Kelvin, p_i is inlet gas pressure and p_o is outlet gas pressure [24].The dynamic viscosity for argon, $\mu=2.21\text{x}10^{-5}\text{N.s/m}^2$, was used for permeability measurements.

2.4 SINTERING

The final microstructure of the sintered sample is greatly depended upon the processing variables such as temperature, particle size, applied pressure, particle packing, composition and sintering atmosphere. [25]

2.4.1 There are four categories of sintering which are based on the composition:

- **Solid-state sintering:** It includes heating the green body to a temperature, which would be around its melting temperature. There is no liquid present and the atomic particles fuse together, which leads to the reduction in porosity [25].
- **Liquid-phase sintering:** In this type of sintering, a small amount of liquid is present at the sintering temperature, which enhances the densification at a much lower temperature. [25].
- **Vitrification:** In this process, a large amount of liquid is present. It is usually more than 25% of the original solid volume at the sintering temperature. Such large amounts of liquid fill up all the pores, thereby producing a very dense

material. Vitrification is important for the production of ceramics from readily available raw materials like clay.[25]

- **Viscous sintering:** This type of process is used in the manufacturing of glass. A certain amount of glass is heated until it softens and begins to flow. Densification is achieved by the viscous flow of glass due the influence of surface tension.[25]

The driving force behind sintering is the reduction in surface free energy. Although the reduction in surface free energy is very small when compared to the reduction of energy due to other chemical reactions, for sintering the mass only has to be transported extremely small distances. Figure 2.7 illustrates the different mechanisms involved in a two particle sintering.

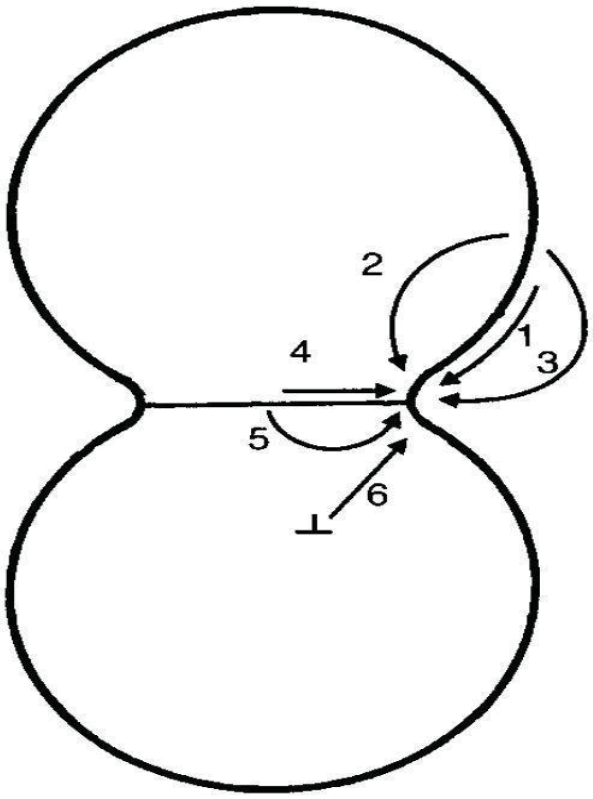

Figure 2.7 Schematic representation of sintering mechanism [25]

1. Surface diffusion
2. Lattice diffusion
3. Vapor transport
4. Grain boundary diffusion
5. Lattice diffusion from the grain boundary
6. Plastic flow (by dislocation motion)

In Figure 2.6 above, mechanisms 1, 2 and 3 only produce microstructural change without causing shrinkage and do not lead to densification. The densifying mechanisms are 4, 5 and 6, as they remove material from the grain boundary region. Grain boundary diffusion and lattice diffusion from the grain boundary to the neck have the highest impact on densification in ceramics. Plastic flow is more pertinent in the sintering of metal powders. It is the dislocation motion that can cause neck growth and densification through deformation of particles due to sintering stress. [25]

2.4.2 Sintering Aid

The most important component of an SOFC is the electrolyte. It has to be as close to theoretical density as possible, but at the same time, it should have good ionic conductivity and stability. The most common electrolyte used is YSZ. Since our design is complex, we cannot apply pressure to create a dense electrolyte; we have to employ sintering aids. Sintering aids can be used to enhance densification and to reduce sintering temperature. The key requirement for a sintering aid is that the melting temperature of the aid has to be below the sintering temperature. The presence of the liquid phase is responsible for the enhancement of the densification. Transition metal oxides have been

proved effective sintering promoters, but they can also interfere with the other characteristic properties of an electrolyte [26].

Studies have proved that alumina to be a very good sintering aid for YSZ. In the work of Hasan.E *et al.,*the addition of 0.77 wt% Al_2O_3 to YSZ electrolyte did not reduce the performance of the cell and improved densification. The performance data is plotted in Figure 2.8.

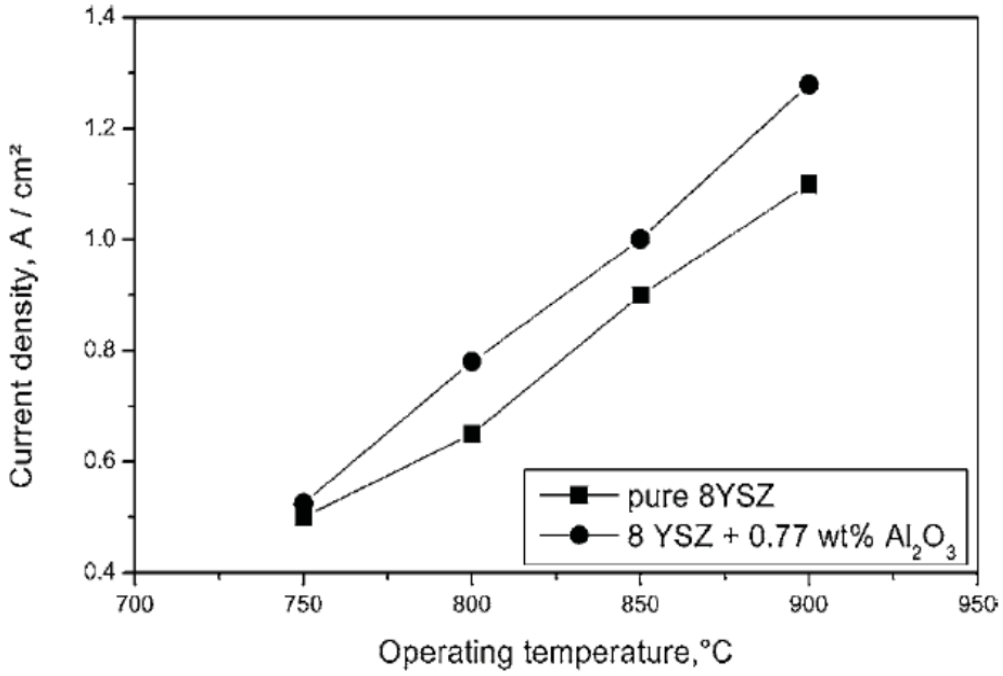

Figure 2.8 Performance of SOFC with alumina doped YSZ [27]

The improved performance of the cell can be attributed to the low helium leakage rate shown in Figure 2.8.

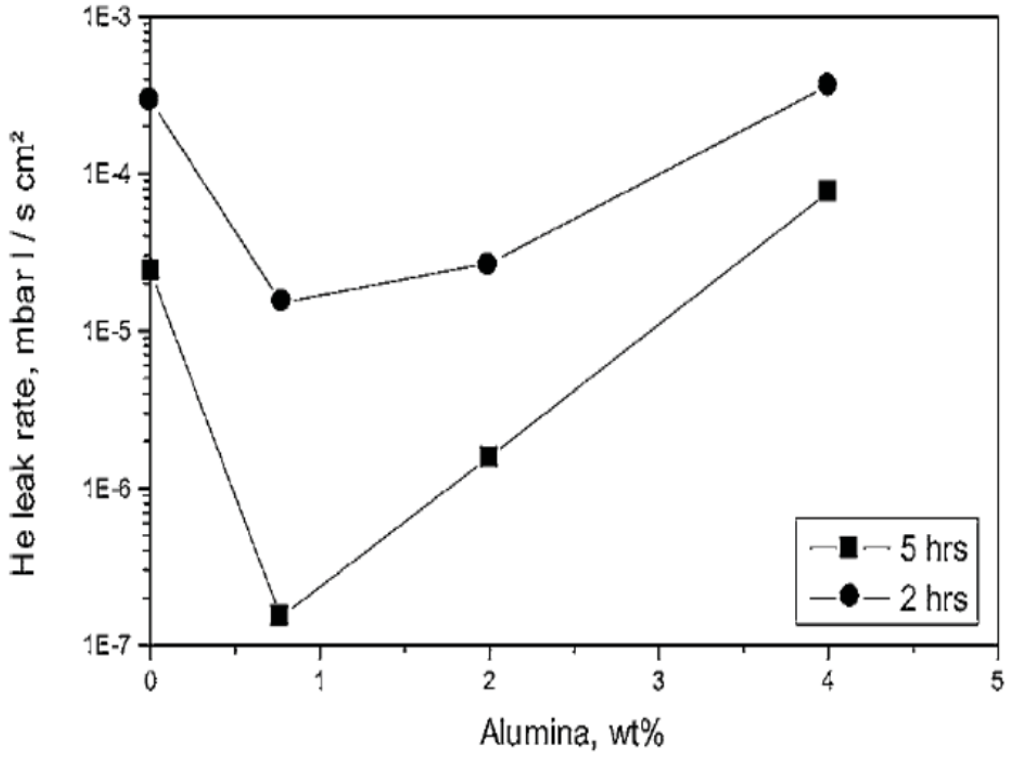

Figure 2.8 Helium leakage rate of alumina doped YSZ [27]

YSZ powder with particle size between 0.25 μm and 0.3 μm has the highest sinterability; smaller particle size can increase agglomeration activity and reduce sinterability. [27]

2.4.3 Constrained sintering

No sintering process is independent; in other words, almost all sintering processes are constrained. For example, even when we consider the sintering of a pure single phase powder, there can still be considered constrained sintering because of the presence of agglomerates in the green sample.

When we consider constrained sintering, there are 4 important cases to consider as shown in the Figure 2.9 below [28].

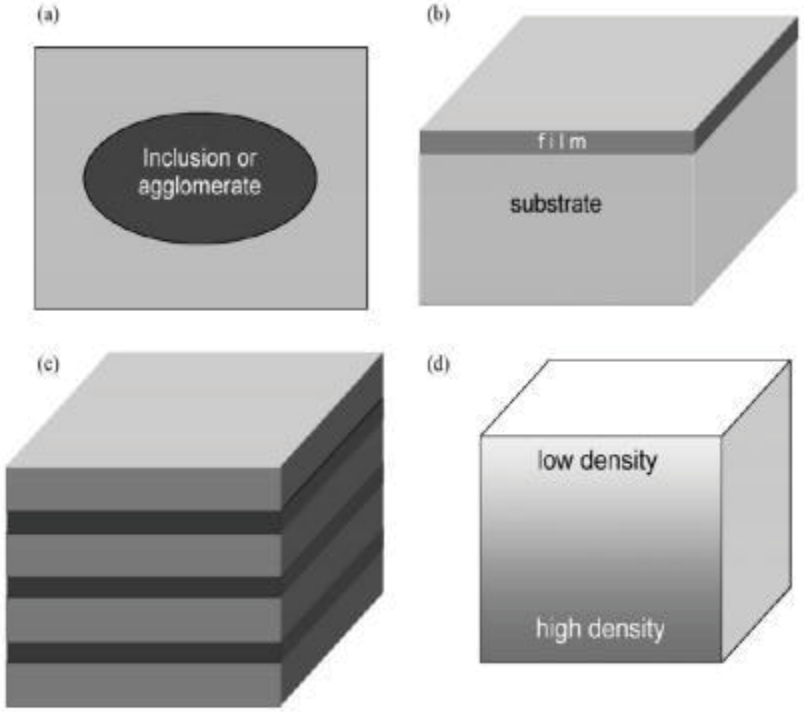

2.9 Schematic illustrations of structures that will undergo differential densification

a) In sintering of composites the particles will densify around the second phase material that may be present such as platelets or rods etc.

b) When a thin film undergoes sintering on a rigid substrate, the sintering film is placed in biaxial tension by the substrate and the majority of the densification will only occur in the vertical direction

c) When a series of layered green structures undergo sintering, they will shrink at different rates and hence the layers will constrain each other and cause stresses.

d) Constraints can also arise in the same phase material due to the presence of agglomerates in the samples, as areas of different densities will differ in sintering.

- **Constrained sintering of multilayers**

In the case of a cosintering process where we have multiple green layers, the difference in sintering rates of individual layers can result in transient stresses which can cause a reduction in the densification of individual layers. The stresses caused by such differential sintering can result in flaws in the structure, such as cracking, warping or delamination. These flaws can be overcome to a certain extent by tailoring the powder characteristics, green density and sintering program [28].

CHAPTER 2

REFERENCES

1) N.Q. Minh, T. Takahashi, Science and Technology of Ceramic Fuel Cells, Elsevier, Amsterdam, 1995

2) Murray, E. P. (2002). Electrochemical performance of (La,Sr)(Co,Fe)O3–(Ce,Gd)O3 composite cathodes. Solid State Ionics, 148(1-2), 27-34. doi:10.1016/s0167-2738(02)00102-9

3) Hayashi, K. (1997). Sputtered La0.5Sr0.5MnO3–yttria stabilized zirconia composite film electrodes for SOFC. Solid State Ionics, 98(1-2), 49-55. doi:10.1016/s0167-2738(97)00098-2

4) Stochniol, G., Syskakis, E., & Naoumidis, A. (1995). Chemical Compatibility between Strontium-Doped Lanthanum Manganite and Yttria-Stabilized Zirconia. Journal of the American Ceramic Society, 78(4), 929-932. doi:10.1111/j.1151-2916.1995.tb08416.x

5) Bansal, N. P., Singh, P., Widjaja, S., & Singh, D. (2011). *Advances in solid oxide fuel cells VII: A collection of papers presented at the 35th International Conference on Advanced Ceramics and Composites, January 23-28, 2011, Daytona Beach, Florida*. Hoboken, NJ: Wiley

6) Lara-Curzio, E., & Readey, M. J. (Eds.). (2009*). 28th International Conference on Advanced Ceramics and Composites B: Ceramic Engineering and Science Proceedings, Volume 25 (No. 4). John Wiley & Sons.*

7) Rahaman, M. N. (2007). *Ceramic processing*. Boca Raton, FL: CRC/Taylor & Francis.

8) I.B. Cutler, in Ceramic Processing Before Firing (G.Y. Onada, Jr and L.L, Hench eds.). John Wiley, New York, 1978, pp 21-29

9) Barringer, E. A., & Bowen, H. K. (1982). Formation, packing, and sintering of monodisperse TiO2 powders. Journal of the American Ceramic Society, 65(12).

10) Shanefield, D. J. (2013). Organic additives and ceramic processing: with applications in powder metallurgy, ink, and paint. Springer Science & Business Media.

11) Sōmiya, S. (2013). Handbook of advanced ceramics: Materials, applications, processing, and properties. Amsterdam: Academic Press, imprint of Elsevier

12) PAGs are Rising to the Top of the Synthetic Market. Retrieved November 23, 2016, from http://www.machinerylubrication.com/Read/930/pag-synthetic-oil

13) Maiti, A. K., & Rajender, B. (2002). Terpineol as a dispersant for tape casting yttria stabilized zirconia powder. Materials Science and Engineering: A, 333(1), 35-40.

14) Maiti, A., & Rajender, B. (2002). Terpineol as a dispersant for tape casting yttria stabilized zirconia powder. Materials Science and Engineering: A, 333(1-2), 35-40. doi:10.1016/s0921-5093(01)01821-4

15) Retreived December 1st 2013, from : http://msdssearch.dow.com/PublishedLiteratureDOWCOM/dh_0903/0901b80380903f18.pdf?filepath=dowwolff/pdfs/noreg/787_00019.pdf&fromPage=GetDoc

16) Powell, J., Assabumrungrat, S., & Blackburn, S. (2013). Design of ceramic paste formulations for co-extrusion. Powder Technology, 245, 21-27. doi:10.1016/j.powtec.2013.04.017

17) Hashmi, S. (2016). Introduction to Finish Machining and Net-Shape Forming. (2016). Comprehensive Materials Finishing, Xix-Xx. doi:10.1016/b978-0-12-803581-8.09024-x

18) Cho, B. (2007). *U.S. Patent No. US8153259 B2*. Washington, DC: U.S. Patent and Trademark Office.

19) Jiang, J., & Liu, X. (2003). *U.S. Patent No. US6651730 B2*. Washington, DC: U.S. Patent and Trademark Office.

20) Calvert, P., & Cima, M. (1990). Theoretical Models for Binder Burnout. Journal of the American Ceramic Society J American Ceramic Society, 73(3), 575-579. doi:10.1111/j.1151-2916.1990.tb06555.x

21) Amao, A. M. (2007). *Mathematical model for Darcy Forchheimer flow with applications to well performance analysis* (Doctoral dissertation, Texas Tech University).

22) M Sc Petrophysics Course Notes By Paul Glover Pdf - Free Ebooks Download. (n.d.). Retrieved November 23, 2016, from http://ebookbrowse.in/pdf/title/m-sc-petrophysics-course-notes-by-paul-glover.html

23) B.A.Haberman, J.B. Young (2004); Three-dimensional simulation of chemically reacting gas flows in the porous support structure of an integrated-planar solid oxide fuel cell; Hopkinson Laboratory, Cambridge University Engineering Department, Cambridge CB2 1PZ, UK.

24) Jena, A., & Gupta, K. (2008). Characterization of Pore Structure of Electrodes of Solid Oxide Fuel Cells. Bansal/Advances Ceramic Engineering and Science Proceedings Advances in Solid Oxide Fuel Cells: Ceramic Engineering and Science Proceedings, Volume 26, Number 4, 169-176. doi:10.1002/9780470291245.ch19

25) Rahaman, Mohammed, and Lutgard Jonghe.(2003) *Handbook of Advanced Ceramics*. By Shigeyuki Sōmiya. Amsterdam: Academic,. 187-201

26) Kleinlogel C, Gauckler L J. Solid State Ionics, 2000, 135 ... (n.d.). Retrieved March 23, 2016, from http://www.oalib.com/references/18040601

27) Hassan, A. A. E., Menzler, N. H., Blass, G., Ali, M. E., Buchkremer, H. P., & Stöver, D. (2002). Influence of alumina dopant on the properties of yttria-stabilized zirconia for SOFC applications. Journal of materials science, 37(16), 3467-3475.

28) Green, D. J., Guillon, O., & Rödel, J. (2008). Constrained sintering: A delicate balance of scales. Journal of the European Ceramic Society, 28(7), 1451-1466.D.

CHAPTER 3

MATERIALS AND EXPERIMENTAL METHODS

The purpose of this research was to study and 3d print an SOFC via microextrusion. This required understanding the effects of binder and solvent on porosity, shrinkage, conductivity and permeability of various components of the cell. The resulting 3d printed SOFC was tested for performance and analyzed.

3.1 SOFC POWDERS

The cell was made of Nickel Oxide-Yttria Stabilized Zirconia (NiO-YSZ) composite for the anode and Yttria Stabilized Zirconia (YSZ) for the ion-conducting electrolyte and a composite made of 50% Lanthanum Strontium Manganite (LSM) and 50% Yttria Stabilized Zirconia for the cathode. These materials were bought from NexTech materials, Ltd and Sigma Aldrich.

- **Electrolyte powder**

The electrolyte was made of YSZ8; (Yttria-Stabilized Zirconia 8 mole %), with composition $(Y_2O_3)_{0.08}(ZrO_2)_{0.92}$. The BET surface area was 7.6m^2/g. The mean diameter of the particles in the YSZ powder was 0.64 μm.

- **Cathode powder**

The cathode layer was made from a composite of 50% LSM20; Lanthanum Strontium Manganite (20%), with composition $(La_{0.80}Sr_{0.20})_{0.95}MnO_{3-\delta}$and 50% YSZ8; (Yttria-Stabilized Zirconia 8 mole %), with composition $(Y_2O_3)_{0.08}$ $(ZrO_2)_{0.92}$. The BET surface

area was 4.4m^2/g of the LSM powder. Note that the LSM powder is deliberately A-site deficient.

- **Anode powder**

    1. The anode layer was made using NiO-YSZ; Nickel Oxide – Yttria Stabilized Zirconia, composed of 40% NiO-60%YSZ by weight. The BET surface area was 2.1m^2/g.

    2. The anode layer was also fabricated using NiOnanopowders, with particle size < 50 nm. The density of the NiOnanopowders was 6.67 g/mL. The NiOnanopowder material was mixed with 60% YSZ.

3.2 PASTE FORMULATION

The paste was formulated using the materials listed in Table 3.1. The binder that was used was METHOCEL^{TM} A4M, Methylcellulose; it was bought from Dow Chemical Company, Midland, Michigan. The solvent used was cyclohexanone that was available in the lab. Polyalkylene glycol was used as a lubricant; the product is manufactured by *FJC* Universal. The dispersant used in the formulation was □-Terpineol with density of 0.93 g/mL; it was obtained from Sigma Aldrich. The sintering aid was only added to the formulation of YSZ paste which was alumina with BET surface area of 150 m^2/g. It was obtained from Alfa Aesar.

Table 3.3. Paste formulation

Component	Amount
Binder (methoxy cellulose)	1%-9% of ceramic content
Solvent (cyclohexanone)	1g – 8g
Lubricant (Polyalkylene glycol)	0.8 g
Dispersant (Terpineol)	0.48 g
Ceramic	16 g
Sintering aid (electrolyte)	0.77 wt% alumina (58 Å)

Agglomerates in the powder needed to be broken down and this was done by placing the powders in an ultrasonicator. The solvent used was methanol.

3.3 FLACKTEK SPEEDMIXER

The preparation of pastes was done in a FlackTekSpeedmixer (Figure 3.1). The speed mixer was provided by Dr. Choi from University of Akron. The powders were all transported to Akron, where they were added in proportions mentioned in Table 3.1. The cup sizes used were 40 g and also obtained from FlackTek.

- Mixing was performed by dual rotation of the cup, which is why it is also called dual asymmetric centrifugal mixing. It has several advantages over traditional mixing equipment such as ball mixing. Samples mixed via speedmixer have uniform mixing and hence increase reproducibility. Sample preparation is done in a plastic container, thereby reducing cleanup time. Several substances can be mixed, such as pastes, oils, liquids, creams etc., which causes bladeless and thereby reducing material loss. Another merit is that it can be programmed to produce matching series of samples. Additionally, the samples are air bubble free since the mixing and deaeration can be achieved simultaneously by using the dual asymmetric centrifugal technology. Finally, the speedmixer does not require a counterweight.

Figure 3.1 The SpeedMixer™ DAC 150.1 FVZ-K was used to prepare the pastes [1]

Figure 3.2 shows a sample of YSZ paste of printable viscosity. Due to the unavailability of a viscometer, the pastes were qualitatively analyzed to make sure they could be extruded.

Figure 3.2. Printable YSZ paste (particles are well suspended without any presence of segregation or agglomeration)

All samples were mixed at 2500 rpm for 5 minutes. The pastes were then transported back to Youngstown State University and had to be printed as soon as possible to prevent the agglomeration of the particles in paste or its densification due to the loss of solvent.

3.4 HYREL 3D PRINTER

The 3d printer used for our study was the ENGINE SR (Standard Resolution) ^{TM} (Figure 3.3). It is manufactured by Hyrel 3D of Norcross, GA. the HYREL platform provides an open interface that allows users to experiment with different materials [3].

Figure3.3.Hyrel 3d printer ENGINE SR [2]

The original printer setup did not have the capability for extrusion. This required the acquisition of the EMO 25 Extruder head. The original nozzles dragged the pastes on printing, however. The nozzle was replaced with a nozzle fabricated in-house, consisting of a LEUR needle of pore size 0.8 mm, as shown in Figure 3.4.

Figure 3.4. In house fabricated nozzle

3.4.1 Repetrel

The graphic user interface used by Hyrel 3d printers is called Repetrel. The main screen that appears is shown in Figure 3.5. Repetrel does come installed on the machine and can be used to control the machine from the touch screen pad located at the base of the instrument. However, early in this research program, Youngstown State University requiredthat all computers on campus that are network-connected must be updated to Windows 7.As a result, when the system was updated, the touch screen on the machine failed, so that the printer graphical interface had to be accessed through an external monitor.

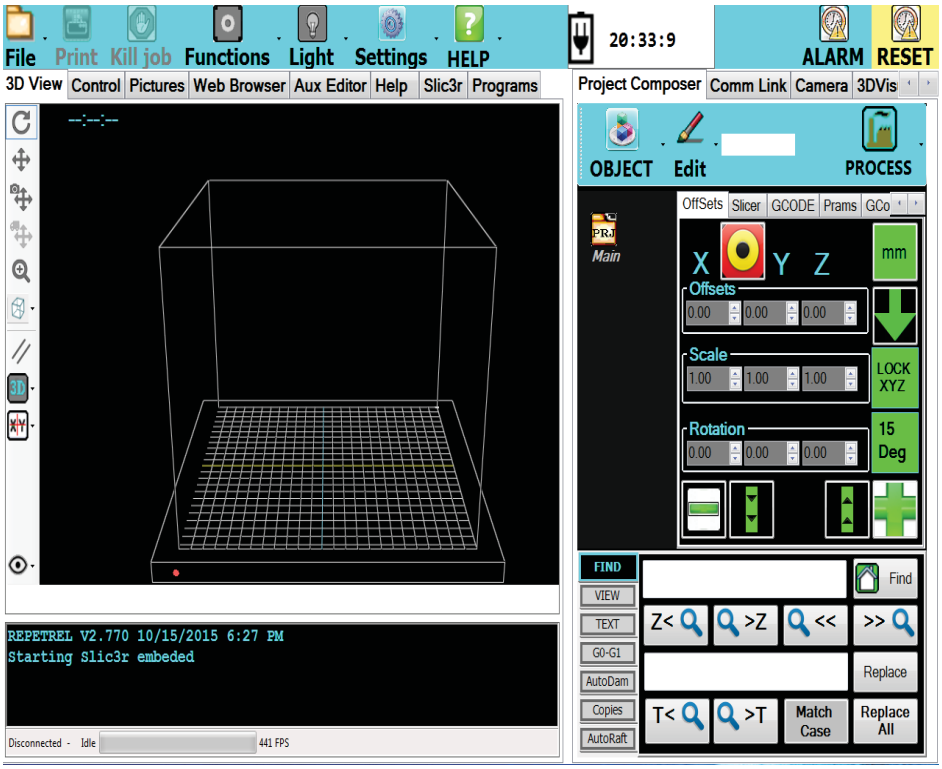

Figure 3.5. Repetrel user interface [3]

3.4.2 Printing

The paste was transferred from the 40 g container to the EMO extruder cartridge via a plastic syringe to prevent any large agglomerated particles from entering it. The agglomerated particles prevented the smooth rotation of the piston and hence the smooth flow of the paste from it.

SolidWorks software was used to create the image files of the samples to be printed. The design files in (.stl) format were transferred to the Hyrel machine. The .stl file is loaded into MeshLab to heal the file (remove reference lines, resolve duplicate vertices, etc.). The healed .stl file is then brought into Slic3r to slice it (convert it into the G-code that drives the printer).

The default setting for the speed moves was 25 mm/s, which was too high for this application, so it was lowered to 5 mm/s for all movements.

The various SOFC components were printed disks of 23 mm diameter and height 1.6 mm. The nozzle diameter was 0.8 mm. The manufacturer claimed to support layer heights of 0.25 microns but, their preferred thickness ranged from 250-400 μm for every layer when building plastic parts. For extrusion materials their recommended thickness was 500 μm. The bottom fill pattern was concentric and then rectilinear, to prevent pinholes in the sample. The build time for each component layer was 5 min and 13 s in other words the printer was configured to print 2 cm^2/min. The cartridge and nozzle needed to be cleaned after every run to avoid contamination of the subsequent printing.

The support material was set at zero. The resolution reported by the manufacturer was about 5 μm in the x- and y-directions, and 0.5 μm in the Z. The repeatability was about 25 μm in the x and y, and about 10 μm in the Z axis.

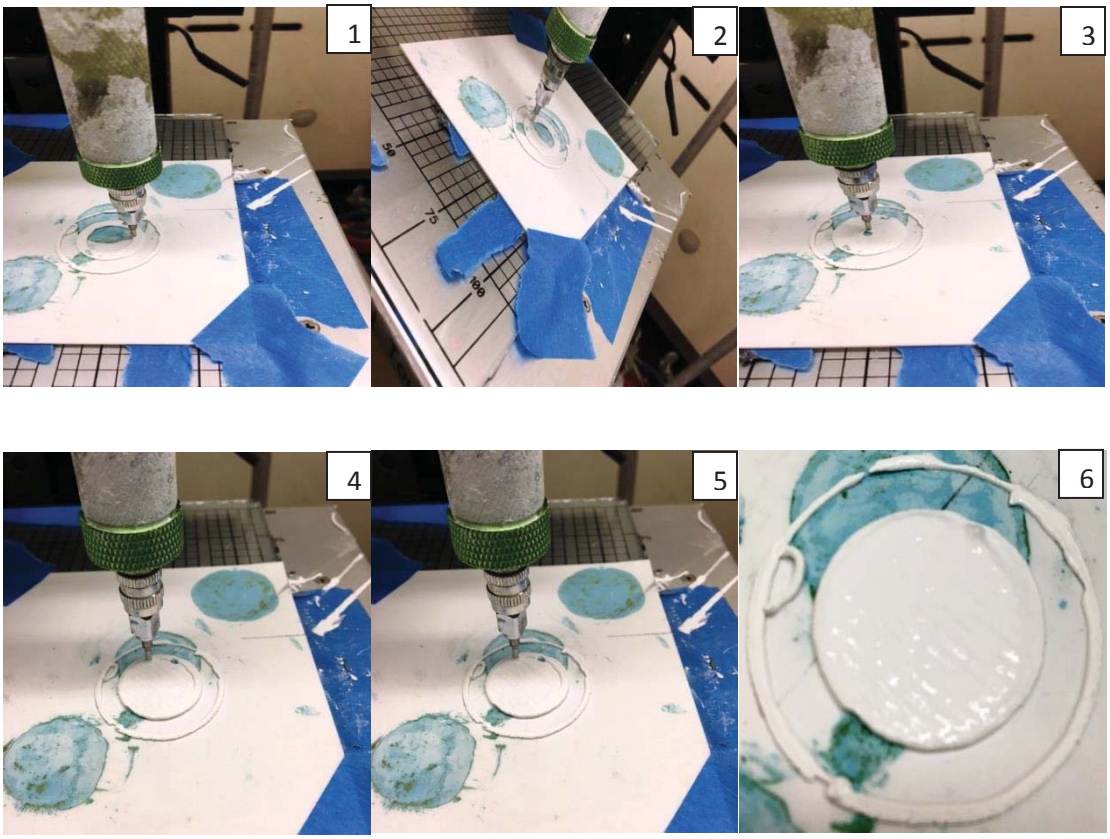

Figure 3.6. YSZ printing

The disk samples were printed on top of a thin square alumina plate, which was held in place with the help of painter's tape on the glass bed.

The printed samples were fired at 1400 °C using a ramp rate of 3 °C/ min for 2 h. A more mutually compatible sintering temperature of 1300 °C was later substituted into the procedure.

3.5 THE PROBOSTAT™

The electrochemical cell used to derive current-voltage curves for the 3d printed SOFC is called the ProboStat™(Figure 3.7), manufactured by Norwegian Electro Ceramics AS (NorECs). It was obtained fromNextech (Fuel Cell Materials), Lewis Center, Ohio. A

ProboStat^{TM} system offers a wide variety of tests for measurements of electrical properties, transport parameters, and kinetics of materials, solid/gas interfaces and electrodes under controlled atmospheres at high temperatures. A button cell set-up was used for our experiments. A button cell solid oxide fuel cell is typically a thin circular solid electrolyte of one to three centimeters in diameter with an anode pasted on one side and a cathode on the other [4]. The ProboStat^{TM}was placed inside a vertical tube furnace with a diameter of 4 cm and length of 28 cm (Figure 3.8). The power supply for the oven was 220 volts and 20 amps. The controller of the oven is equipped with two control units; one is used to set the temperature of the oven and the other is set to be a safety shut-off. The alarm (no sound) feature can prove to be very useful in case there is a leak between anode and cathode compartments, which would cause the temperature to rise. When the temperature reaches the set temperature set of the alarm, the furnace is automatically shut off. We operated the button cell at 800^{0}C with a 100^{0}C runaway cutoff, so the alarm would shut down the system at 900 ^{0}C.

Figure 3.7. The Probostat™[5]

Figure 3.8. Typical setup with a furnace [5]

3.6 ARCHIMEDES POROSITY EXPERIMENT SET UP

It was essential for our study to be able to do porosity measurements. The porosity of only fired samples was measured, as the capability to perform porosity testing on green samples was not available. The dry weight of fired samples was noted. The samples were then immersed in boiling water for about an hour to make sure the water seeped into all the pores of the sample. A wet paper towel was used to wipe off the excess water from the samples and the weight of the samples was noted again. The weight of the samples was also recorded when the samples were submerged completely under water.

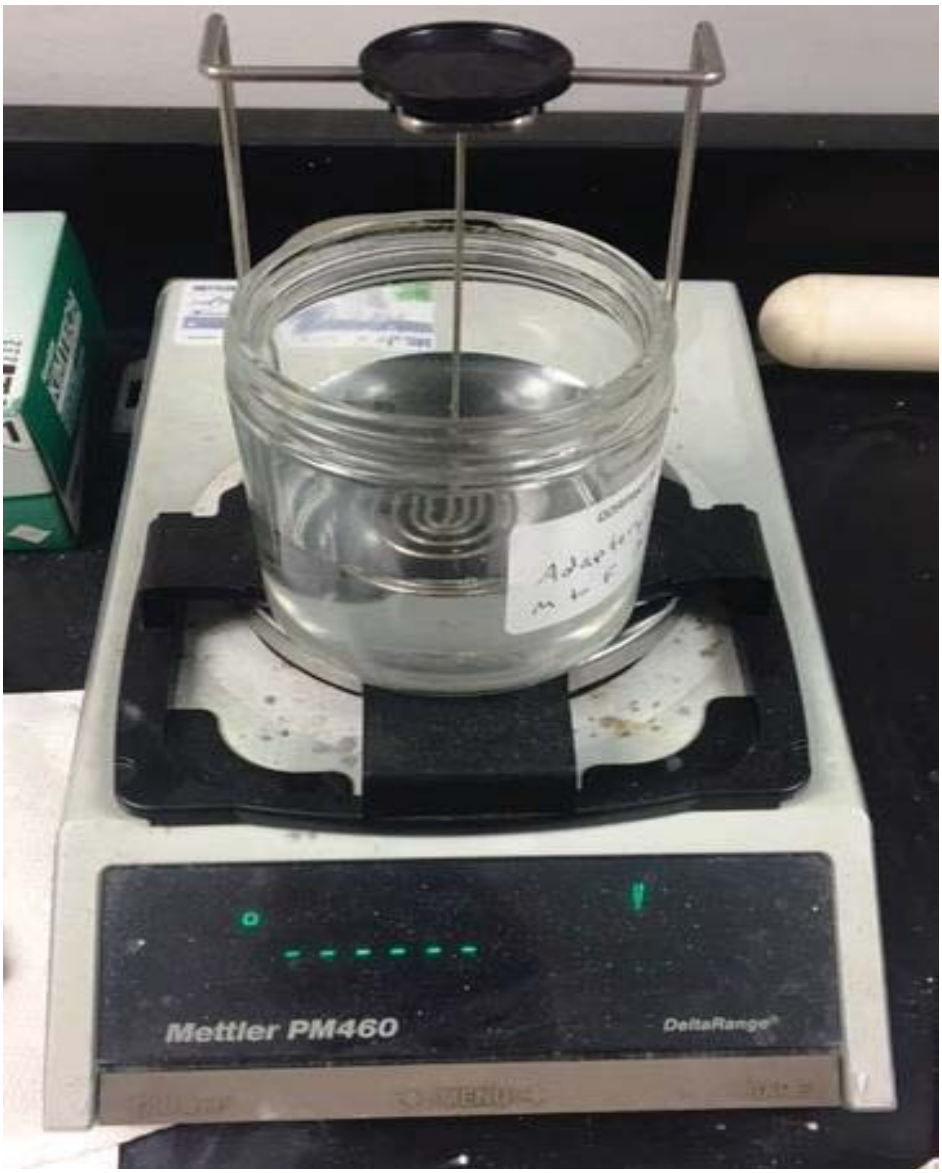

Figure .3.9 Archimedes porosity set-up for hydrostatic weighing

The porosity was calculated by the formula given below

$$N_t\,(\%) = \frac{W_1 - W_s}{W_1 - W_2} \times 100 \qquad 3.1$$

Where

- W_1 is the weight of the sample saturated with water
- W_2 is weight saturated obtained by hydrostatic weighing
- W_s is the dry weight of the sample

3.7 SHRINKAGE ANALYSIS

The dimensions of both green and fired samples were measured using a micrometer. The shrinkage was obtained using the formula given below.

$$Shrinkage = \frac{Wet\ Diameter - Fired\ Diameter}{Wet\ Diameter} \text{ X } 100 \qquad 3.2$$

3.8 CONDUCTIVITY MEASUREMENT

YSZ is an ionic conductor whereas Ni-YSZ and LSM-YSZ are both electronic conductors. The set-up was different for measuring the electronic and ionic conductivities.

3.8.1 Electronic Conductivity

The four point probe method was for electrical conductivity measurements. This set-up was used for measuring the conductivities of highly conductive samples such as Ni-YSZ or LSM-YSZ.

In order to perform this test, bars of the samples were fabricated.

The dimensions of the bars were recorded. The bar was then attached by means of platinum wires. The point of contact of every platinum bar was coated with Liquid Bright Platinum and then fired at 1000 °C in order to ensure a stable contact was created.

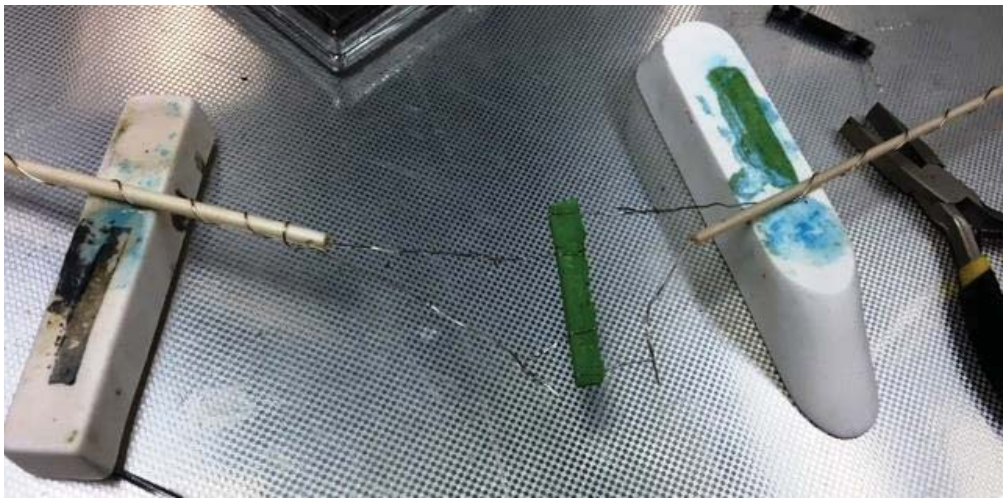

3.10. Ni-YSZ conductivity bar for 4 point test

The sample bar was then transferred to a tube furnace (800 °C) and set-up according Figure 3.11 shown below:

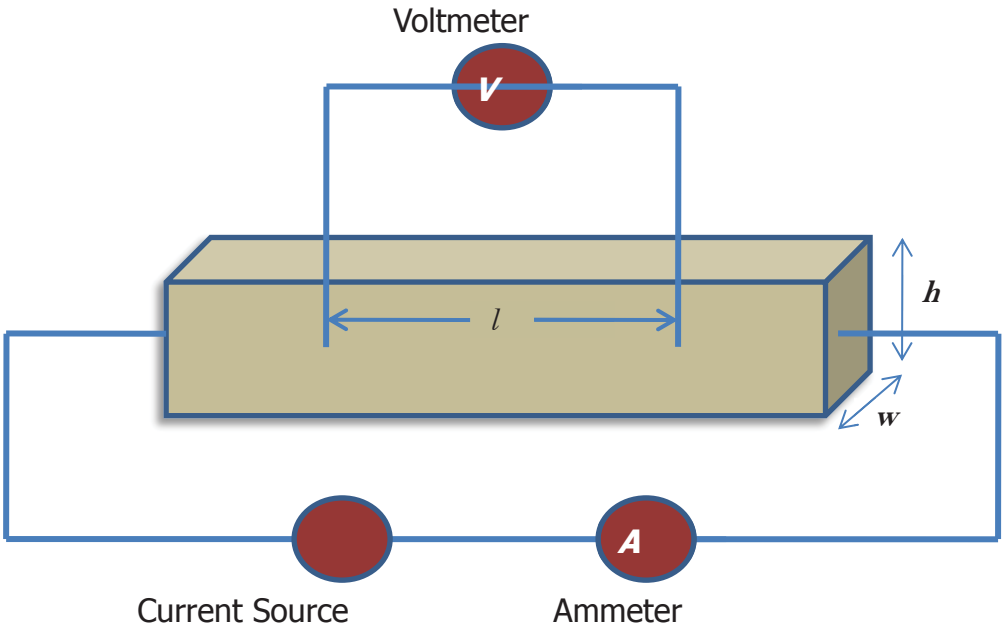

Figure 3.11. How many points? point technique used to measure the resistivity of bars.

A constant current, I, was supplied, and voltage across the two points using the platinum contacts, which were separated by distance *l*. The resistance of the samples was measured and then the conductivity of the samples was calculated according to the equation below

$$\text{Conductivity} \quad \sigma = l / (R \times w \times h) \qquad 3.3$$

The conductivity of LSM-YSZ samples was measured in air and the Ni-YSZ samples were measured in a reducing environment (hydrogen).

3.8.2 Ionic Conductivity

To measure the ionic conductivity of the YSZ samples, both sides of the YSZ disk needed to be coated with a Pt electrode. This was done by using Liquid Bright Platinum (part # 6082). It was thick dark paste which contained 66% platinum from Heraeus. Liquid Bright Platinum solution contains both solvated and granular platinum particles, the paste seemed to have lost solvent over time since it was obtained 7 years ago and hence α-terpineol was added to it increase the volume and create a homogenous mixture. When air was passed through both the anode and cathode compartment at 800^0C the resistance of YSZ dropped. It behaved as an electrochemical cell and produced a current when external voltage was applied. The ionic conductivity set up is shown in Figure 3.12.

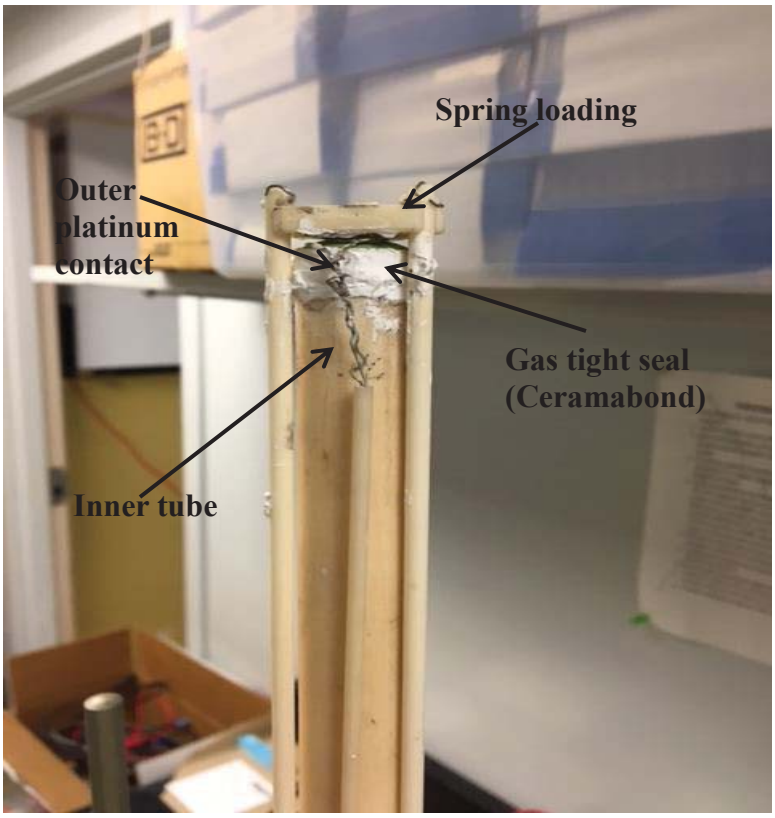

Figure 3.12 Ionic conductivity set-up using the Probostat.

3.9 PERMEABILITY

The permeability measurements were interpreted using Darcy's law. After the conductivity measurements were performed, the furnace was allowed to cool down. The permeability measurements were done at room temperature. The permeability experiment was set up as show in Figure 3.13. Argon gas was allowed to flow through a valve that could regulate pressure from 1 to 5 psi. The pressure of the flow of gas to one side of the ceramic disk was measured using manometer 1, which was connected to the gas inlet of the Probostat^{TM}. Manometer 2 was connected to the gas outlet of the Probostat^{TM} to measure the pressure drop on the opposite side of the ceramic disk. The flow rate was

measured using an inverted graduated cylinder and stop watch. The difference in pressure drop was noted.

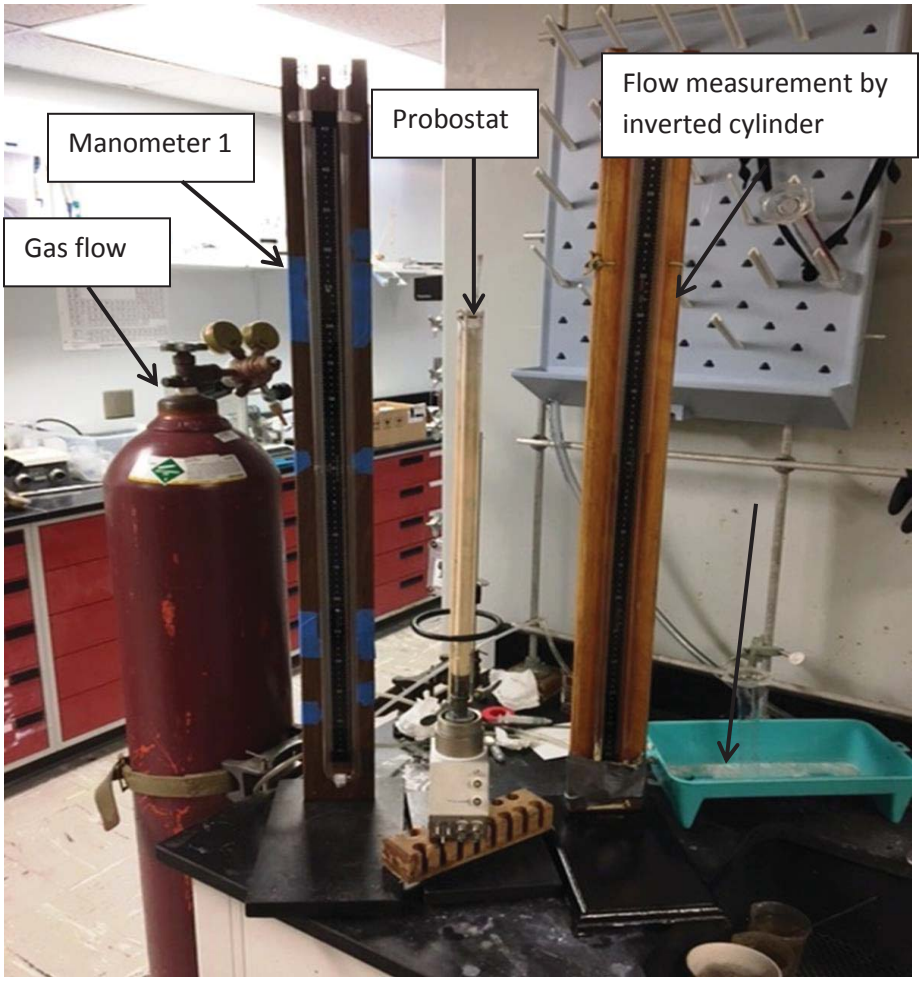

Figure 3.13. Permeability set-up

3.10 SCANNING ELECTRON MICROSCOPY (SEM)

The SEM analysis of the samples was done using a JEOL JIB 4500 multibeam(Figure 3.14) and a JEOL JST-IT 300 (Figure 3.15). The powders were loaded onto the carbon tape placed on the holder and loaded into the SEM. All samples were dried in a furnace for an hour at 120 °C to dry out the moisture. The samples for cross-section analysis had to be polished beforehand. The purpose of polishing was to remove all the damage that

was done to the surface of the sample by sawing and grinding procedures. In this stage the sample is polished by a sequence of successively fine diamond suspensions ranging from 6 μm to 0.25 μm.

Figure 3.14. Image of JEOL JIB 4500

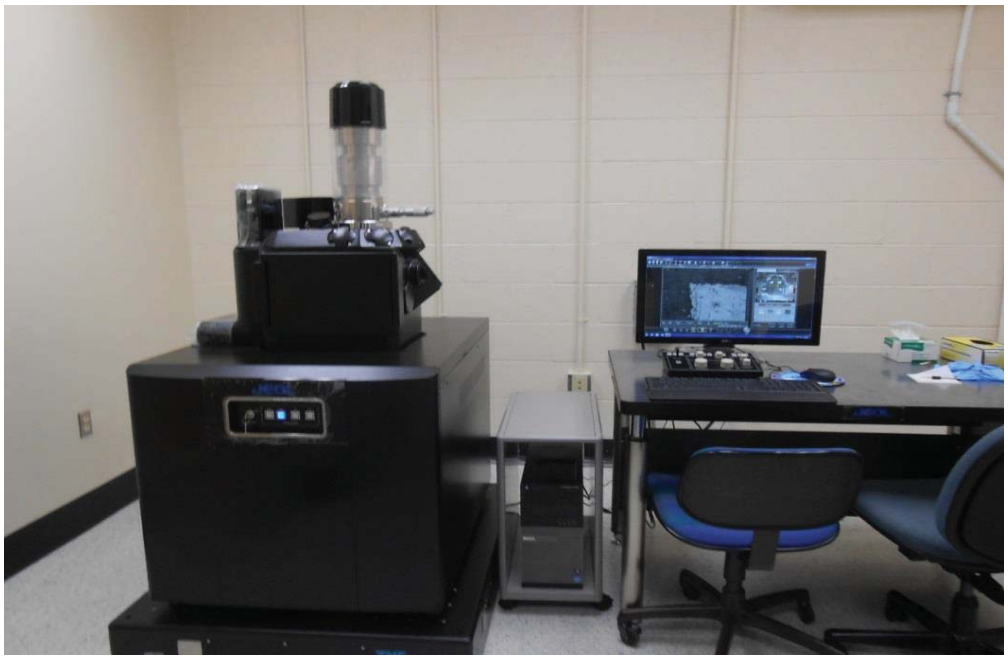

Figure3.15. Image of JEOL JSM-IT300LV variable pressure SEM

Since the resolution of optical microscopy is limited by distraction effects, higher resolution information is obtained by scanning electron microscopy. In SEM a beam of electrons is focused on the surface of the sample. When a beam of electrons is focused on the surface of solid sample it produces various signals such as backscattered, secondary and Auger electrons, X-ray fluorescence photons and other photos of different energies. In SEM only backscattered and secondary electrons are used to construct an image [6]

The electron source is usually a tungsten filament. The electron beam is focused on the object using a magnetic condenser and objective lens systems. The electrons are accelerated onto the object with energies ranging from 1 to 30 keV. The lenses are capable of reducing the spot size of the beam to nearly 10 nm as the beam hits the sample surface [6]

Scanning in an SEM system is made possible by the pair of electromagnetic coils that are located inside the objective lens; a pair is responsible for deflecting the beam in the x direction across the sample and the other is setup to deflect in the y direction. In SEM, conductive samples are easiest to analyze, as the unhindered flow of electrons reduces objects that are visualized as a result of charge buildup. Another advantage of electrically conductive samples is that they are also thermally conductive,which reduces their degradation as a result of heat. Nonconductive samples can be made conductive by coating the surface with a metallic film [6].

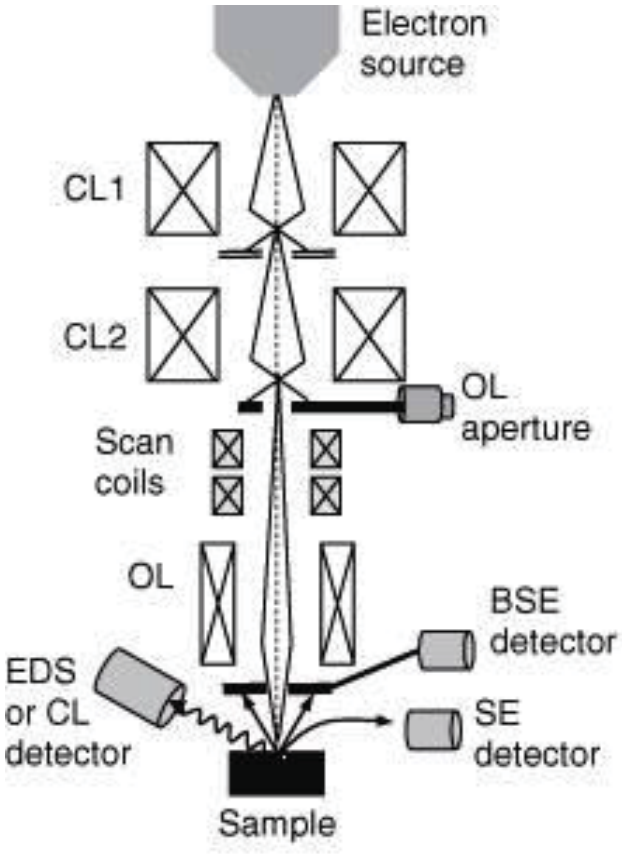

Figure3.16. Electron beam column in an SEM [7]

The secondary electrons are produced when an object is bombarded with an electron beam which has energy of several keV. These electrons have energy of about 50 eV and their numbers are usually half to one fifth of the backscattered electrons. These electrons are produced when the beam strikes the weakly bonded conduction electrons in the sample. They are only produced from depths ranging from 50 to 500 Å and their exit beam is larger than the incident beam in diameter. These can be prevented by the application of a negative bias to the transducer housing. The secondary electrons provide a more detailed image to understand the morphology of the surface of the sample [6]

When the beam of electrons strikes the surface of the object, some electrons penetrate the object and undergo elastic and non-elastic collisions. Some of the electrons remain in the object while others undergo more collisions and eventually exit from the surface as back scattered electrons. The diameter of the beam produced as a result of backscattered electrons is much larger than the incident beam. These electrons have a broad energy spread ranging from 50 eV to almost the energy of the incident beam. The backscattered electrons provide a lower resolution image of the surface than the one provided by the secondary electrons but they provide a more distinctive contrast between heavier atoms and lighter ones. The image provided by a heavier atom will be brighter. The area of origin of secondary and backscattered electrons is depicted in Figure 3.17.

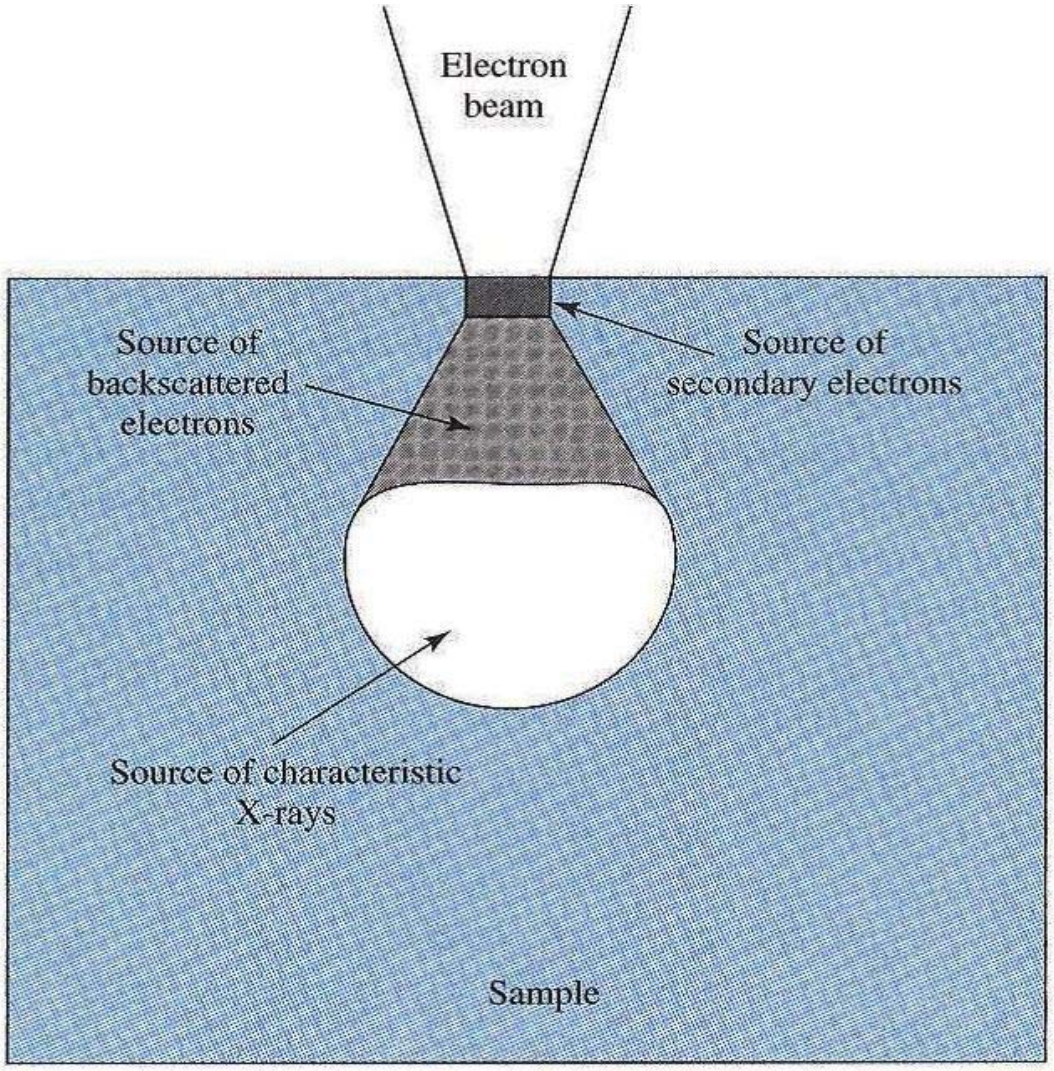

Figure 3.17. Source of backstattered and secondary electrons [6]

3.11 ENERGY DISPERSIVE SPECTROSCOPY (EDS)

The chemical composition of the samples can be studied with the help of EDS. EDS was done using the EDAX™ Apollo SDD EDS detector in the JEOL JIB-4500 multi beam system.

EDS utilizes the X-rays that are emitted when the sample is bombarded with an electron beam. It can essentially be utilized to detect all the elements ranging from Be to

U,although most instruments are not capable of detecting elements with atomic numbers less than 10 [c]. The electron beam can knock out the electrons from the K-shell which then causes the electrons from the L-shell or other higher shells to relax and fill the electrons in the K-shell. This process leads to release of energy in the form of characteristic x-rays of each element. This process is shown in figure 3.18.

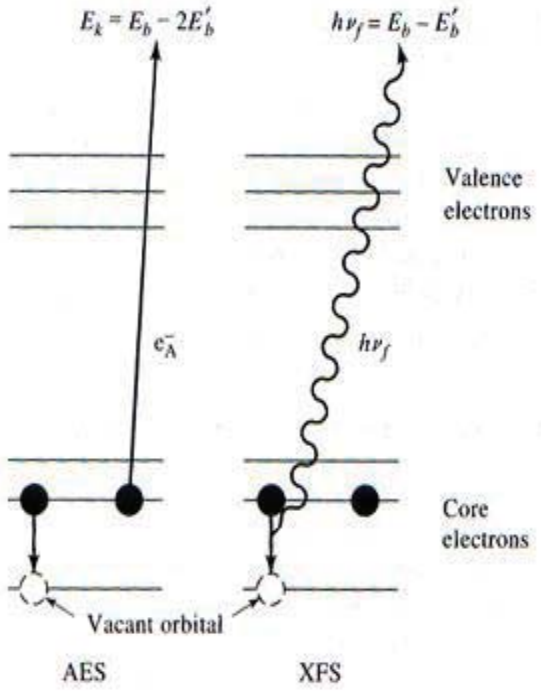

Figure 3.18. Difference between X-ray fluorescence spectroscopy and Auger electron emission during SEM analysis [8]

When analyzing for elements with atomic numbers above 35, L lines are used instead of K lines to prevent the need for extremely high electron beam energy. The EDS can be used to create an elemental map of the area scanned under an SEM. The EDS can show the percentages of the elements present in the scanned area [9]

3.12 PARTICLE SIZE ANALYZER

The Cilas 1190 particle size analyzer was used to analyze the particle size distribution of all the powders. It is equipped with 3 lasers to ensure accuracy. The instrument is capable of measuring particles ranging from 0.04 to 2,500 µm.

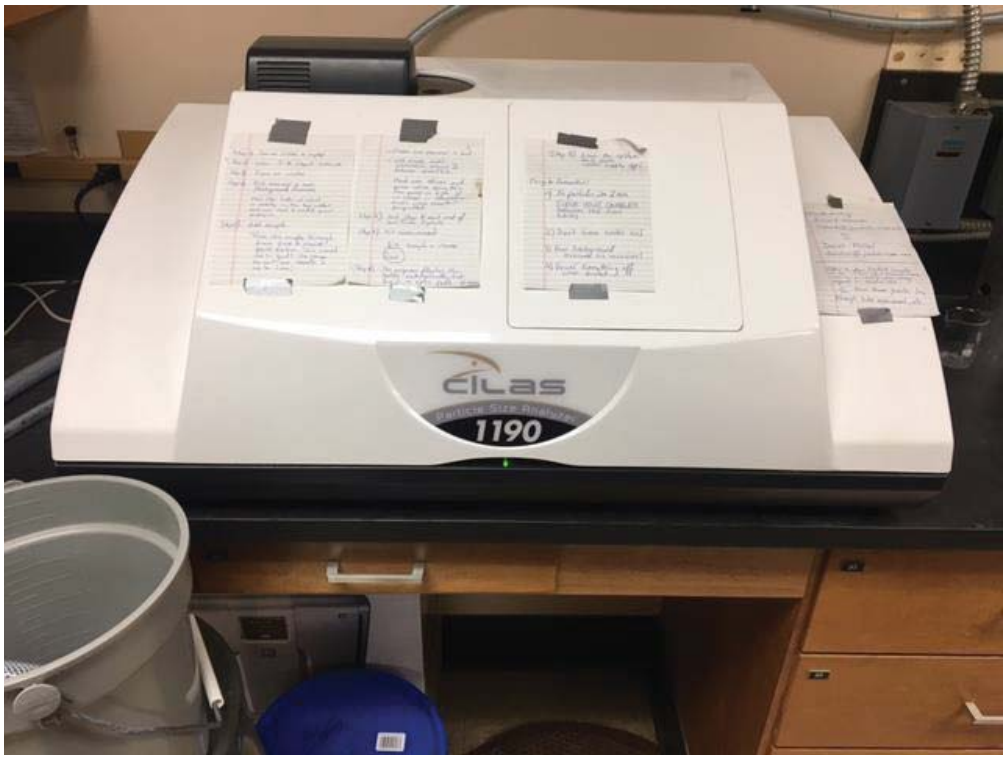

Figure3.19. Cilas 1900 laser particle size analyzer

The instrument is available in two different designs depending up on the user's desire to make measurements in either liquid or dry dispersion. The instrument at Youngstown State University is set up to measure samples in a liquid dispersion.

The particles are analyzed by laser diffraction. It is based on the fact that when light strikes a particle it some of it gets scattered. The scattering pattern is a function of the particle size of the particles in a sample. The scattering pattern obtained is the ratio of

diameter of the particles (D) and the wavelength of the incident light (λ). According to diffraction theory, the scattering angle is inversely proportional to the particle size of the sample and is calculated as [14]:

$$\text{Sin } \theta = 1.22\lambda / D \qquad 3.11$$

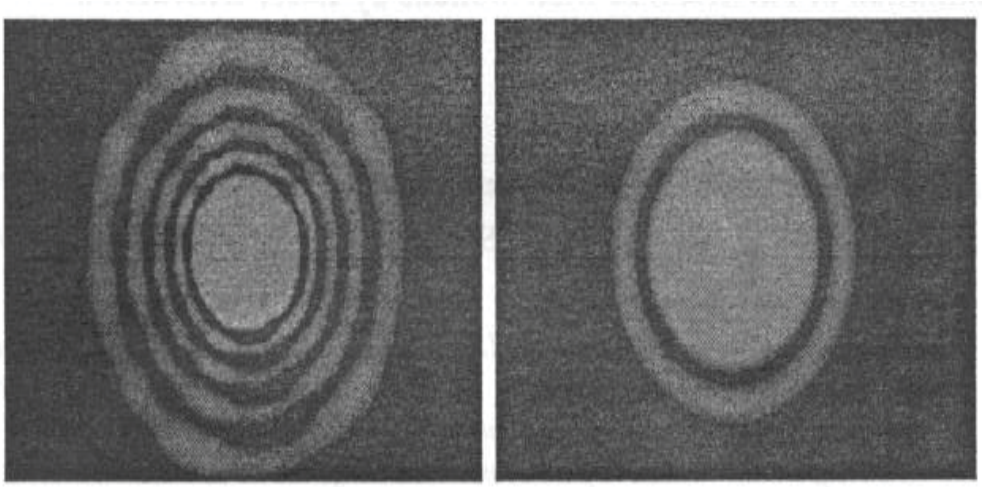

Figure3.20. Diffraction patter from a larger particle (left) and smaller particle (right) [11]

Fraunhofer, Mie and Rayleigh scattering all can be differentiated depending on (D/λ) ratio. If the particles are 5-6 times larger than the λ, then Fraunhofer scattering occurs. If the particle size is about 10 times smaller than the λ, then Rayleigh scattering occurs. If the ratio is around 1 then it can be regarded as Mie scattering. The ratio of light that is scattered from Mie and Fraunhoer is very small, whereas for Rayleigh scattering it almost

equal.

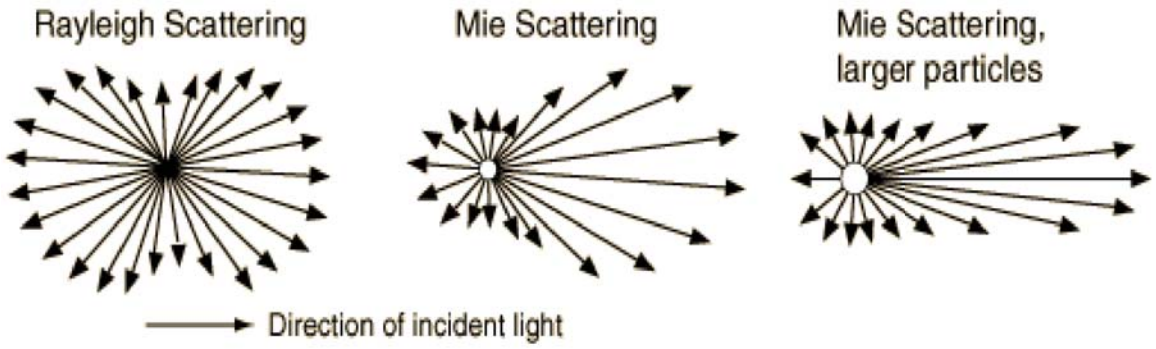

Figure 3.21. Different types of scattering based on (D/λ) [13]

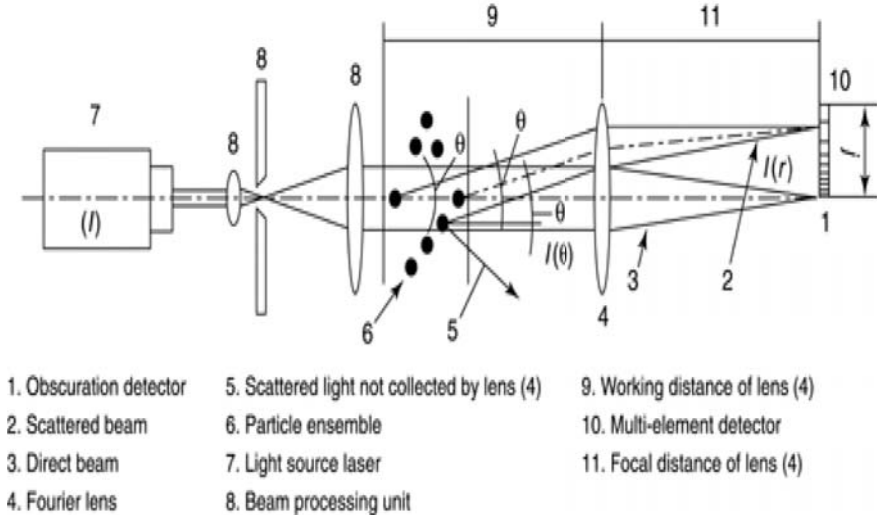

Figure 3.22. Setup of a laser diffraction instrument [12]

A dispersion solution was made by adding 0.4 g sodium hexametaphosphate to 10 ml of water. The powders were added to the solution to prevent agglomeration.

The measurements were performed by switching on the Cilas instrument and its dedicated laptop. Then the software used to perform the measurements (Size Expert Software) was launched. The water was then turned on to the instrument by turning the

lever. Once the reservoir was filled, background measurements were performed. The stirrer and pump were turned on before the liquid powder dispersion samples were added to the reservoir until the obscuration (Obscuration is the measure of percentage of light that gets blocked by the sample) showed a reading between 10 to 20%.The real time signals window was closed and measurements were made. The instrument flushed out the system automatically. The procedure was repeated for all the samples.

CHAPTER 3

REFERENCES

1) Retrieved on December 15th 2009, from http://flacktek.net/dac150.1fvzk.php
2) Retrieved on December 16th 2013, http://www.hyrel3d.com/resources/forum/engine-hr/
3) Hyrel System 30 3D Printer MANUAL Revision 1.3; Hyrel 3D: Norcoss, GA, 2016
4) US Fuel Cell Council, Introduction to Solid Oxide Fuel Cell Button Cell Testing , July 6 , 2007
5) Retrieved on December 20th 2009, from http://www.norecs.com/index.php?page=141
6) Skoog, D. A., Holler, F. J., & Crouch, S. R. (2007). Principles of Instrumentation (6th ed.). Belmont, CA: Thomson Brooks/Cole.
7) Bell, D. C., & Erdman, N. (2013). Low Voltage Electron Microscopy: Principles and Applications. West Sussex, UK: John Wiley & Sons.
8) Skoog, D. A., Holler, F. J., & Nieman, T. A. (1998). Principles of Instrumentation Analysis (5th ed.). Philadelphia, PA: Saunders College Publishing.
9) http://cfamm.ucr.edu/documents/eds-intro.pdf
10) Rahaman, M. N. Ceramic processing; CRC/Taylor & Francis: Boca Raton, FL, 2007
11) TECHNICS-NEW MATERIALS 21 (2012) Determination of particle size distributions by laser diffraction, ZORAN STOJANOVIC, INSTITUTE OF

TECHNICAL SCIENCES OF SASA, BELGRADE, SMILJA MARKOVIC INSTITIUTE OF TECHNICAL SCIENCES OF SASA, BELGRADE

12) Retrieved on October 29th 2016, from :http://www.pharmacopeia.cn/v29240/usp29nf24s0_c429.html

13) Retrieved on October 29th 2016, from :http://hyperphysics.phy-astr.gsu.edu/hbase/atmos/blusky.html

CHAPTER 4

RESULTS AND DISCUSSION

4.1 PARTICLE SIZE AND MORPHOLOGICAL ANALYSIS OF POWDERS

4.1.1 Particle Size and Morphological Analysis of YSZ powder

The particle size distribution of the YSZ powder obtained from the laser scattering technique is shown in Figure 4.1. The mean diameter of the particles in the YSZ powder was 0.64 µm. The data shows that the particles in the powder had a wide a range of particle size but 80% of the particles ranged from 0.099 µm to 0.894 µm.

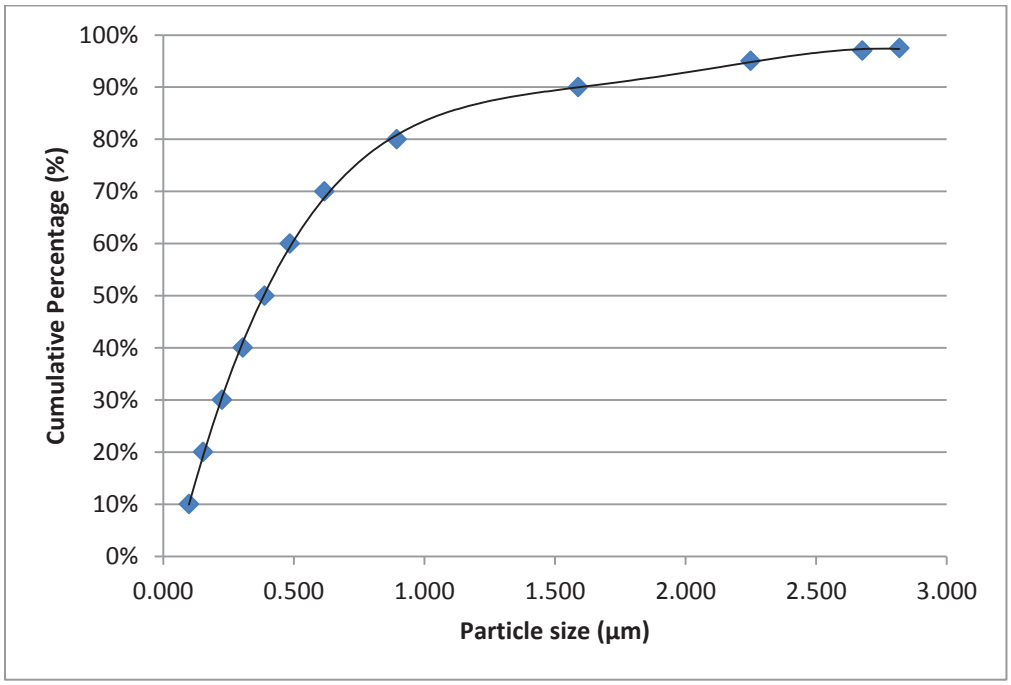

Figure 4.1 Particle size distribution of YSZ powder

The morphology of YSZ powder was analyzed under an SEM. The images obtained are presented in Figure 4.2. The SEM images support the data obtained from the laser

scattering process in that the particles present in the powder exhibit a range of particle sizes, from tenths to single microns. The particles also did not have any predominant shape and the presence of agglomerations can also be seen in Figure 4.2.

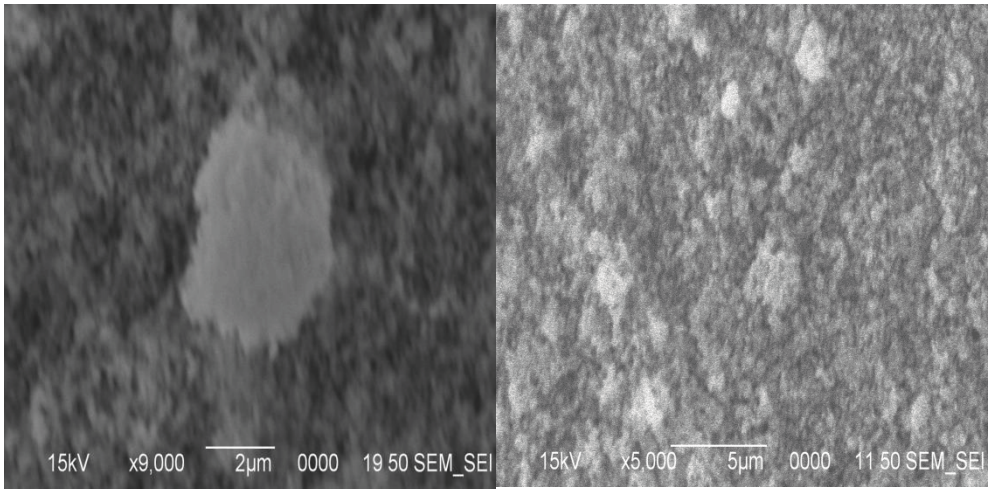

Figure 4.2 Morphology of YSZ powder at 9K and 5K magnification

Powders with nanosize particles are not recommended from the fabrication of YSZ electrolyte as YSZ nanoparticles have a high tendency to spontaneously agglomerate in order to reduce the interfacial energy and the total surface area. The presence of agglomeration will result in the formation of large pores in the sintered ceramic layer [6]. Dahl et al., 2007 performed several experiments and concluded that densities of greater than 96% were obtained from YSZ powders with particle sizes with mean diameters of 210 and 370 nm, regardless of the technique of fabrication [1].

4.1.2 Particle Size and Morphological Analysis of LSM powder

The particle size distribution of the LSM powder obtained from the laser scattering technique is shown in Figure 4.3. The mean diameter of the particles in the LSM Powder

was 2.01 µm. The data shows that the particles in the powder were of a wide a range of particle sizes.

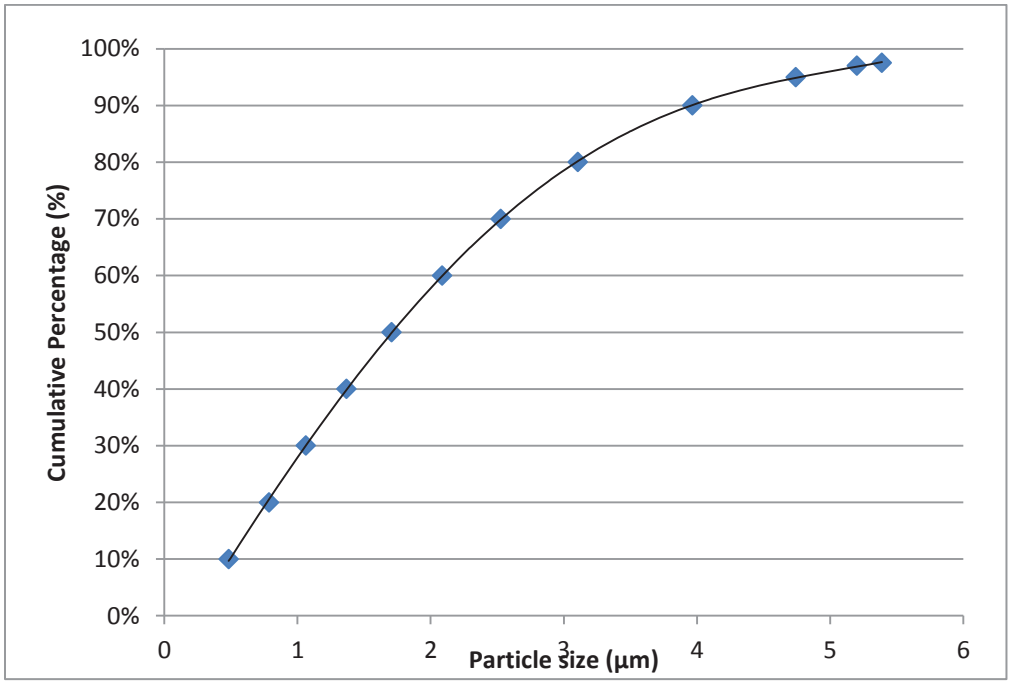

Figure 4.3 Particle size distribution of LSM powder

The morphology of LSM powder was also analyzed under an SEM. The images obtained are presented in Figure 4.4. The SEM images support the data obtained from the laser scattering process that the particles present in the powder have particle sizes in the range from 0.48 µm to 5.83 µm. The particles also did not have any predominant shape but they particles had very sharp well defined edges unlike those seen in YSZ powder which were globular. On comparison with particles present in YSZ powder, the LSM particles were bigger in size as 80% of them ranged between 0.48 µm to 3.1 µm. The range was also broader when compared to YSZ powder.

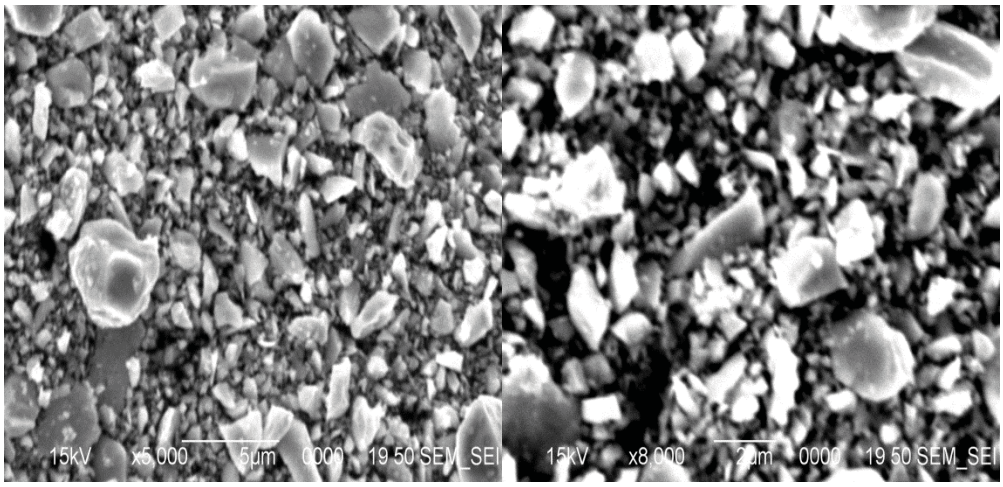

Figure 4.4 Morphology of LSM powder at 5,000 and 8,000 magnifications

4.1.3 Particle Size and Morphological Analysis of Ni-YSZ powder

The particle size distribution of the Ni-YSZ powder obtained from laser scattering technique is shown in Figure 4.5. The mean diameter of the particles in the Ni-YSZ powder was 6.15 µm. The data shows that the particles in the powder ranged from 0.24 µm to 20.4 µm. The Ni-YSZ powder had particles which were much coarser compared to the particles in LSM-YSZ (50-50) and YSZ powders. In Ni-YSZ powder, 40% of the particles had sizes between 2.45 µm and 11.526 µm.

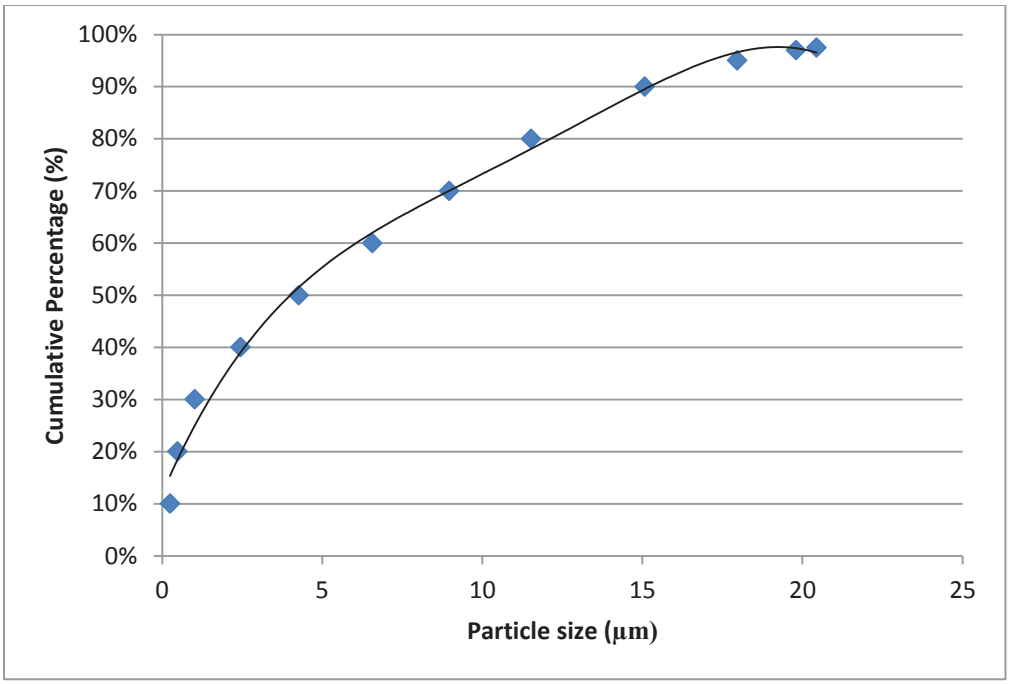

Figure 4.5 Particle size distribution of Ni-YSZ powder

The morphology of Ni-YSZ powder was also analyzed under an SEM. The images obtained are presented in Figure 4.6. The SEM images support the data obtained from the laser scattering process in that the particles present in the powder have different particle sizes. The particles also did not have any predominant shape but the powder consisted of two different types of particles as seen in Figure 4.6. Particle type 1 as seen in the images had very distinct and defined edges and appears to have a smooth surface, whereas Particle type 2 looked like a cluster of smaller particles.

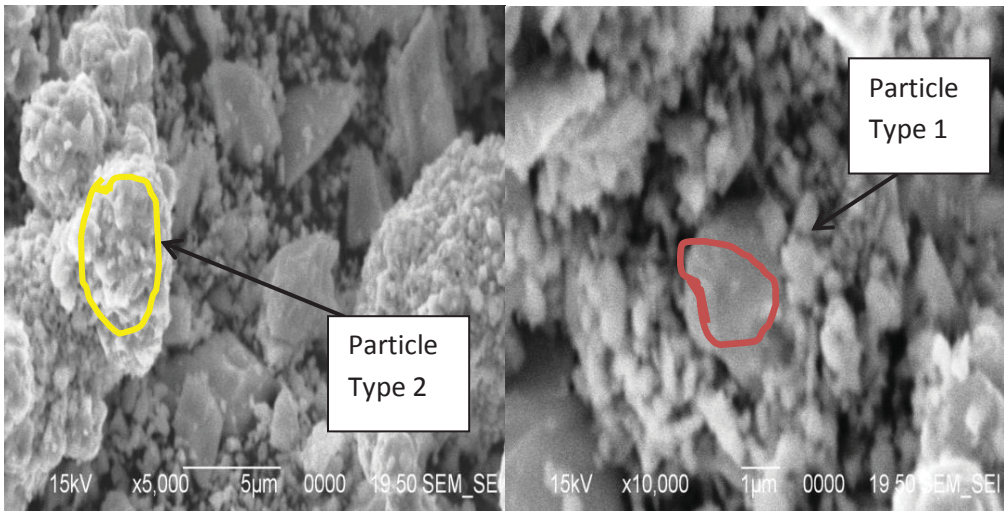

Figure 4.6 Morphology of Ni-YSZ powder at 5000 and 10, 000 magnifications

The two different types of particles illustrated in Figure 4.5 were examined using an EDAX (energy dispersive spectroscopy) instrument to study their elemental composition. The area highlighted in Figure 4.7 corresponds to Particle type 2.

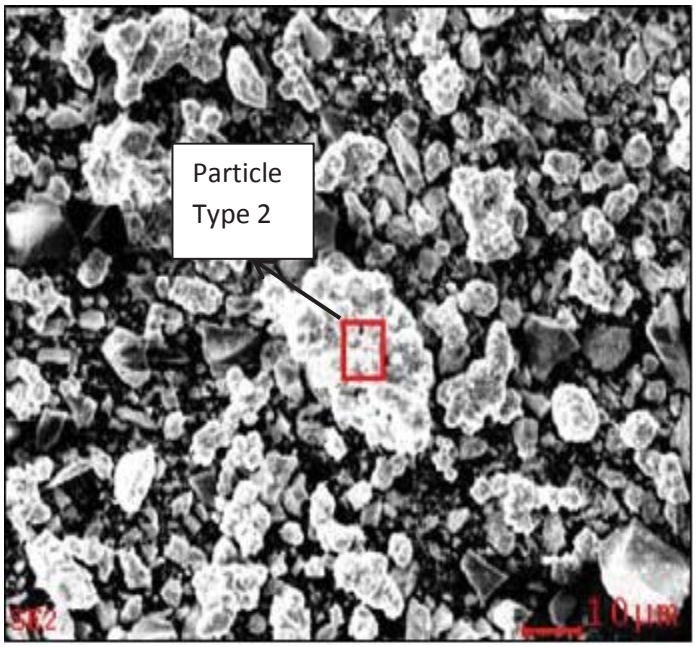

Figure 4.7 EDS analysis of Ni-YSZ powder corresponding to Particle type 2

The elemental composition corresponding to Particle type 2 is presented in Table 4.1 and shows the presence of all the elements present in Ni-YSZ.

Table 4.1 EDS elemental composition corresponding to the area highlighted in Figure 4.7

Element plus Transition	Wt%	At%
OK	19.49	48.97
NiL	67.67	46.33
YbM	04.64	01.08
ZrL	08.20	03.61
Matrix	Correction	ZAF

The Kα emission line for Zr is at 15.77 KeV and for Y it is at 14.96 KeV, which causes a considerable overlap in their peaks and hence they cannot be resolved [2]. Yb's presence in the sample can be regarded as an impurity.

The area marked in Figure 4.8 corresponds to Particle type 1 present in the Ni-YSZ powder.

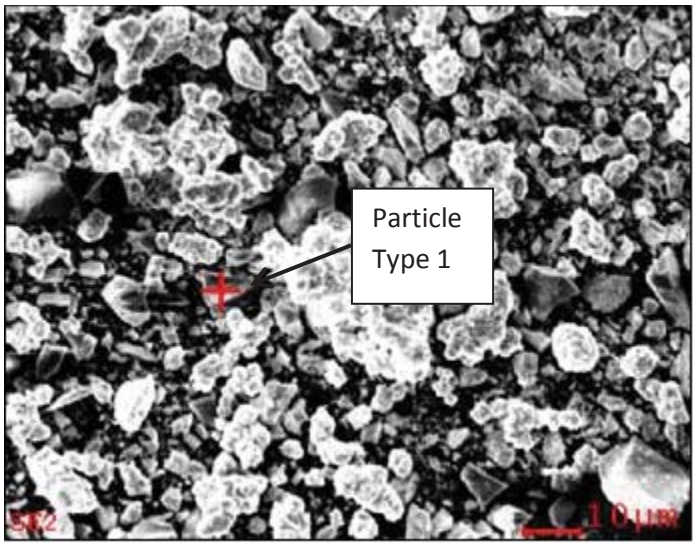

Figure 4.8 EDS elemental analysis of Ni-YSZ powder corresponding to Particle type 1.

The elemental composition corresponding to Particle type 1 is presented in Table 4.2. It also showed the presence of all the elements present in Ni-YSZ. Based on vendor specifications, the powder nominally contains 40% Ni and 60% YSZ. Particle type 1 showed a lower concentration of Ni than particle type 2. The concentration of Zr was higher in particle 1 and as mentioned before Y and Zr peaks could not be resolved into separate peaks. Other particles were analyzed and similar compositions were obtained. This technique could not be used successfully to validate the difference between particles of different elements, this may be due to the fact that the beam could not be focused on only a single micron-sized particle and could have detected the emitted x-rays from particles in the vicinity of the area analyzed.

Table 4.2 EDS elemental composition corresponding to the area highlighted for Figure 4.8

Element plus transition	Wt%	At%
OK	18.94	50.76
NiL	44.63	32.60
YbM	02.21	0.55
ZrL	34.22	16.09
Matrix	Correction	ZAF

4.1.4 Particle Size and Morphological Analysis of NiO nanopowder

The particle size distribution for the NiO nanopowder purchased from Sigma- Aldrich was deduced using the laser scattering technique and is presented in Figure 4.5. The mean diameter of the particles in the NiO powder was 0.61 μm. The particles had a much narrow range of particle size compared to the other powders. The particles were of sizes between 0.432 μm and 0.918 μm.

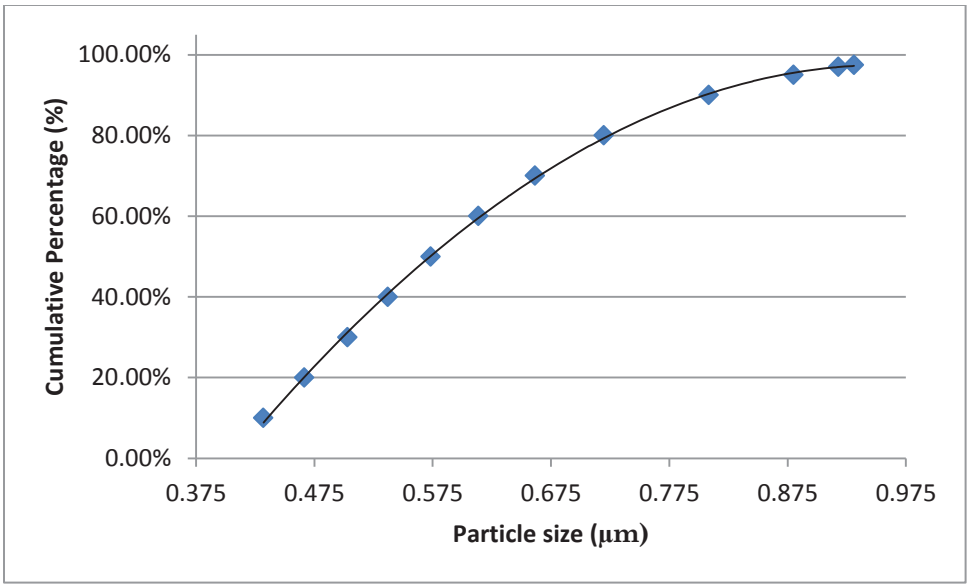

Figure 4.9 Particle size distribution of NiO nanopowder

The SEM images for the NiO powder obtained from Sigma Aldrich are displayed in Figure 4.10. The supplier stated that the particle size of the powder was < 50 nm but as seen in the images in Figure 4.10 and supported by the data obtained from the particle size analyzer it is clear that the particles had very high agglomeration. Nanoparticles have very high surface energy, making the system very unstable, so the particles have a tendency to agglomerate in order to reduce this energy and attain a more stable state [3].

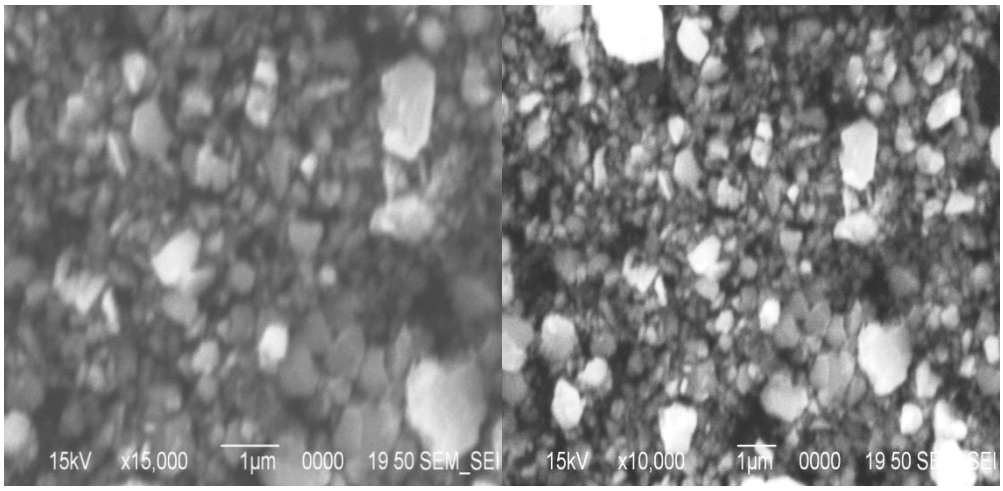

Figure 4.10. SEM images of NiO powder at 15k and 10k magnification.

4.2 INITIAL DATA

4.2.1. Cube

One of the very first prints fabricated using the Hyrel 3d printer is displayed in Figure 4.11. The paste formulation used to print this sample contained water as a solvent and 3% methoxy cellulose as binder. The edges lacked definition because of the adhesion between water molecules and the large surface area of the nozzle dragged the paste. As discussed in chapter 2, water increases the viscosity of the paste.

Figure 4.11. 3d-printed YSZ cube using water as the solvent and 3% methoxy cellulose as the binder.

Theoretical density of YSZ is 6.10 g/cm^3. The mass of the 3d printed sample was 2.8636 g and the volume displaced by it was 476 mL. Therefore, the density calculated for the sample was 6.06 g/cm^3, or 98.6%. This was very encouraging. The porosity data agreed with the SEM analysis (Figures 4.12 and 4.13) as the sample appeared to be very dense with very small pores.

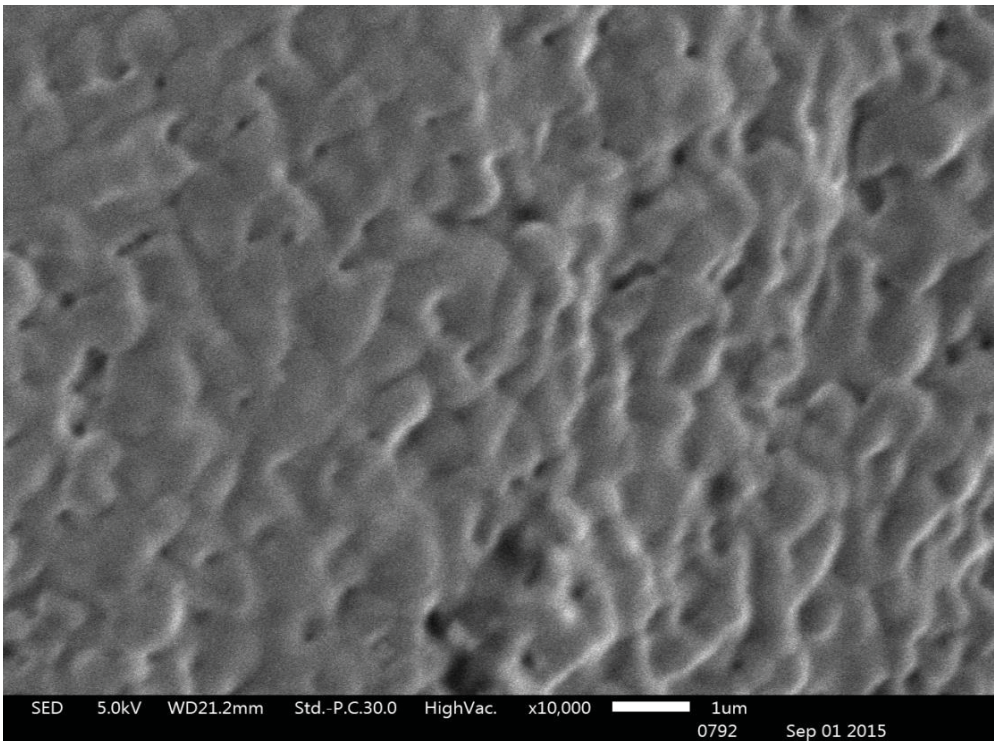

Figure 4.12. SEM image of 3d-printedYSZ at 10k magnification.

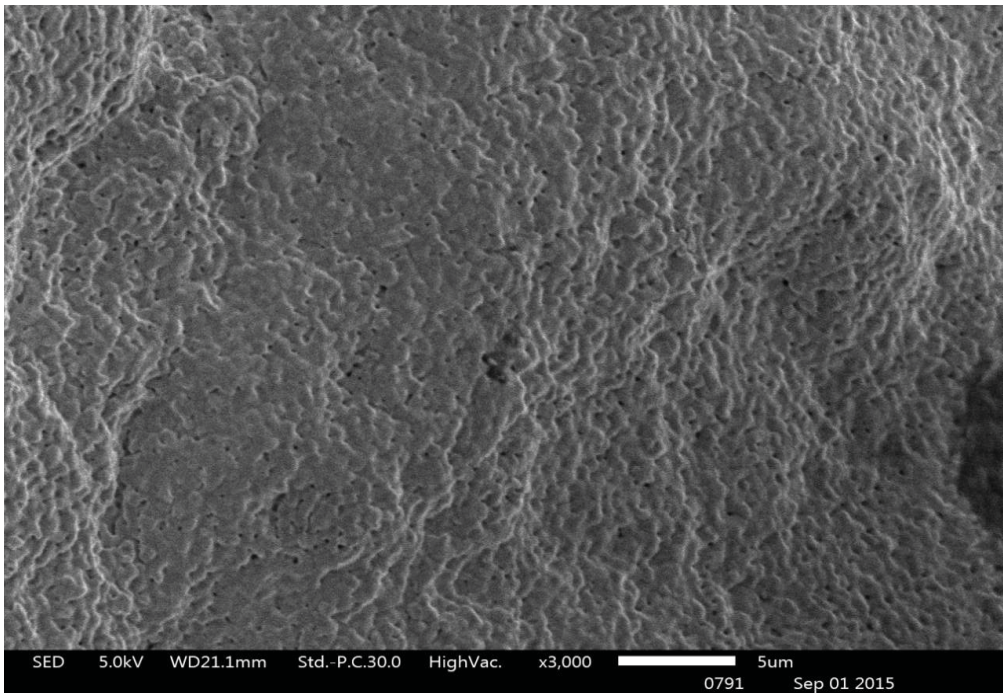

Figure 4.13. SEM image of 3d-printedYSZ at 3k magnification.

4.2.2. Circular Disk

Using the formulation with water as the solvent and 3% methoxy cellulose as the binder, a circular disk of 400 μm was attempted. The disk formed several cracks as seen in Figure 4.14 due to lack of homogeneity, which resulted in constrained sintering, which was discussed earlier in Chapter 2. If the sample has varying densities throughout the sample, it leads to the formation of stresses which lead to the creation of cracks on sintering.

Figure 4.14. 3d-printed YSZ disk with cracks due to constrained sintering using water as the solvent and 3% methoxy cellulose as the binder.

SEM images that were obtained are presented in Figures 4.15 and 4.16, which show the cracks but the sample again did not seem to have a lot of pores present in it.

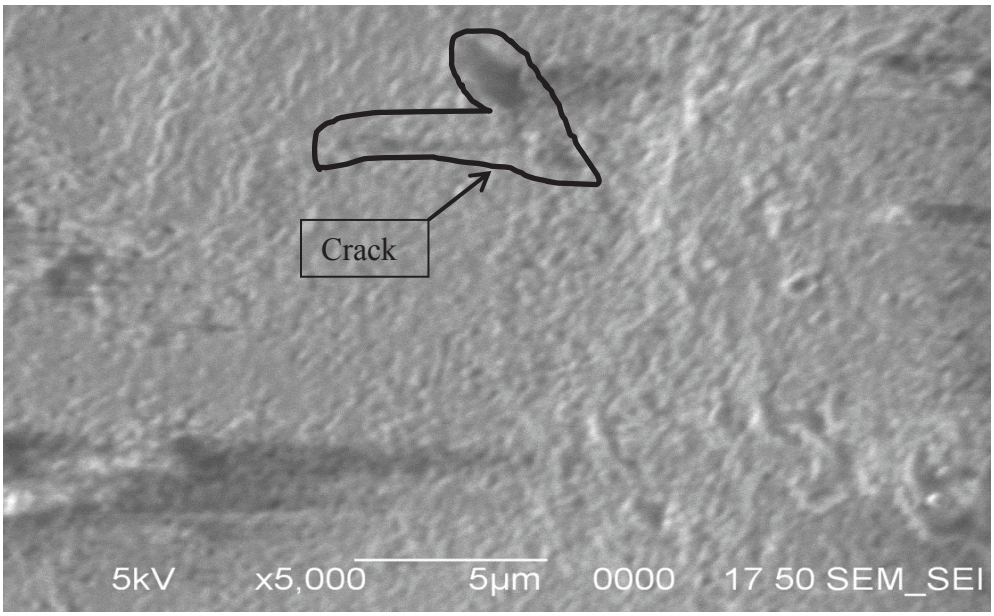

Figure 4.15. SEM image of the same cracked YSZ disk as in Figure 4.14 at 5k magnification.

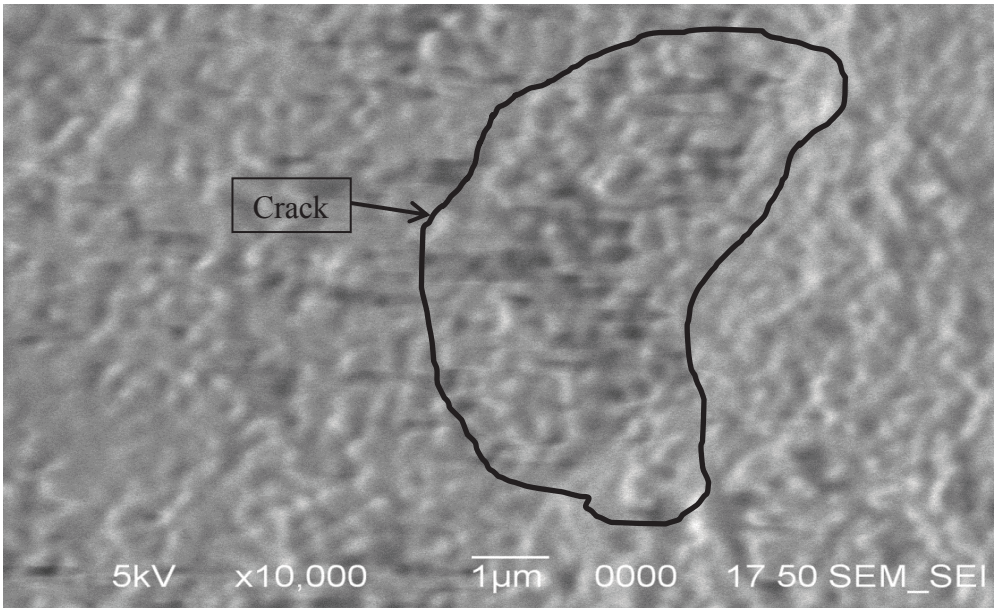

Figure 4.16. SEM image of same YSZ sample as in Figure 4.15 at 10k magnification.

4.2.3. Square Wafer

A square wafer was also printed of length and breadth 10 mm and height 3.45 mm, which is presented in Figure 4.17 below.

Figure 4.17. YSZ square wafer printed with paste containing 3% methyl cellulose as the binder and water as the solvent

The mass of the sample was obtained as 0.6272 g. It displaced a volume of 0.11 mL via the Archimedes technique. The calculated density was 5.7 g/cm^3

The density of the sintered square wafer was found to be 93.5% of the theoretical maximum. Again the sample had high density, which has been difficult to obtain using other 3d printing techniques for ceramics.

4.3. Porosity data of YSZ

4.3.1. Effect of binder on porosity of YSZ

The initial data was collected and paste formulations were prepared using water as the solvent but as discussed in chapter 2 and evident from Figures 4.11, 4.14 and 4.17; water resulted in higher viscosity and adhesion. Hence, it was replaced by cyclohexanone which proved to be a better homogenizer and printed samples had sharper edges.

The effect of binder content on porosity is shown in Figure 4.18. The porosity of the samples was measured keeping the cyclohexanone solvent constant at 5.5 g. Despite the general linear appearance of the graph, samples at both ends of the curve gave questionable porosity values due to cracking. The sample with only one percent binder had very low viscosity and the binder content was barely enough to hold the sample together in the green state. The excess solvent caused a nonuniform distribution of binder, resulting in higher density particle packing in the upper region of the printed line and low density below where the binder would congregate. This led the sample to have areas of high and low density, which resulted in the formation of cracks. The sample prepared with 9% binder content caused the paste to have very high viscosity and limited particle-particle contact, so that sintering could only commence as the binder burned out from the outer edges inwards. This leads to stresses caused by nonuniform sintering and ultimate cracking. When the samples were printed with binder content within the 2-8% acceptable range, the addition of binder increased the overall porosity of the sample.

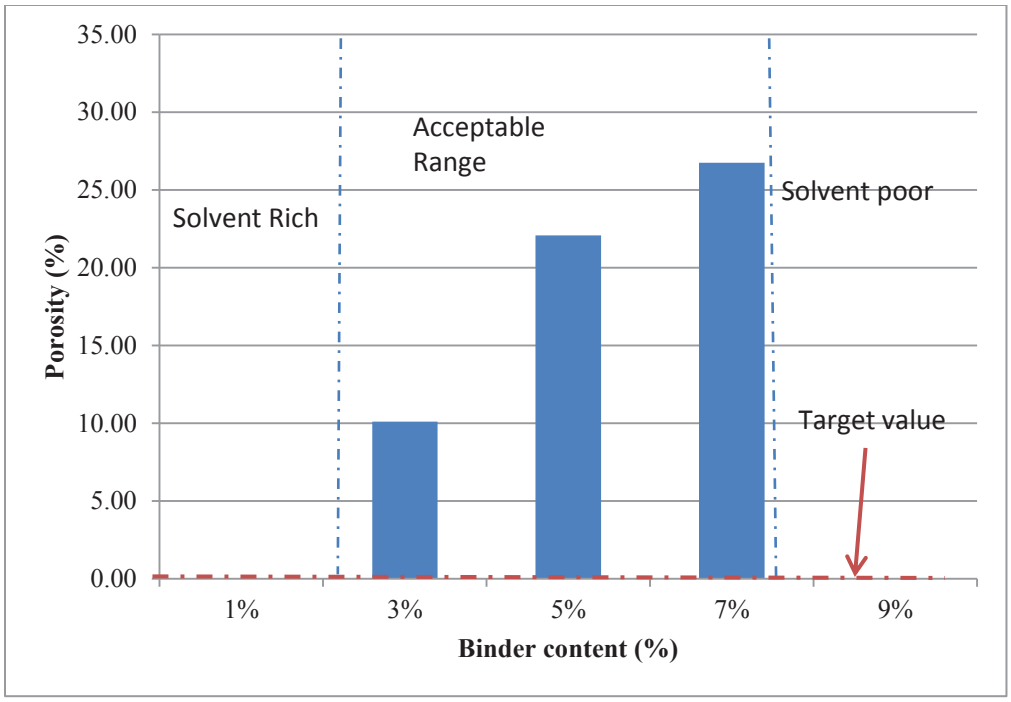

Figure 4.18 Effect of printing paste binder content on porosity of 3d-printed YSZ sintered at 1400 °C. Solvent was held constant at 5.5 g.

The results were in agreement with data in the literature which was discussed in chapter 2.

4.3.2. Effect of solvent on porosity of YSZ

In Figure 4.19 the porosity of the samples was measured when the binder content was held at a constant 3% and the solvent content was varied from 4 g to 6.5 g. Even within this rather narrow range, porosity measurements were again compromised at either end. Samples with 4 and 4.5 g solvent were solvent poor, which made for ineffective utilization of the polymeric binder. The sample with 6.5 g was solvent rich, which causes nonuniform distribution of binder. These samples after firing had numerous cracks. Only the solvent levels at 5.0 and 5.5 g gave crack-free porosity readings. This is consistent

with Figure 4.18 in terms of a workable solvent/binder ratio. Based on the crack-free data points, porosity was seen to decrease with increasing solvent content, from 12 to 8%. As discussed in chapter 2 the solvent is added to dissolve the binder and increase the flowability of the sample. The acceptable range of viscosity is very narrow, on order of one to two million centipoise, and to account for it the 3d printer has to be capable of varying the pressure of extrusion. The motor on the Hyrel 3d printer could only supply 10 pound-inches of torque which was considerably low and made it very difficult to dispense a continuous bead.

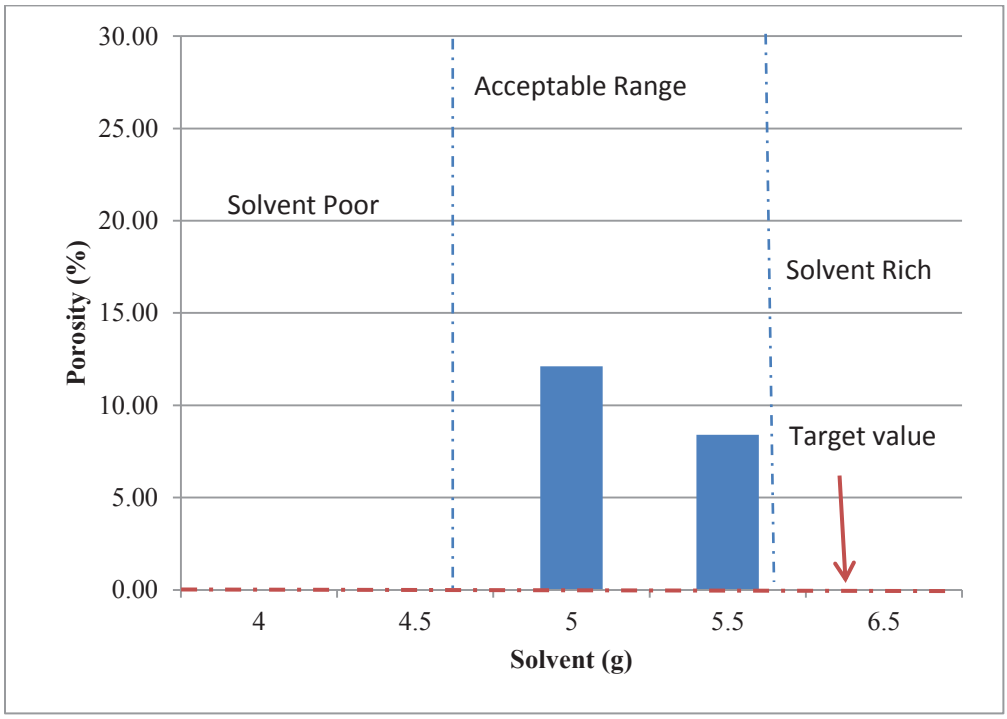

Figure 4.19. Effect of solvent content of the printing paste on porosity of 3d-printed YSZ. Sintering temperature = 1400 ^{o}C; binder content held constant at 3%.

The porosity of the YSZ samples would be expected to decrease by the addition of solvent, as the particles are better able to reposition themselves. Positioning of the

particles becomes difficult as the solvent escapes, but terpineol was added to the system, which allowed some movement of the particles as discussed in chapter 2.

4.4. SHRINKAGE DATA OF YSZ

4.4.1. Effect of binder on shrinkage of YSZ

With the idea of cofiring adjacent fuel cell components, the effect of shrinkage was studied. Figure 4.20 displays the effect of addition of binder on shrinkage of YSZ. The solvent was held constant at 5.5 g and binder content was varied from 1% to 9%. The printed samples were sintered at 1400 °C using a heating rate of 3 °C per minute. The effect of binder content is evident from the graph and agrees with theory, which suggests that shrinkage increases as the amount of binder is increased. The shrinkage data shows an almost a linear dependency on the binder content; shrinkage is a dimensional change and is not affected by imperfections or cracking In general, degree of shrinkage increases with increasing binder content, .

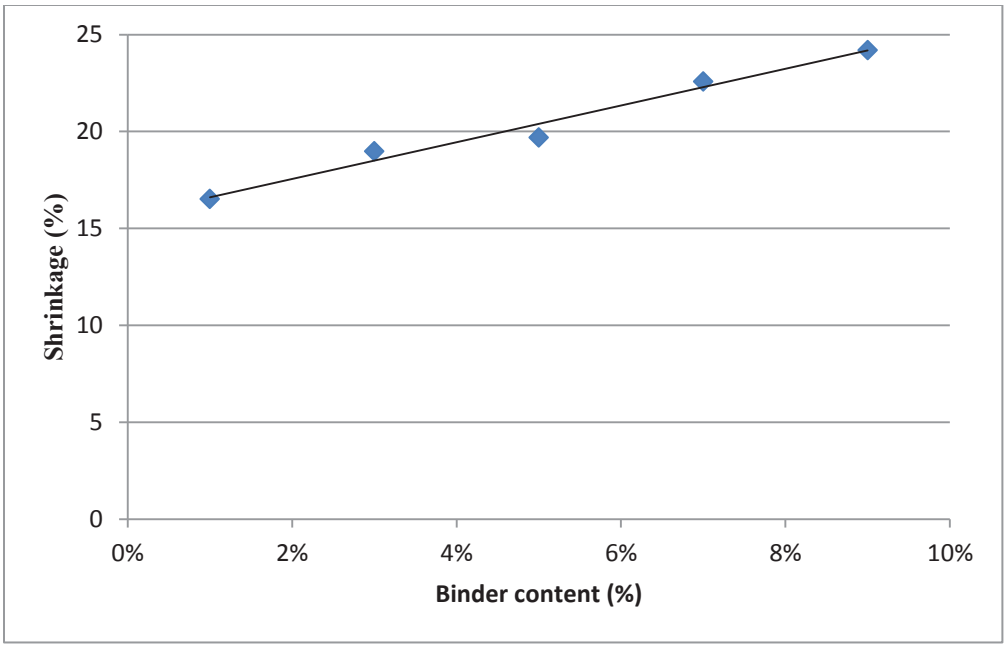

Figure 4.20. YSZ shrinkage vs binder content of the printing paste. Sintering temperature = 1400 ^{o}C; solvent content = 5.5 g.

4.4.2. Effect of solvent on shrinkage of YSZ

The effect of solvent was also correlated with shrinkage and can be seen in Figure 4.21. The binder was kept constant at 3% and the solvent was varied from 4 to 6.5 g. The printed samples were sintered at 1400 °C using a ramp rate of 3 °C per minute. Shrinkage could be varied from 19 to 26%, depending on solvent content. As seen in Figure 4.21, somewhat surprisingly, the amount of shrinkage increased with the increase of solvent content. This may be due to lower density of the binder at higher solvent levels, or there could have been some residual solvent in the green form.

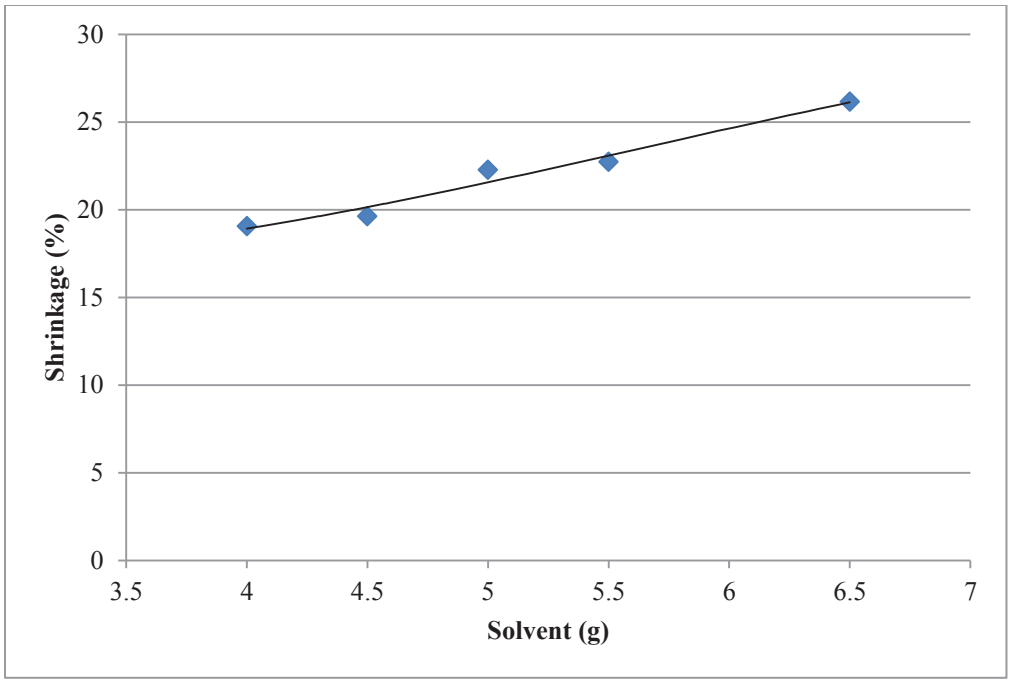

Figure 4.21. Shrinkage vs solvent content of the printing paste for 3d-printed YSZ. Sintering temperature = 1400 ^{o}C; binder content held at 3%.

4.5. IONIC CONDUCTIVITY OF YSZ

4.5.1. Effect of solvent on conductivity of YSZ

The effect of solvent content of YSZ paste formulation relative to the conductivity of a sample is presented in Figure 4.22. Again the binder content was held at 3% and solvent content was varied from 4 to 6.5 g. There was a difference of 22% in the conductivity between the least and the most conductive sample. The ionic conductivity of a sample is the result of ionic diffusion, which takes place because of vacancies or holes present in the crystal lattice. The vacancy concentration is unaffected by the sintering mechanism of YSZ and hence the activation energy required for ionic conductivity remains same. However, the "connectivity," or the ability of oxide ions to access and cross the sintered

boundaries between adjacent particles, is affected by porosity. According to theory, ionic conductivity is reduced with increase in porosity, and the data that was obtained by us agrees with it as the samples with the highest conductivities also had the least porosities. Referring back to Figure 4.19, it was shown that YSZ porosity increased with decrease in solvent content of the paste. Thus the trend in Figure 4.22, where conductivity rises with solvent content of the paste, is consistent with theory and the previous results. The paste containing 5.5 g solvent and 5% binder had a conductivity of 1.9 S/cm, within 5% of the value found in conventionally prepared YSZ electrolytes. . Literature values have been reported to be around 2 S/m at 800 °C [4].

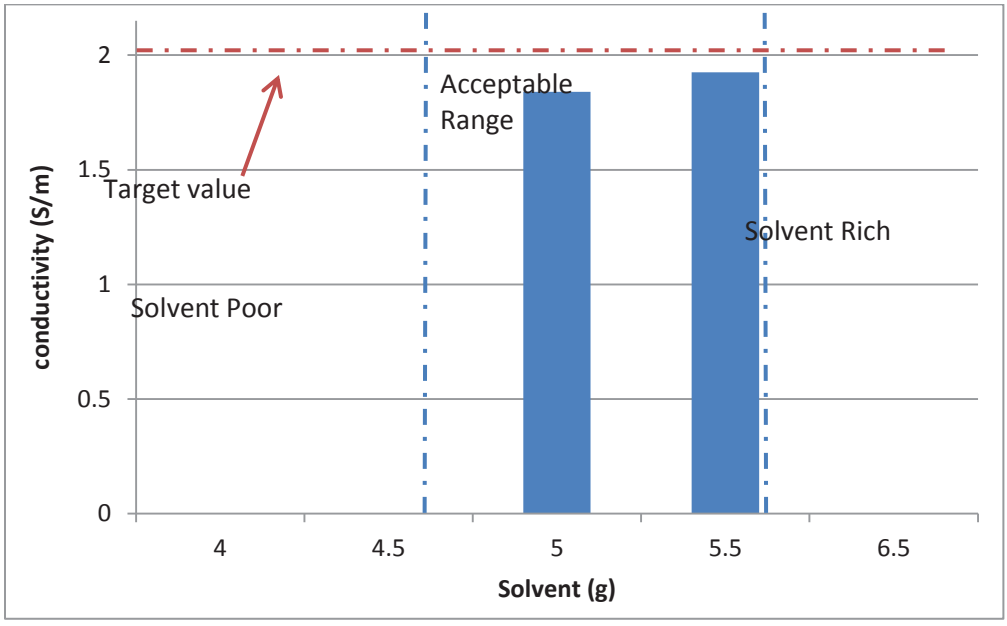

Figure 4.22. Ionic conductivity of 3d-printed YSZ vs solvent content. Sintering temperature = 1400 ^{o}C; binder content held constant at 3%.

4.5.2. Effect of Binder on conductivity of YSZ

The effect of binder content on the conductivity of 3d-printed YSZ is plotted in Figure 4.23. The solvent was held constant at 5.5 g and the binder content was varied from 1 to 9%. There was a difference of 24% between the least and the most conductive samples. This is once again interpreted as a porosity effect. Referring back to Figure 4.18, increasing binder content increased porosity, which has a detrimental effect on conductivity. The sample with 3% binder had the least porosity and showed the highest conductivity. If the conducting species are adsorbed onto pore surfaces in that case the ionic conductivity will increase, but only if the pores are open ended.

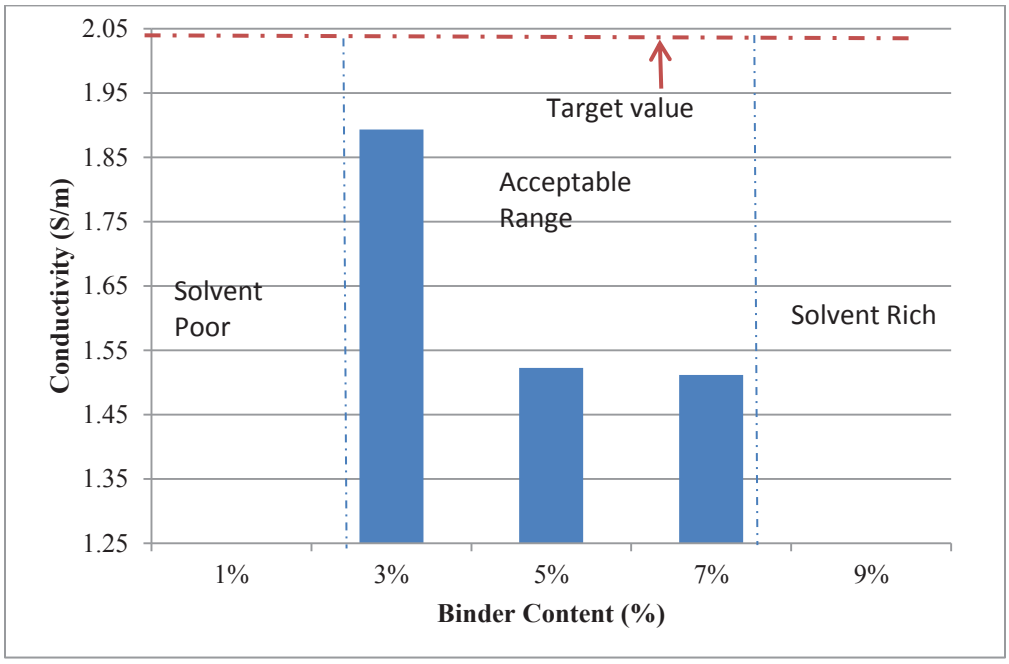

Figure 4.23 Conductivity of printed YSZ disk vs binder content of the paste. Sintering temperature = 1400 ^{o}C; solvent content hold at 5.5 g.

4.6. PERMEABILITY DATA OF YSZ

4.6.1. Effect of Binder content on permeability of YSZ

Another important parameter is permeability, which was calculated using Darcy's law. This was one of the most difficult measurements to make as some samples can have cracks due to constrained sintering that make for an artificially high permeability reading. The samples with 1% and 9% binder were extremely difficult to print, and exhibited some cracks after sintering due to irregular stresses. As a result, permeabilities for the high and low binder contents were 2 to 4 times higher than the trendline would indicate. Analyzing the other data points in the graph shown in Figure 4.24, leads to the conclusion that the permeability of a sample increases as the amount of binder is increased. When the binder escapes the ceramic body, it creates channels that result in either closed or open porosity. Although higher porosity should increase the probability of higher permeability, if the majority of the pores are closed, the permeability of the sample will be low.

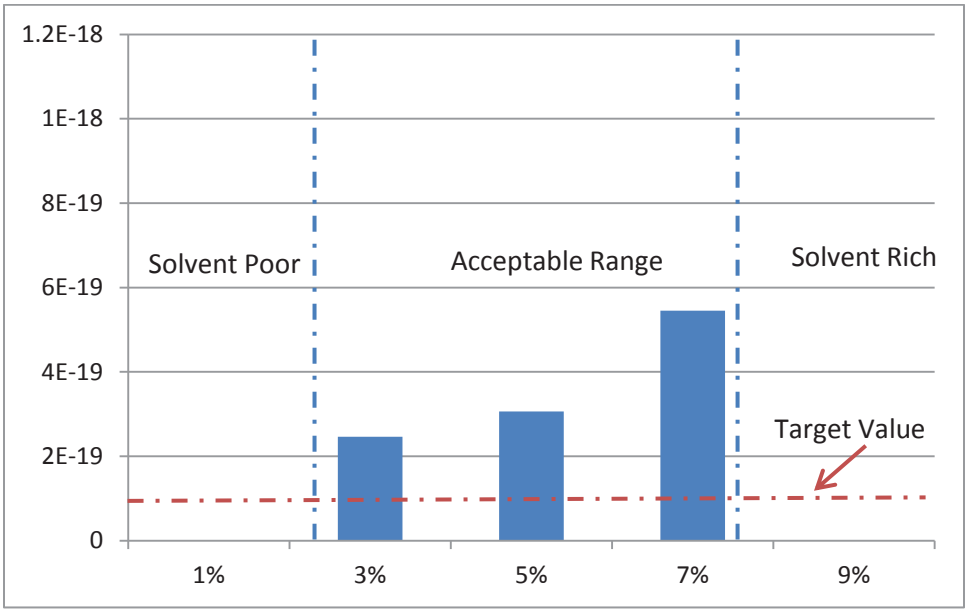

Figure 4.24 Permeability of 3d-printed YSZ electrolyte vs binder content of the printing paste. Sintering temperature = 1400 ^{o}C; solvent was held at 5.5 g

The permeability of YSZ electrolyte has been reported to be around around $1x10^{-19}$ m^2 , our values very slightly higher[5] .

4.6.2. Effect of Solvent content on permeability of YSZ

Data to show the effect of permeability on the amount of solvent can be seen in Figure 4.25. The binder content was held at a constant 3% and the solvent was varied from 4.0 g to 6.5 g. The samples with 4 g and 4.5 g were too viscous and subjected to constrained sintering as their layers had variable densities which are known to cause cracks and hence those samples were much more permeable. The sample with 6.5 g of solvent was not viscous enough again formed cracks and showed higher permeability. The trendline for the intermediate solvent values between 4.4 and 5.7 g went downwards; permeability fell as solvent content of the printing paste rose. To the extent that permeability and porosity correlate with each other, this is consistent with Figure 4.1, where higher solvent content made for lower porosity.

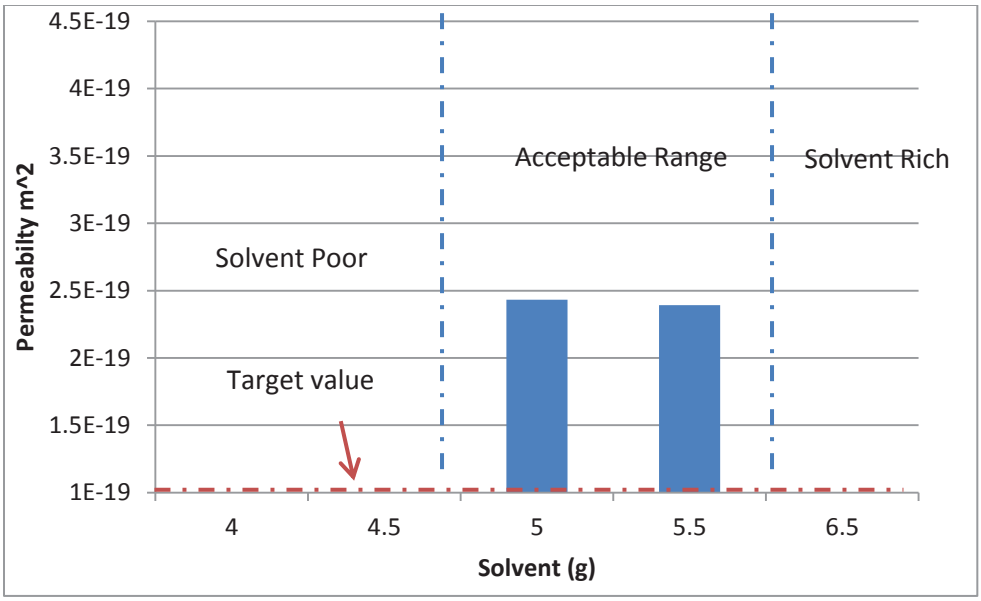

Figure 4.25 Permeability of 3d-printed YSZ electrolyte vs solvent content of the printing paste. Sintering temperature = 1400 ^{o}C; binder content was held at 3%.

4.7. POROSITY DATA FOR SOFC ANODE, NI-YSZ (Nextech)

Having developed an optimized paste for YSZ microextrusion, it was time to develop pastes for printing the electrodes as well. For the electrodes, high porosity and permeability of the printed deposits is considered a positive attribute, as react gases must penetrate into the electrodes to contact the tri-phase boundary at the electrode/electrolyte interface.

The effect of binder on the porosity of sintered disks of Ni-YSZ that were obtained from NexTech was then studied. For this study the ratios of both binder and solvent to the amount of ceramic were varied to obtain a printable paste. As seen in Figure 4.26, as the amount of binder was increased, the porosity of the samples increased. This is consistent with Figure 4.18 for YSZ alone. Even though a smooth curve spanning the 1-9% binder

content was obtained, the samples with binder content 7% and more were difficult to print. All the samples were fired at 1400 °C using a ramp rate of 3 °C per minute and held for 2 hrs.

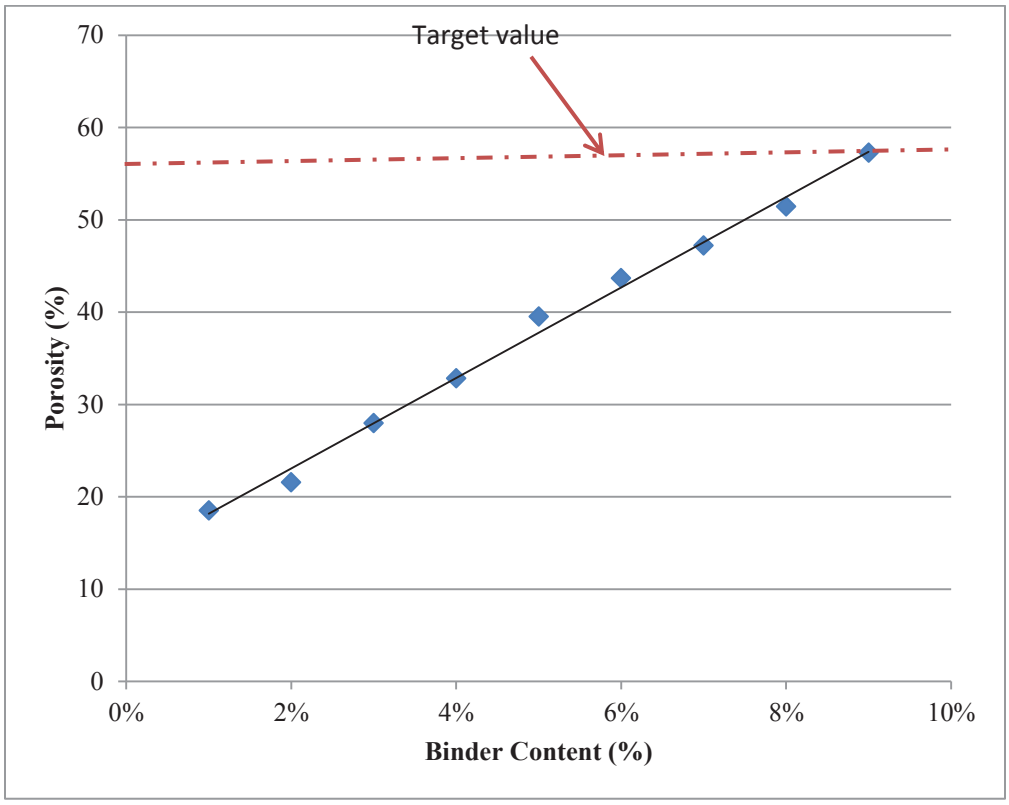

Figure 4.26 Porosity of 3d-printed NexTech Ni-YSZ vs binder content of the printing paste. Sintering temperature = 1400 ^{o}C; solvent and binder content were varied to obtain a printable paste

4.8. CONDUCTIVITY DATA FOR Ni-YSZ Anode, Ni-YSZ (NexTech)

The electronic conductivity in Ni-YSZ was measured using 4 point test method since it is a very good conductor. The conductivity of the samples was measured to be 240 S/cm at 800 °C after the sample bar had been reduced under hydrogen for 0.5 hrs. For samples containing 40% Ni reported to be at 500 S/cm at 900 °C after reduction in hydrogen for 2

hrs [7]. The sample tested contained 9% binder content and its porosity was obtained to be 57%. The main reason for lower conductivity of the sample can be due to the presence of high of porosity in the sample which is in conformity with theory, as it states that electronic conductivity reduces with increase in porosity. Although, it also suggests that open porosity can increase the conductivity if the conducting species are adsorbed onto the pore surfaces.

The sample was also only reduced for about 0.5 hr which might not have been enough time to reduce all of the NiO into Ni. The presence of contact resistance was ignored but it could have also been a small factor.

4.9. SHRINKAGE DATA FOR SOFC ANODE, Ni-YSZ (NexTech)

Figure 4.27 shows the effect of increase in the binder content on shrinkage of Ni-YSZ anode. All the samples were fired at 1400 °C with a ramp rate of 3 °C per minute and held for 2 h. The shrinkage of samples increased as the amount of binder was increased. The samples with binder content 7% and more were difficult to print. There was no need to segregate the data into zones, because shrinkage could be reasonably measured whether the sample was cracked or not. As seen in the graph, the samples did not shrink as much as the samples of YSZ and this was a major concern.

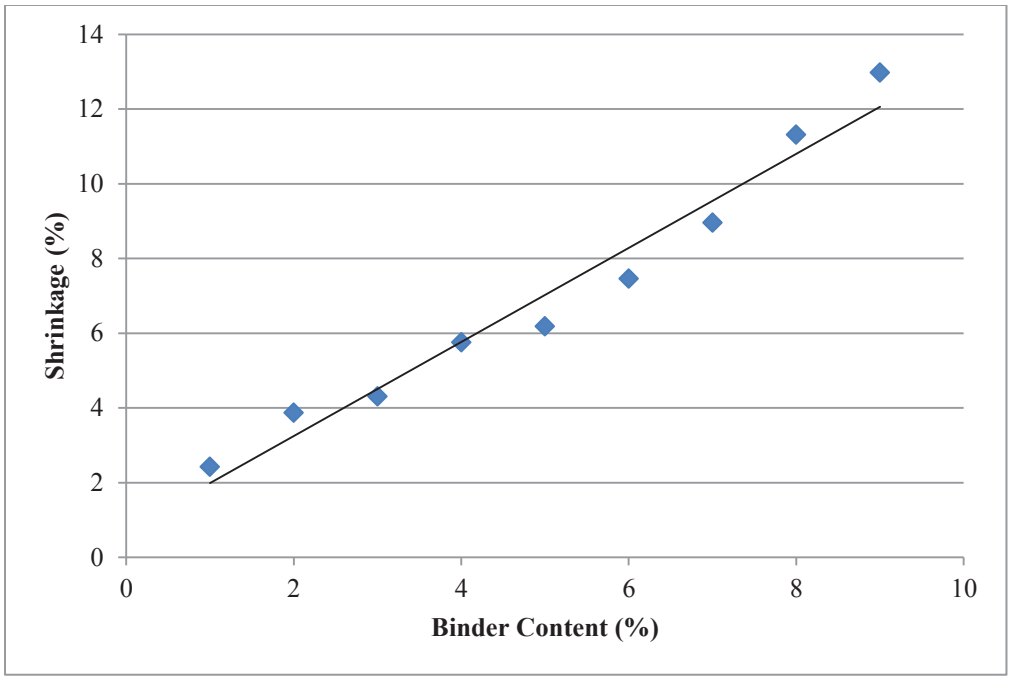

Figure 4.27 Shrinkage of 3d-printed NexTech Ni-YSZ with binder content of printing paste. Sintering temperature = 1400 ^{o}C; solvent and binder content were varied to obtain a printable paste

The difference in shrinkage of YSZ and Ni-YSZ samples was very high. The effect of unequal shrinkage between adjacent phases be seen in Figure 4.28. The samples were co-fired at 1400 °C with a ramp rate of 3 °C per minute and held for 2 h. Constrained sintering due to the differences in shrinkage caused delamination of the YSZ phase from the Ni-YSZ phase. Delamination is clearly visible on the side of the sample, which is shown in Figure 4.29.

Figure 4.28. Mismatch in shrinkage of YSZ-Ni-YSZ fired at 1400 °C.

Figure 4.29. Side view of delamination caused by mismatch of shrinkage of YSZ and Ni-YSZ.

So far all of the parameters tested had to do with paste formulation. The degree of sintering and the performance of the printed part, however, is also dependent on the sintering temperature. In the book by (Minh, Takahashi, Nguyen, & Taka, 1995) who published the data from Argonne labs, shrinkage of SOFC components prepared by tape calendaring was examined as a function of temperature. The accumulated date is graphed in Figure 4.30. It shows an exponential increase in the shrinkage of samples with temperature rather than a linear increase. To examine this aspect, the sintering temperature was dropped to 1300 ^{o}C to take advantage of the narrower shrinkage range.

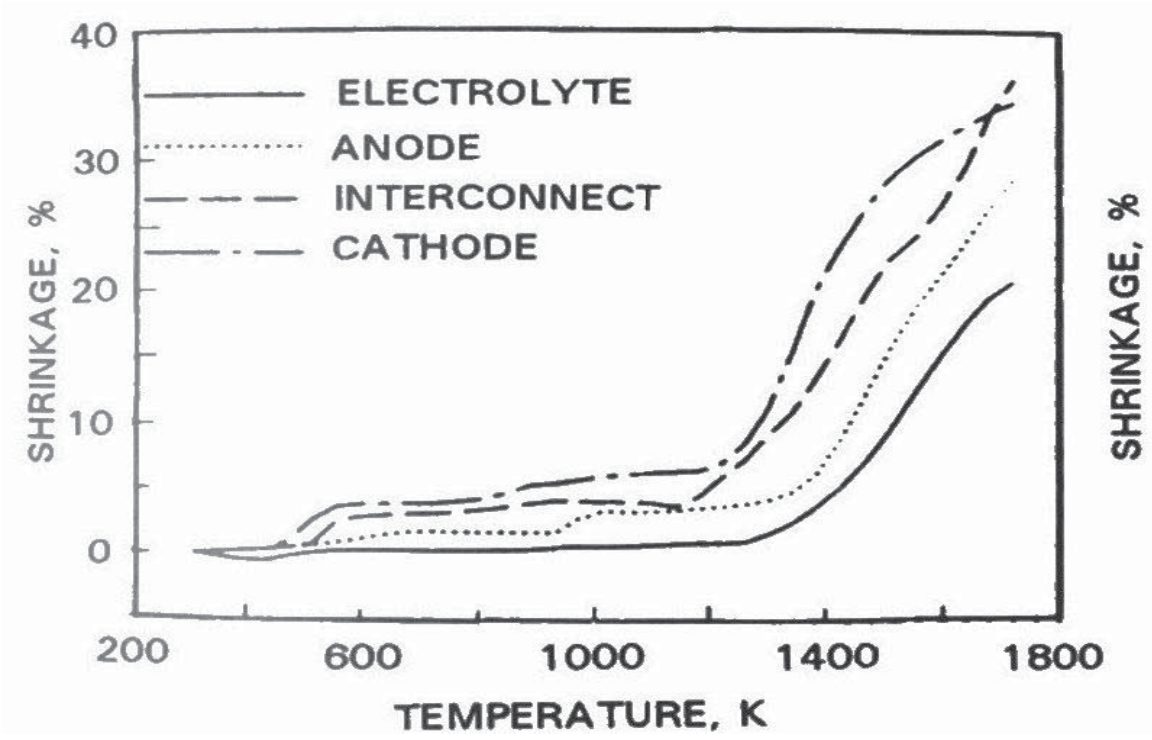

Figure 4.30. Shrinking profiles of different materials [10]

Figure 4.31 (Steil, 1997), plotted the porosity of YSZ samples as a function of temperature. As seen in the graph the porosity of the samples increased once the sintering

temperature was dropped below 1200 °C. So, it was safe to conclude that the reduction in sintering temperature would not affect the porosity of YSZ samples.

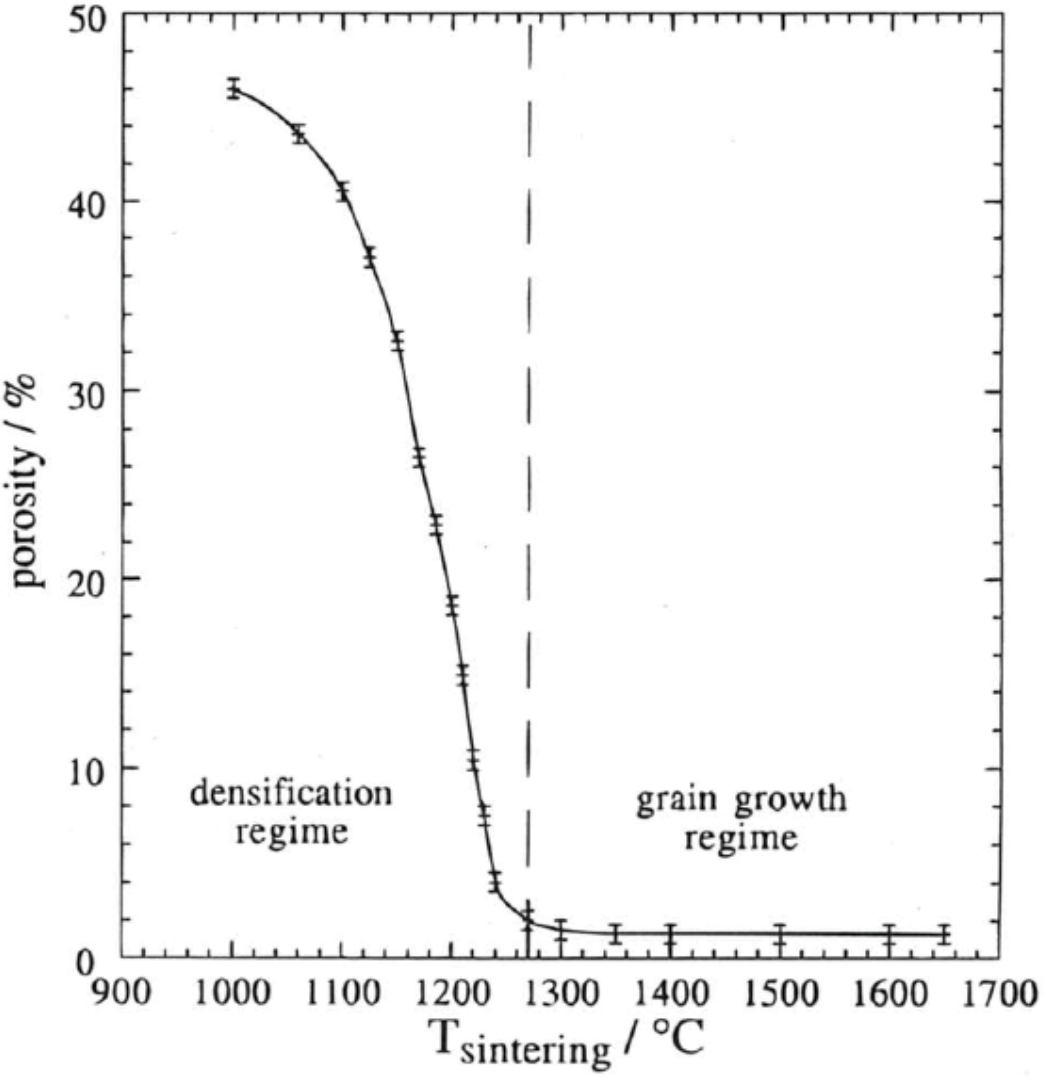

Figure 4.31. Porosity of YSZ as a function of sintering temperature [8]

4.10. SHRINKAGE DATA FOR SOFC CATHODE, LSM-YSZ

The effect of binder content on the shrinkage of LSM-YSZ samples can be seen in Figure 4.32. All the samples were sintered at 1300 °C with a ramp rate of 3 °C per minute and

held for 2 h. The ratios of both binder and solvent were again varied with a constant amount of ceramic to achieve a printable paste. The samples with binder content more than 7% were difficult to print. According to the data in Figure 4.32, shrinkage of LSM-YSZ samples increased with increase in binder content, consistent with the other component pastes. The shrinkage of LSM-YSZ samples is very close to the shrinkage of YSZ samples which was shown in Figure 4.26.

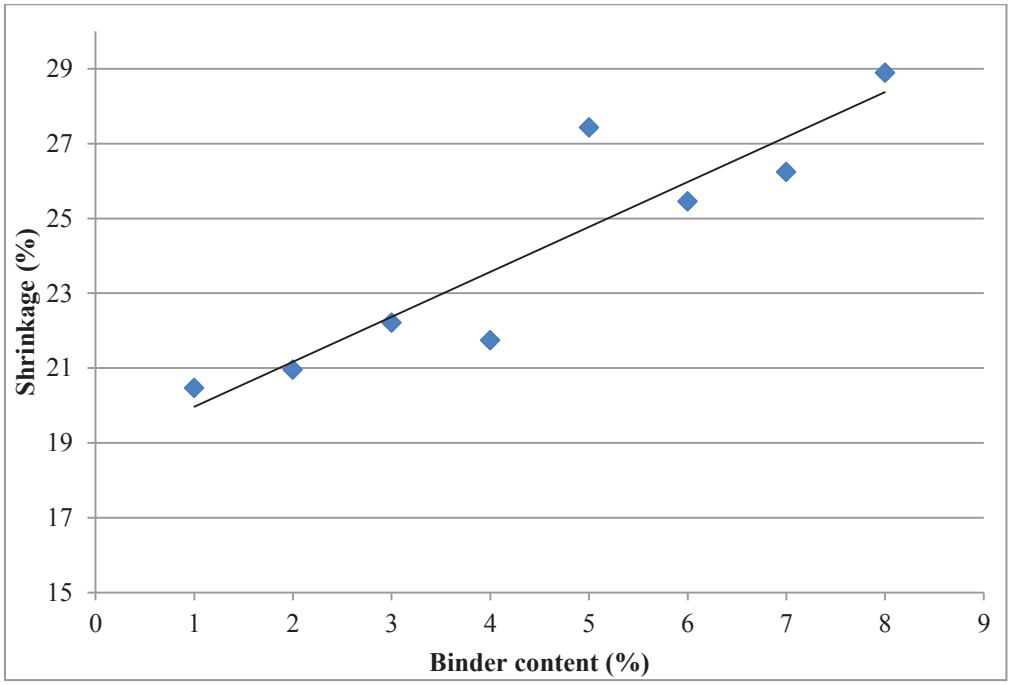

Figure 4.32 Shrinkage of 3d-printed LSM-YSZ cathode vs binder content of the printing paste. Sintering temperature = 1300 ^{o}C; solvent content was varied along with binder content to obtain a printable paste

4.11. POROSITY DATA FOR SOFC CATHODE, LSM-YSZ

The porosity data for LSM-YSZ samples is presented in Figure 4.33. All the samples for this data were sintered at 1300 °C with a ramp rate of 3 °C per minute and held for 2 h.

The porosity of the samples increased with an increase in the binder content, consistent with anode data in Figure 4.25 and electrolyte data in Figure 4.18. The samples with binder content 7% and more were difficult to print.

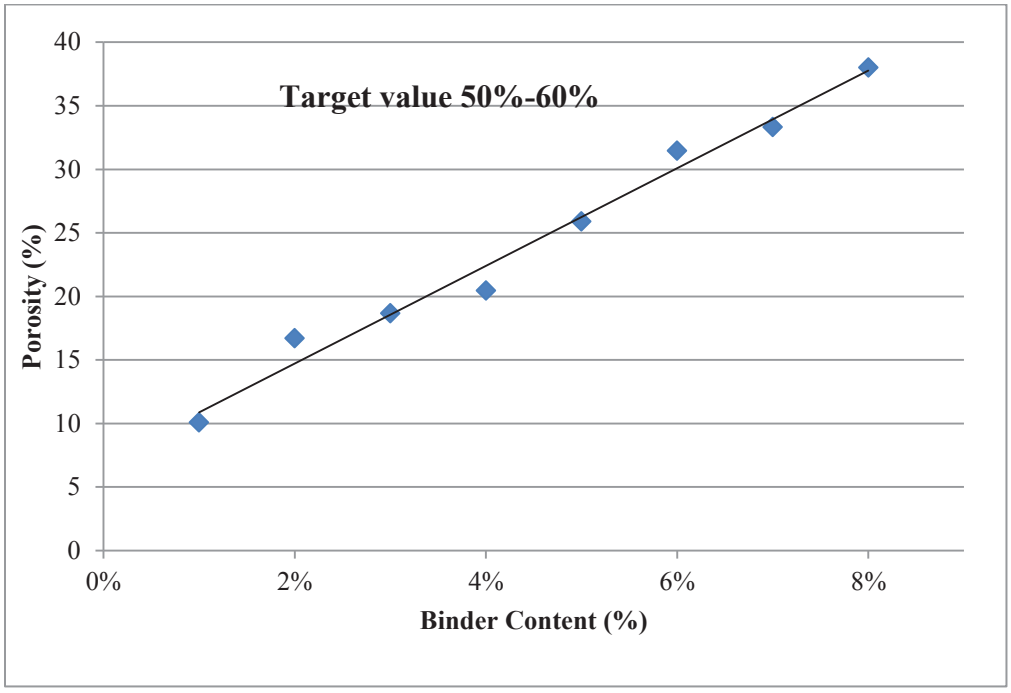

Figure 4.33 Porosity of 3d-printed LSM-YSZ cathode samples vs binder content of the printing paste. Sintering temperature = 1300 ^{o}C; solvent content was varied along with binder content to obtain a printable paste

4.12. CONDUCTIVITY DATA FOR SOFC CATHODE, LSM-YSZ

The electronic conductivity of LSM-YSZ sample was measured using 4 point test method. The conductivity of the samples was measured to be 2.14 S/cm at 800 °C in air. Literature values have been reported to be at 3.60 S/cm at 900 °C [9], [11]. The sample tested contained 8% binder content and its porosity was obtained to be 38%. The electronic conductivity was of the sample was lower due to the presence of porosity

which is in conformity with theory, as it states that electronic conductivity reduces with increase in porosity. It also suggests that open porosity can increase the conductivity if the conducting species are adsorbed onto the pore surfaces.

4.13. COFIRING OF SOFC COMPONENTS

4.13.1. Three-layer cofiring with NexTech NiO

All three SOFC layers were cofired along with LSM-YSZ, but the sintering temperature was dropped from 1400 °C to1300 °C with a ramp rate of 3 °C per minute and held for 2 h. The result is shown in Figure 4.34. There was no delamination observed, but because there is a mismatch in the shrinkage of each layer (compare Figures 4.32, 4.27, and 4.20) the sample was warped, which is evident in Figure 4.34.

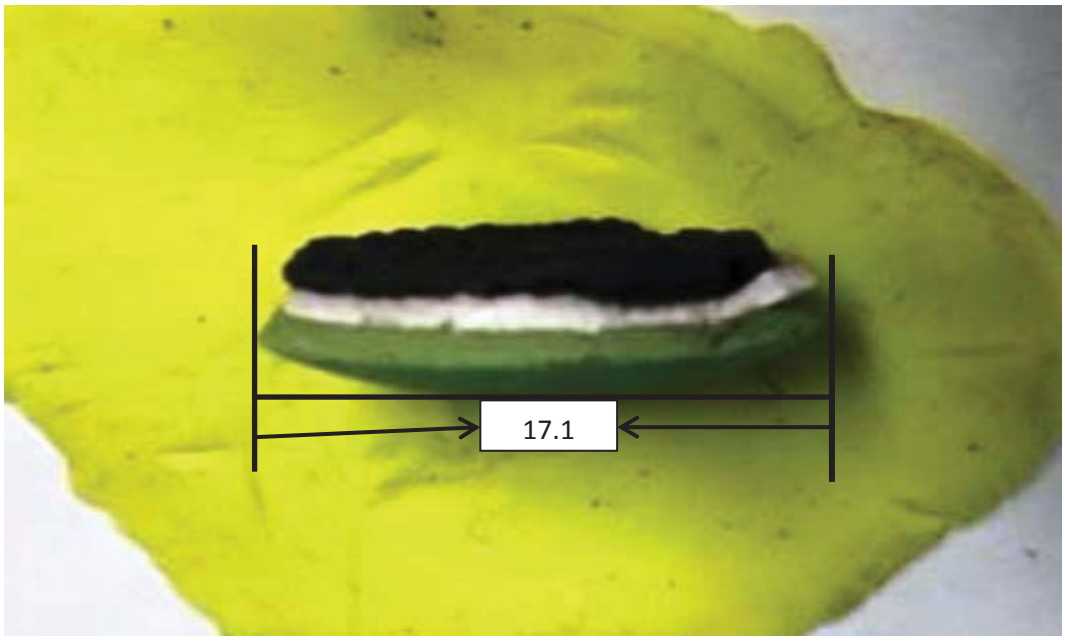

Figure 4.34. Warping caused by shrinkage mismatch of different fuel cell component layers

The interface of the sintered layers examined under an SEM can be seen in Figures 4.35 and 4.36. The properties required for each layer had been maintained. The Ni-YSZ (anode) layer, LSM-YSZ (cathode) layer both showed porosity and the YSZ (electrolyte) as seen was dense.

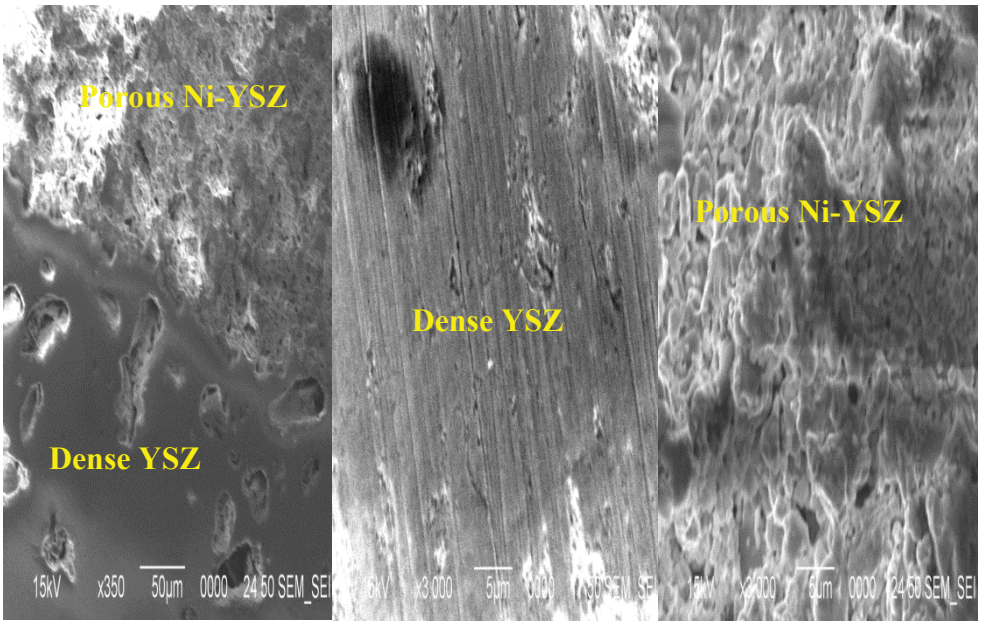

Figure 4.35. Interface of Anode (Ni-YSZ) and (YSZ) electrolyte layer, sintered at 1300 °C

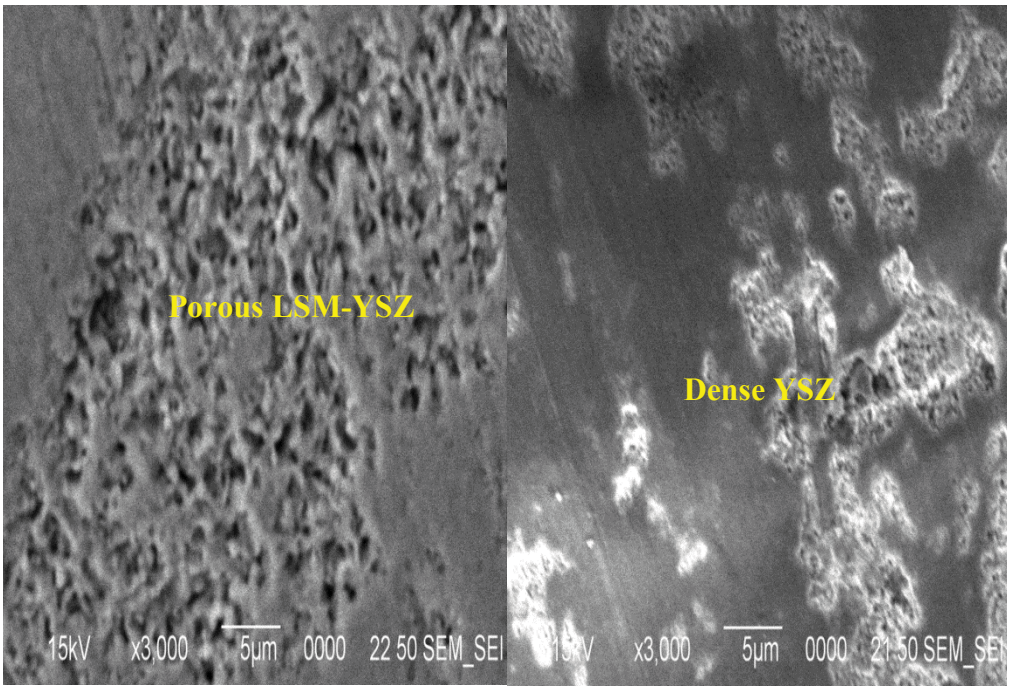

Figure 4.36. Interface of ANODE (LSM-YSZ: 50-50%) with (YSZ) electrolyte layer sintered at 1300 °C.

4.13.2. Shrinkage of NiO-YSZ anode using NiO nanopowder

The shrinkage of Ni-YSZ phases either had to be increased, or the other two phases decreased; variation in binder content could increase shrinkage, but to approach 20% shrinkage, it would have to rise well outside workable limits of the paste. Thus binder content could not be used to achieve shrinkage that could be matched with the shrinkages of LSM-YSZ and YSZ samples. Use of nanopowders was required.

NiO nanopowders were obtained and mixed with 60% YSZ. The limited availability of powder allowed for only two samples to be prepared. The shrinkage levels obtained are shown in Figure 4.37. The shrinkage was in the range of the LSM-YSZ and YSZ powders.

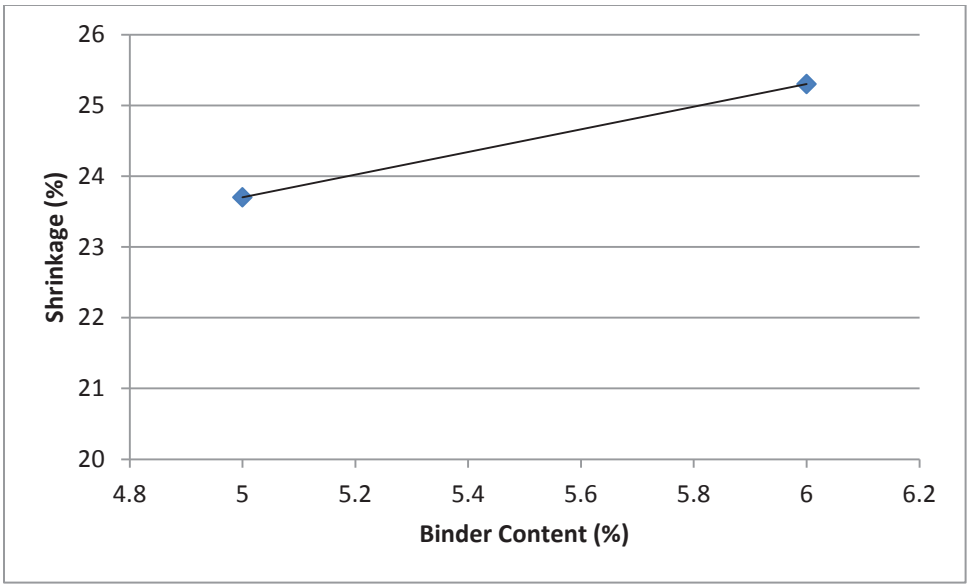

Figure 4.37. Shrinkage of 3d-printed anode using NiO nanopowder vs binder content of the printing paste. Sintering temperature = 1300 ^{o}C; solvent content was varied along with binder content to obtain a printable paste

4.13.3. Porosity data for Ni-YSZ (NiO nanopowder- Sigma Aldrich)

Figure 4.38 shows porosity data for the paste formulated using 40% NiO nanopowder blended with 60% YSZ. The porosity of the sample was reduced with lower binder content, consistent with all the other component paste formulations. Employing smaller particles should also serve to reduce porosity, as reduction in particle size increases densification. Our limited data in this regard found that trend to be correct: comparing the nanopowder data in Figure 4.34 to Figure 4.25 employing NexTech NiO, 5% binder content had porosity fall from 39% to 34.5% and 6% binder content has porosity fall from 42% to 38.9%.t However, note that the sintering temperature for the nanopowder had been reduced to 1300 °C while the NexTech powder was sintered at 1400 ^{o}C, so the

difference in porosity for the two powders under the same conditions would likely have been even greater.

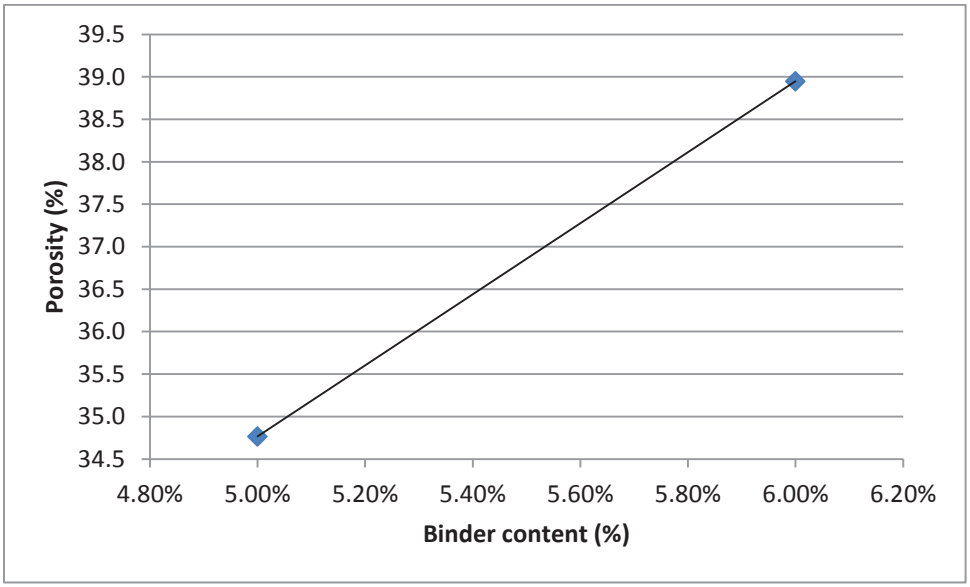

Figure 4.38 Porosity of 3d-printed anode using NiO nanopowder vs binder content . Sintering temperature = 1300 ^{o}C; solvent content was varied along with binder content to obtain a printable paste

4.13.4. Three-layer firing using NiO nanopowder

Having achieved general shrinkage parity among the 3 SOFC layers, it was time to try again printing the layers in succession, on top of each other, and cofiring them. A button SOFC fuel cell was printed using the NiO nanopowders containing 6% binder. The YSZ contained 3% binder and LSM-YSZ contained 7% binder. The shrinkage-binder content plots for each component are overlaid in Figure 4.39. The estimated shrinkage for each phase was within 7% of the others. As a result, the pastes were consecutively printed on top of each other, the shrinkages matched, and there was no warping observed in the system after cofiring at 1300 ^{o}C. A photograph is shown in Figure 4.40.

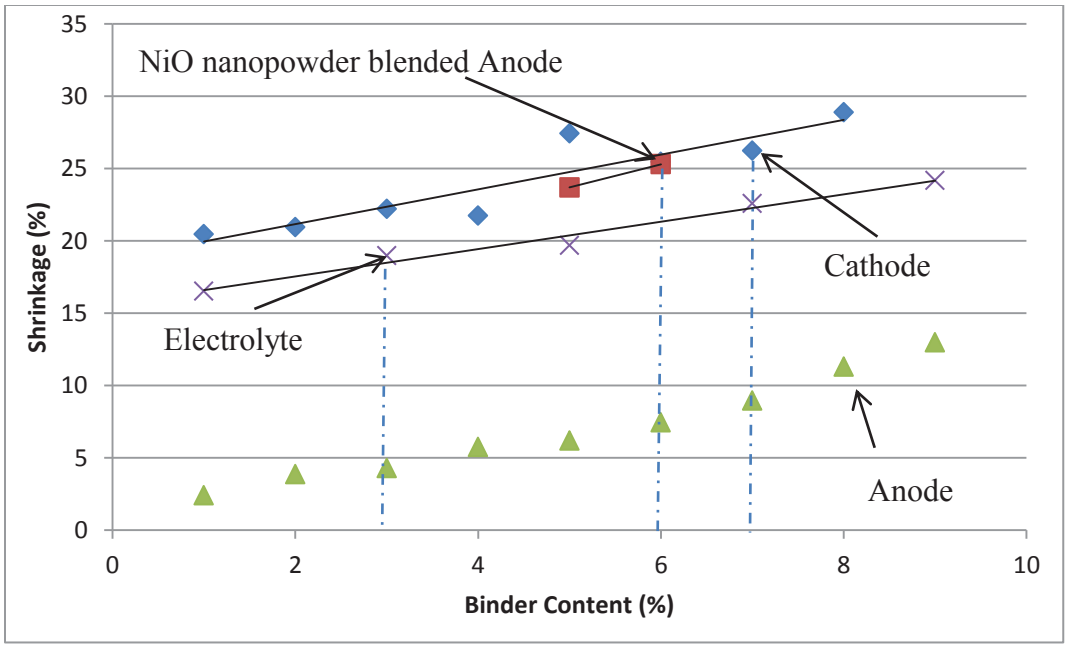

Figure 4.39. Shrinkage data for 3d-printed SOFC anode, cathode and electrolyte. Actual shrinkages and paste binder contents employed are shown.

Figure 4.40 Photograph showing matching shrinkage of printed and cofired SOFC components

4.13.5. Galvanic performance

The galvanic performance (voltage-current density curve) of the cell was obtained by mounting the 3-layer button in the Probostat and heating to 800 ^{o}C. Air was supplied to the LSM-YSZ cathode and H_2 to the NiO nanopowder anode at flowrates of 10 mL/s. An external load box was connected across the two electrodes, so that the voltage-current dependence could be measured. The sample had an open circuit voltage of 0.845 V. A voltage vs current density graph was obtained as seen in Figure 4.41. The resistance of the cell was calculated from the slope of a V-I curve and was found to be 214 Ω.

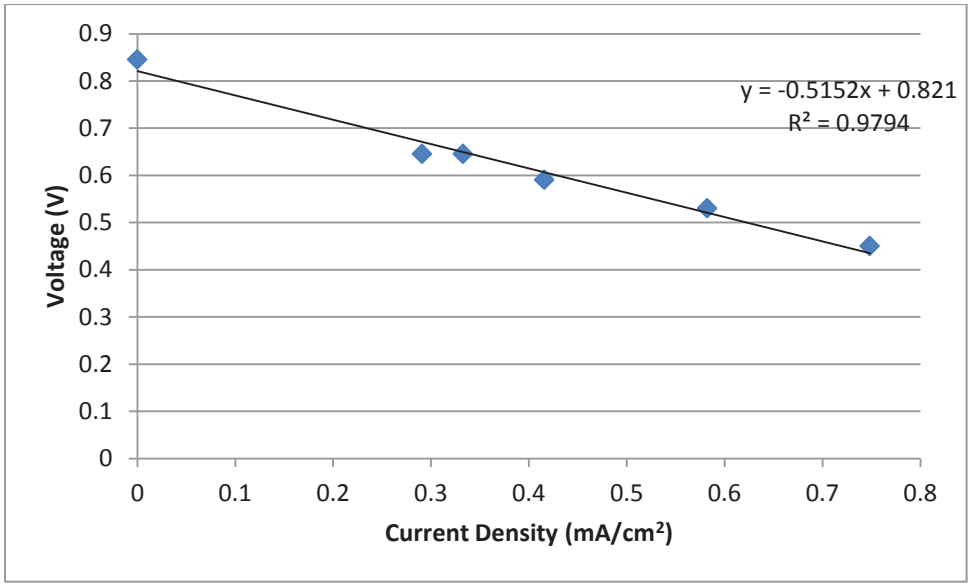

Figure 4.41. Voltage vs current density for a 3d-printed SOFC button. Operating temperature = 800 ^{o}C; H_2 and air supplied at 10 mL/min.

The straightness of the V-I curve would indicate that the cell was resistance-limited. This is often the case in high temperature electrochemistry, where thermal activation barriers for chemical reaction are easily surmounted. The open circuit voltage approached but did not quite reach values obtained with 1.0 atm of H_2 in commercial screen-printed button

SOFCs at 1.0 atm, typically 1.0-1.1 V [10]. This usually indicates some gas leakage; the permeability of the 3d-printed YSZ electrolyte was small, but nevertheless measureable and found to be slightly above commercial values. The permeability of the cofired sample was 1.50 x 10^{-18} m^2, as mentioned previously the required permeability is 1 x$10^{-19}$$m^2$ so ours was higher than commercially available products, it should be noted that commercially available products are never cofired and are usually fabricated one layer at a time. Thus, obtaining nearly milliamperes of current per square centimeter of electrode area in the same voltage range as other fuel cells under load is a good first step. Performance enhancements should accrue from decreasing the linewidth of the printer and producing thinner layers.

CHAPTER 4

REFERENCES

1) Dahl, P., Kaus, I., Zhao, Z., Johnsson, M., Nygren, M., Wiik, K. Einarsrud, M. . (2007). Densification and properties of zirconia prepared by three different sintering techniques. *Ceramics International*, *33*(8), 1603–1610. doi:10.1016/j.ceramint.2006.07.005

2) Retrieved on October 5th 2016, from http://www.med.harvard.edu/jpnm/physics/refs/xrayemis.html

3) Ramachandran, G. (2011). *Assessing nanoparticle risks to human health*. Amsterdam: Elsevier

4) Turco, M., Ausiello, A., & Micoli, L. (n.d.). *Treatment of biogas for feeding high temperature fuel cells: Removal of harmful compounds by adsorption processes*

5)Glass, S. J., & Green, D. J. (2004). Permeability and infiltration of partially Sintered ceramics. *Journal of the American Ceramic Society*, *82*(10), 2745–2752.

6) Luo, D., Luo, Z., Yu, C., & Cen, K. (2007). Study on Agglomeration and Densification Behaviors of Gadolinium-Doped Ceria Ceramics. *Journal of Rare Earths, 25*(2), 163-167. doi:10.1016/s1002-0721(07)60066-0

7) Aruna, S.t, M. Muthuraman, and K.c Patil. "Synthesis and Properties of Ni-YSZ Cermet: Anode Material for Solid Oxide Fuel Cells." Solid State Ionics 111.1-2 (1998): 45-51

8) Steil, M. C. (1997). Densification of Yttria-Stabilized Zirconia. *Journal of The Electrochemical Society*, *144*(1), 390. doi:10.1149/1.1837416

9) Zhang, C., Li, W., Liao, H., Li, C., Li, C., & Coddet, C. (2007). Microstructure and Electrical Conductivity of Atmospheric Plasma-Sprayed LSM/YSZ Composite Cathode Materials. *Journal of Thermal Spray Technology, 16*(5-6), 1005-1010. doi:10.1007/s11666-007-9115-7

10) Minh, N. Q. (2005). *Science and technology of ceramic fuel cells* (2nd ed.). Oxford, United Kingdom: Elsevier Science

11) Leng, Y. J., Chan, S. H., Khor, K. A., & Jiang, S. P. (2004). Development of LSM/YSZ composite cathode for anode-supported solid oxide fuel cells. *Journal of Applied Electrochemistry*, *34*(4), 409–415. doi:10.1023/b:jach.0000016627.29374.24

CHAPTER 5

CONCLUSION

5.1 INITIAL TRIALS

- Manual mixing or ball milling could not be used to produce a homogenous suspension for extrusion. The dual axis centrifuge proved vital for the success of this project.
- Despite its desirability from an environmental perspective, water was not a suitable solvent for extrusion for YSZ paste extrusion as it made the paste too viscous and the printed parts lacked definition.

5.2 MAIN EXPERIMENTS

The conclusions that can be drawn from this work are:

5.2.1 Porosity

- The porosity of ceramic samples fabricated by microextrusion 3d printing increases with increase of binder content.
- Solvent content does not have a huge effect on porosity, but porosity can be caused due to defects in the samples as a result of constrained sintering.

5.2.2 Shrinkage

- Shrinkage increased with increase in binder content of the samples. Optimum binder content was 3% for YSZ ,7% for LSM-YSZ AND 6% for Ni-YSZ.

- Shrinkage is also affected by amount of solvent present in a sample as the solvent escapes the sample during the drying stage. An optimum solvent content was between 5-5.5 g when YSZ paste contained 3% binder content. LSM-YSZ and Ni-YSZ paste formulations were prepared by varying both binder and solvent content to achieve printable pastes.

5.2.3 Ionic Conductivity

- The ionic conductivity of the samples reduced as the binder content was increased, literature values have been reported around 2.099 S/m for YSZ and our data indicates that the highest conductivity was achieved in the least porous sample.
- The ionic conductivity was affected by the amount of solvent but this was again due to the occurrence of porosity which was caused because of constrained sintering.

5.2.4 Permeability

- Permeability increased with the increase in binder as porosity increased which causes the probability of having open channels to increase.
- The permeability of the samples was affected greatly by the amount of solvent, as constrained sintering due to the presence of variable densities caused the samples to have cracks

5.2.5 Final Conclusions

- Solvent and binder content were treated as independent variables in order to determine optimum paste compositions, but it was found that for any given ceramic, only a narrow range of solvent-to-binder ratios and proportions to other paste components could satisfy the multiple requirements of viscosity, sinterability and shrinkage.
- Microextrusion 3d printing of ceramics can be used to produce dense ceramic structures. YSZ could be printed with 90% of theoretical density with a permeability of $2.46 \times 10^{-19} m^2$.
- Particle size is the most important characteristics that can enhance shrinkage and also lower sintering temperature. The density of the sintered sample is affected by its green packing density; particle shape only becomes relevant if it inhibits the packing density of the green sample.
- Ni-YSZ is sintered at 1400 °C, the adoption of NiO nanopowders allowed for lowering its sintering temperature to 1300 °C and ultimately allowed for cosintering of all the components.
- Paste compositions were derived such that all the components of SOFCs can be printed consecutively and retain their respective properties on cosintering.
- Galvanic performance from an SOFC button cell was obtained. The open cell voltage was lower (0.845 V); typically the OCV for SOFC's is around 1.05 V. The internal resistance of the cell obtained was 214 Ω, commercially available devices have resistances around 5-10 Ω at 750 °C [1]. The thickness of the electrolyte for commercial products is about 0.30 μm whereas; it was about 1.6 mm for the ones fabricated by us. Hence, the performance of 3d printed button

cells can be expected to improve as the diameter of the extrusion orifice is reduced, enabling thinner layers.

CHAPTER 5

REFERENCES

1. Khan, Feroze. Effect of Hydrogen Sulfide in Landfill Gas on Anode Poisoning of Solid Oxide Fuel Cells. Thesis. Youngstown State University, 2012

APPENDIX A

A1 Hyrel 3D Printer

The Hyrel 3d printer is comprised of six main components:

- The machine itself.
- Extruders: The extruder printer heads are attached to the machine.
- Accessories: These are additional accessories which may help with the fabrication
- Tool kit: These are provided to update the firmware and help with the maintenance of the machine.
- Removable glass platform: This is the platform on top of the heatable metal platform that the material adheres to.
- Repetrel: This is the software program that controls the machine. The Hyrel printer is capable of building objects measuring up to 200 x 200 x 200 mm.

Hyrel currently provides two types of extrusion heads

1.) Mk1 Extruder – for 1.75mm or 3mm filaments for plastic materials such as PAB etc.,

2.) EMO-25 – for emulsifiable - type of materials such as pastes or clay [1].

- **Loading Heads**

The Hyrel printers can be equipped with 4 extruder heads and therefore can print multiple materials on the same print head simultaneously. The extruder head was loaded in the 4th

position on the control arm by simply sliding into the slot. A blue light on the extruder head lights up once it had successfully made a stable connection with the machine [1].

A.1.1 Hyrel Tramming (leveling)

In order to prepare the build plate for printing, a glass slab was cut to suitable dimensions to be placed on the build plate. The glass slab was be held securely on the build plate with the help of carpenters tape to prevent it from sliding on the heated bed as shown in Figure A.1.

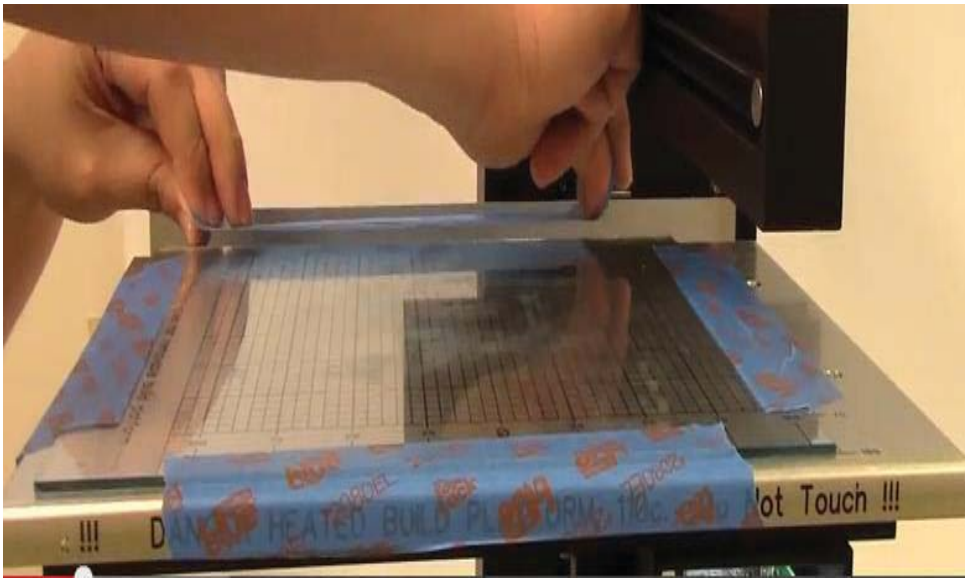

Figure A.1. Glass slab on heating bed

Then the dial gauge was installed using the thumb screws for head #2 and was made sure that the gauge did not rest on the Y-arm. Once that had been done, the next step was to go into Repetrel and unlock motors was selected which enabled us to move the dial gauge directly in the middle of the build plate. Then using a series of +z and –z keys in Repetrel, the dial gauge was zeroed out. When this task had been completed, the next step

was to exit out of the z calibrations command by clicking the red key in the Repetrel. This was followed by using a 2.5 mm wrench to unlock the 4 screws underneath the build plate, holding the bed in place. Once this had been done, the bed was heated to about 55 °C. Once the bed had reached temperature, a hex key was used to loosen the screws located underneath the bed plate .The dial gauge was then placed at all four corners of the bed, adjusting the screws as necessary to make sure that the dial gauge read zero at all of them. Once this had been done, the bed was locked in place by using the 2.5 mm key to tighten the screws underneath the bed. The dial gauge was then removed as the print bed had been successfully leveled.

A.1.2 Paste Cartridges

The original printer setup did not have the capability for extrusion. This required the acquisition of the EMO 25 Extruder head (Standard) package. The package included the following:

- One (1) EMO 25 Extruder Apparatus
- One (1) EMO 25 Cartridge
- One (1) EMO 25 Nozzle Kit = 3 nozzles
- One (1) Block of Plasticine Clay

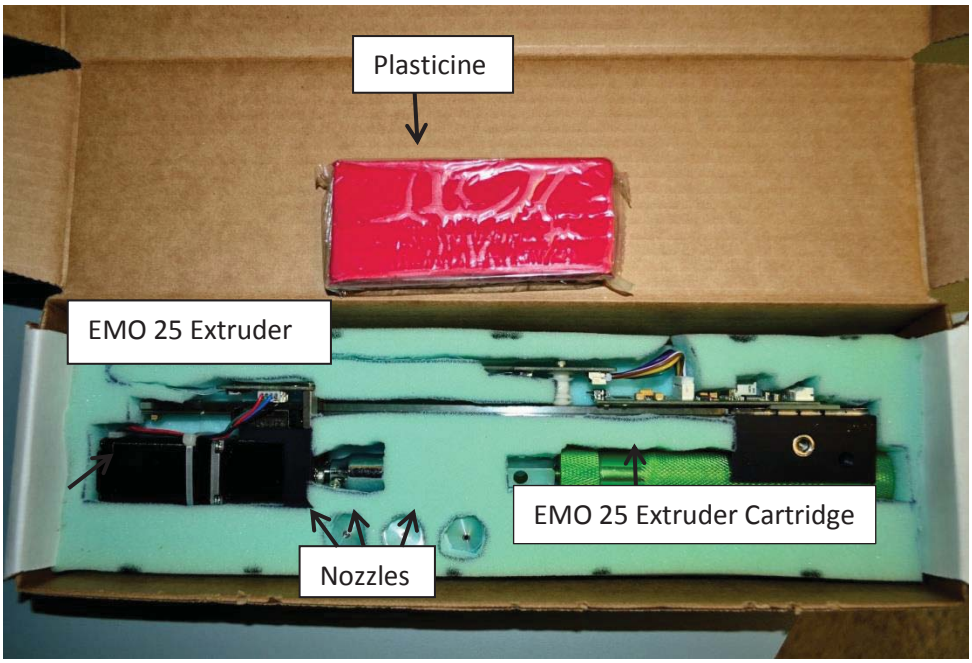

Figure A.2 EMO 25 Extruder package [1]

The original nozzles were of the size 1 mm, 1.5 mm and 2mm. The original nozzles dragged the pastes on printing.

Figure A.3. Original nozzle

The nozzle needed to be replaced to prevent dragging of paste. The nozzle was replaced with a LEUR needle of pore size 0.8 mm.

Figure A.4. In house fabricated nozzle

A.1.3 Calibrating the EMO extruder

This is done by hitting commands “Home X-Y”, “Park” and then “Enable Z calibrate”. A paper was placed on top of a ceramic plate, which in turn is placed on top of the glass plate. The nozzle of the extruder cartridge needed to be maneuvered until the paper could be barely removed from underneath it. The calibration was then completed.

A.1.4 Firmware and Software Updates

Since the printer was not originally designed for extrusion, the company was constantly updating the firmware to adapt the printer for extrusion. The firmware for the control arm and bed needed to be updated by connecting into the mother board located in the back of the control arm. The firmware version depended upon the version of the machine acquired and shown is shown in Figure A.5.

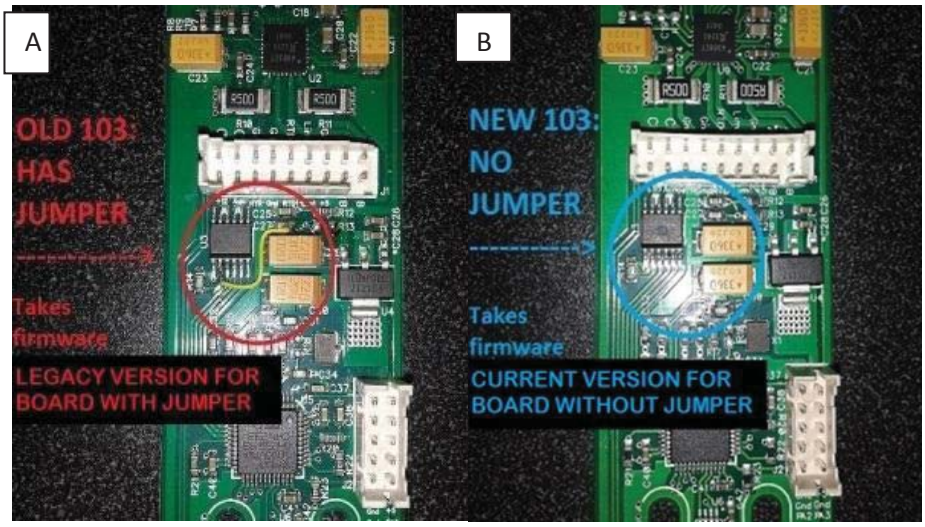

Figure A.5. Firmware based on the wiring in the motherboard of the printer, the printer we have is of the older configuration

The printer used in this research was version A. Along with the firmware,Repetrel and Splicerneeded to be updated.The updates were downloaded from the Hyrel website [1].

The components of the ProboStat^{TM}for the button cell system are:

- the outer alumina tube: Helps shield from the outer atmosphere;
- the inner alumina tube: The button cell and the gold o-ring are supported on the inner alumina tube;
- inner gas tube: Inner gas (air or supply gas to the cathode (inner electrode)), the platinum contact for the electrode is placed on top of the inner gas tube, which is supported by a compressed Tygon hose.
- inner platinum contact: It is sandwiched between the cathode of the sample cell and the inner gas supply tube. It is very delicate and very prone to breaking at the

joint. Hence we ran a platinum wire through the dual holes of the tube; instead of spot welding it; we bent the platinum wire and wrapped a platinum mesh around it as shown in Figure A.6.

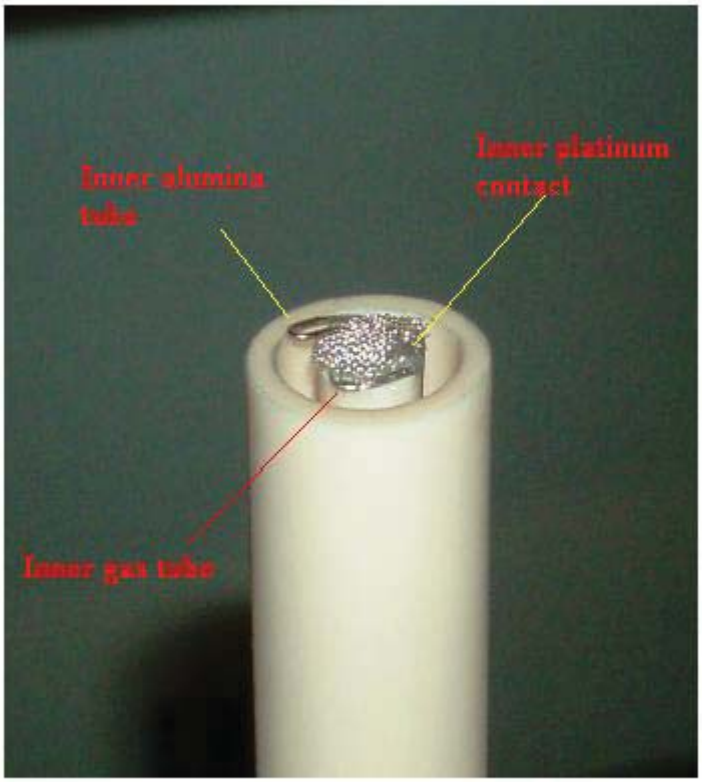

Figure A.6. Inside assembly [2]

- Gold o-ring/Ceramic adhesive: It is placed on the inner alumina tube to provide a gas tight seal between the 2 gas compartments. The gold o-ring needed to be replaced after a few runs so it was replaced by an alumina-filled ceramic adhesive paste called Ceramabond 552 obtained from Aremco. The ceramic paste was applied to the test button samples and it was allowed to dry at room temperature for about an hour. It was then cured at two temperature steps (200^{o}F and 500^{o}),

for 2 hours each before being tested. A good seal was obtained using the ceramic adhesive but the samples had to be removed from the sample holder (tube) using a dremel tool as the ceramic adhesive would form a strong bond with the silica sample holder. Almost all samples were destroyed in the removal process.

- Outer platinum contact: It has to be placed on top of the outer electrode of the sample button cell.

- Spring supported rods: A triangle-shaped alumina plate is placed on top of the outer platinum contact. The three alumina rods with the springs are hooked to the bottom of the inner alumina tube.

- Outer gas tube: It is a clear quartz tube which directs the outer gas to flow to the outer electrode compartment. The curved upper end just sets into the central hole of the tri-shaped alumina plate which is placed on top of the outer platinum contact. It is supported at the base by a segment of flexible plastic tubing.

- Thermocouple: It is a K-type thermocouple and is very effective in monitoring the temperature inside the reaction compartment. If the temperature setting on the furnace is lower than the temperature inside the ProboStat^{TM} then it can be concluded that there is a leak in the system. The ProboStat^{TM}has 3 inputs to connect a thermocouple reader, each input corresponds to a particular set of pins where the thermocouple is connected.

- Four quick-connects: The ProboStat^{TM}has 4 quick-connect gas fittings altogether. Two of them would supply gases to the oxidation and reduction compartments and two would remove the products of reaction from their respective

compartments. The inlet gas quick-connects have a check valve in them. A check valve is installed to prevent any gases from the ProboStat™ to flow back into the gas line.

- Electrical pins: There are 16 pins for electrical connects (Figure A.7) around the base of the inner aluminum tube. The ProboStat™ also has three switches (Figure A.8) which controls shielding.

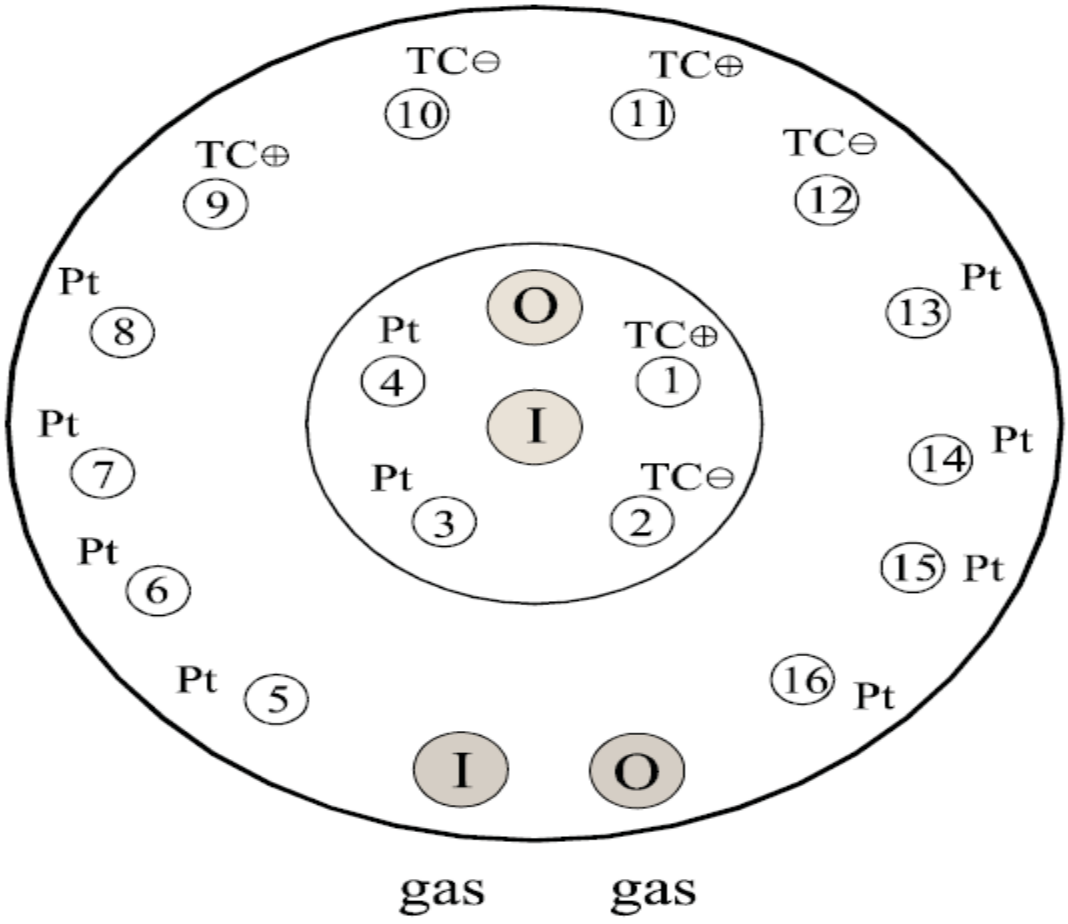

Figure A.7. Top view of the ProboStat™ pin connections

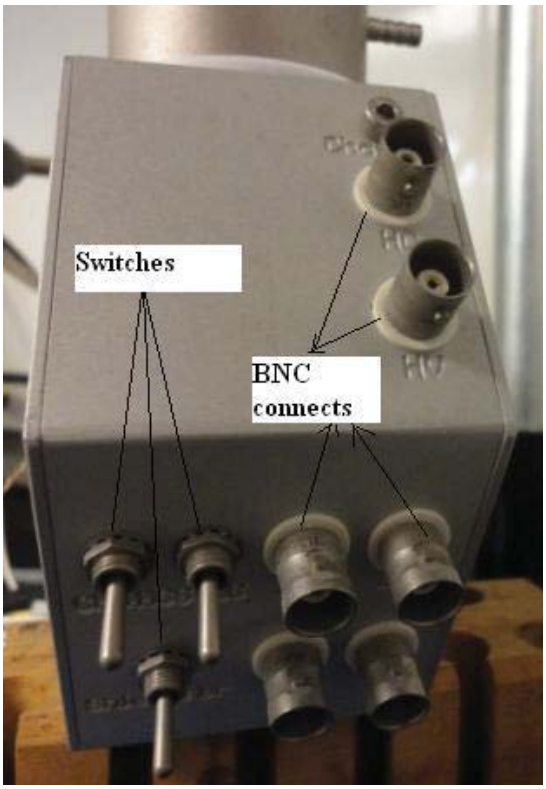

Figure A.8. BNC connects and switches

The assignments of the 16 pins are as follows:

1. TC inner: Thermocouple connects inside the inner alumina tube (Bottom input thermocouple reader)
2. TC inner : Thermocouple connects inside the inner alumina tube (Bottom input thermocouple reader)
3. ILV : Inner low current
4. ILV : Inner low current
5. LCS : Low current shield

6. LC : Low current
7. LVS : Low voltage shield
8. LV : Low voltage shield
9. TC : Thermocouple connects outside the inner alumina tube (Top most input thermocouple reader)
10. TC : Thermocouple connects outside the inner alumina tube (Top most input thermocouple reader)
11. TC : Thermocouple connects outside the inner alumina tube (middle input thermocouple reader)
12. TC : Thermocouple connects outside the inner alumina tube (middle input thermocouple reader)
13. HV : High voltage
14. HVS : High voltage shield
15. HC : High current
16. HCS : High current shield

- Switches: When the switches are turned off (down) the system is grounded and isolated when on. There are 6 BNC connects (Bayonet Neill–Concelmanis a common type of RF connector used for coaxial cable). The 2 pins inside the ProboStat^{TM} correspond to a particular BNC connect. There are 2 pins assignedfor

every BNC connect. BNC connectors corresponding to ILV AND HV were used for convenience because they correspond to pins 3 and 4 of the inner platinum contact and 13 and 15 of the outer platinum contacts. When using the aforementioned pins the system is not affected if one of the switches is switched on by accident.

The button cell was set up as shown in Figure A.10. Physical electrical contact is maintained between the Pt lead wires and the electrode by spring force on the triangle-shaped alumina plate on the outer surface and the compression force by the flexible tube supporting the inner gas tube . The gas-tight seal between the inner and outer electrode compartment is maintained by the gold o-ring.

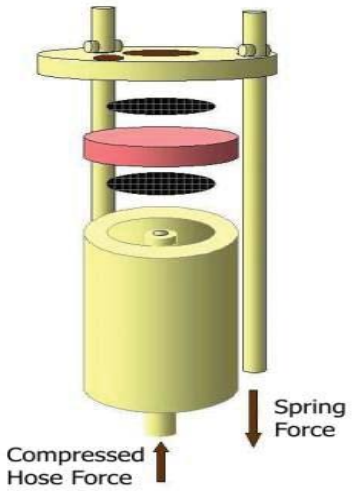

Figure A.9. Forces applied on the sample disk [2]

The outer gas was transported through a quartz tube. The button cell sample has to be contacted with 2 platinum electrodes. Figure A.10 below shows the complete button cell assembly.

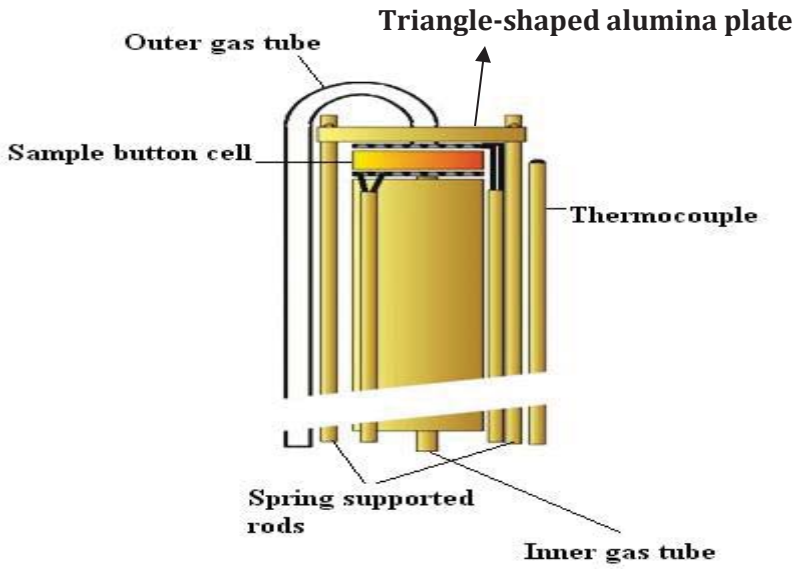

Figure A.10. Complete button cell assembly [2]

A.1.5 Other miscellaneous instruments

- Mass flow controller module: It was bought from Brooks Instruments. It can essentially control four mass flow controllers simultaneously. It is very easy to use. The set point button is used to set the flow needed from a particular gas flow meter (Figure A.11).

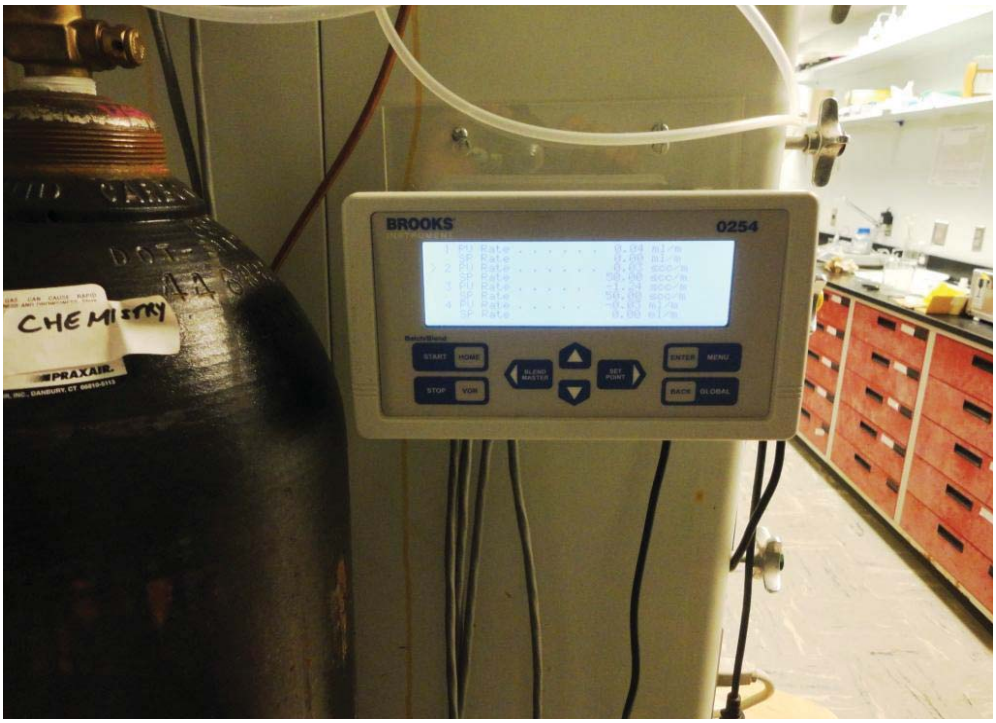

Figure A.11. Mass flow controller module; can control up to 4 gas flows simultaneously

- Mass flow controllers: The flow meters were also supplied by Brooks Instruments. These are designed to be accurate between flows of 5 mL-100 mL/min. The pressure has to be maintained around 20 psi for a stable continuous flow. These were calibrated for carbon dioxide, air, methane and hydrogen. If in any case the gas flow gets obstructed or the pressure drops which can lead to a drop in the gas flow, an alarm will be set off that will cause a red light on the flow meters to blink (Figure A.11).

Figure A.12. Flow meters can control up to 100 mL/min

- Humidification system: The fuel gases were humidified by passing through the humidification assembly shown in Figure A.13. The different percentages of the humidification level were controlled by the partial pressure of the water vapor which is itself is controlled by the temperature. Make-up water to the humidifier was fed from an upper vessel in a “chicken-feeder” orientation, where lowered water level in the lower flask would cause gas displacement through a 0.25 inch plastic tube into the upper vessel, enabling make-up water to flow out.

Figure A.13. Gas humidification system

Hydrogen gas was connected after it had been passed through its respective mass flow connector. Nitrogen was also connected in order to purge before they were fed into the

humidifier. Air was connected to the ProboStat^{TM}after it was passed through its mass flow controller.

APPENDIX A

REFERENCES

1) Hyrel System 30 3D Printer MANUAL Revision 1.3; Hyrel 3D: Norcoss, GA, 2016
2) Retrieved on January 20th 2010, from : http://www.norecs.com/index.php?page=141

APPEDNIX B

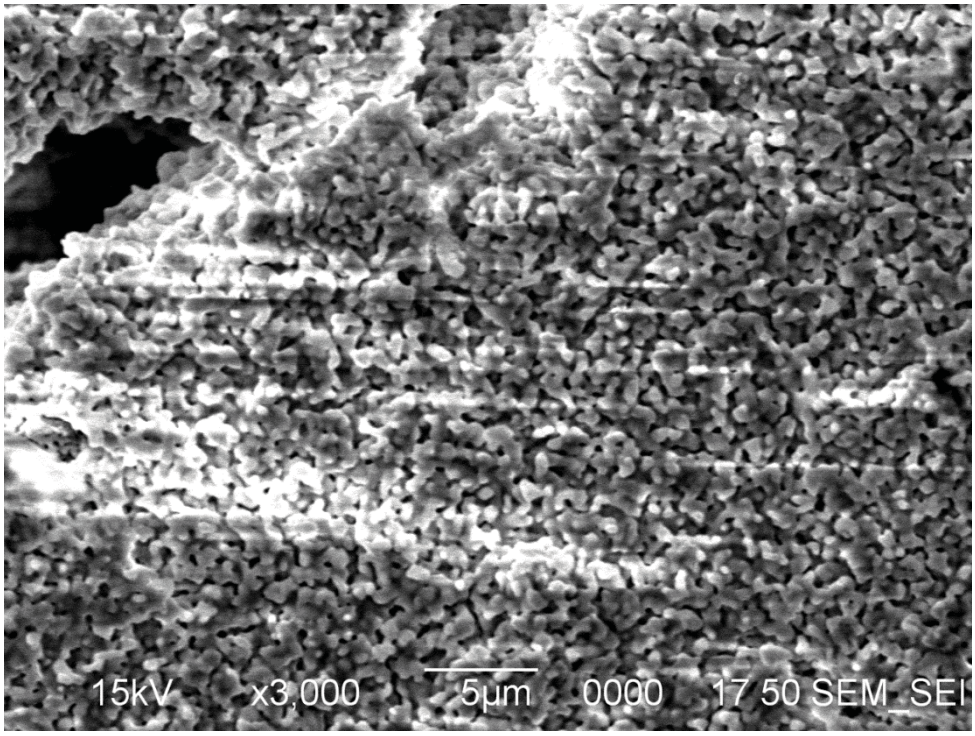

Figure B.3. Sample with 1 % Binder content and 5.5 g of solvent

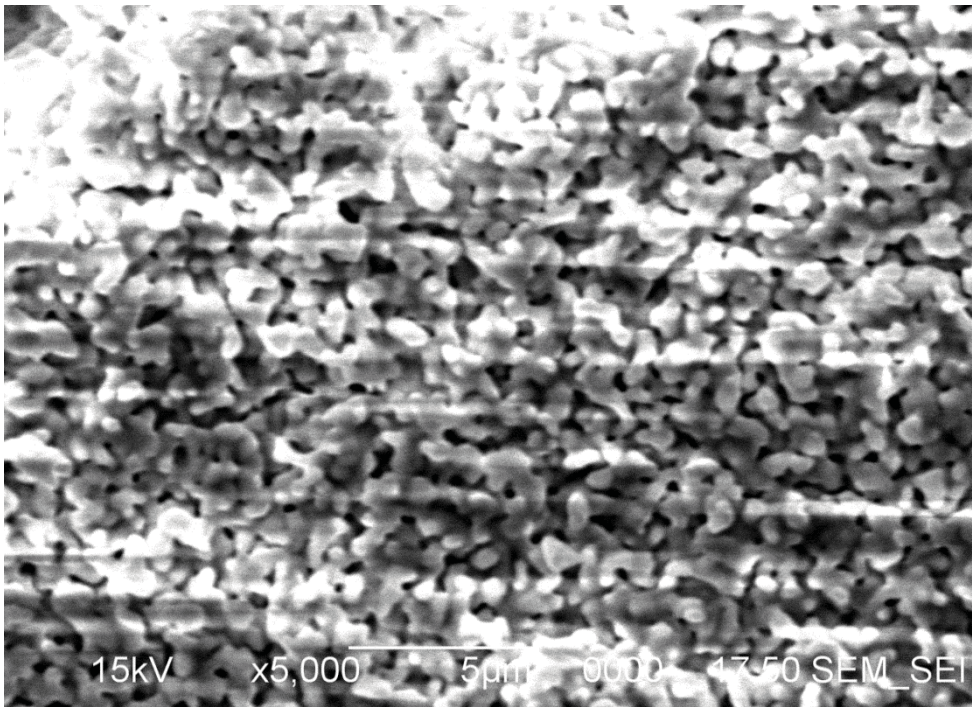

Figure B.2. Sample with 3 % Binder content and 5.5 g of solvent

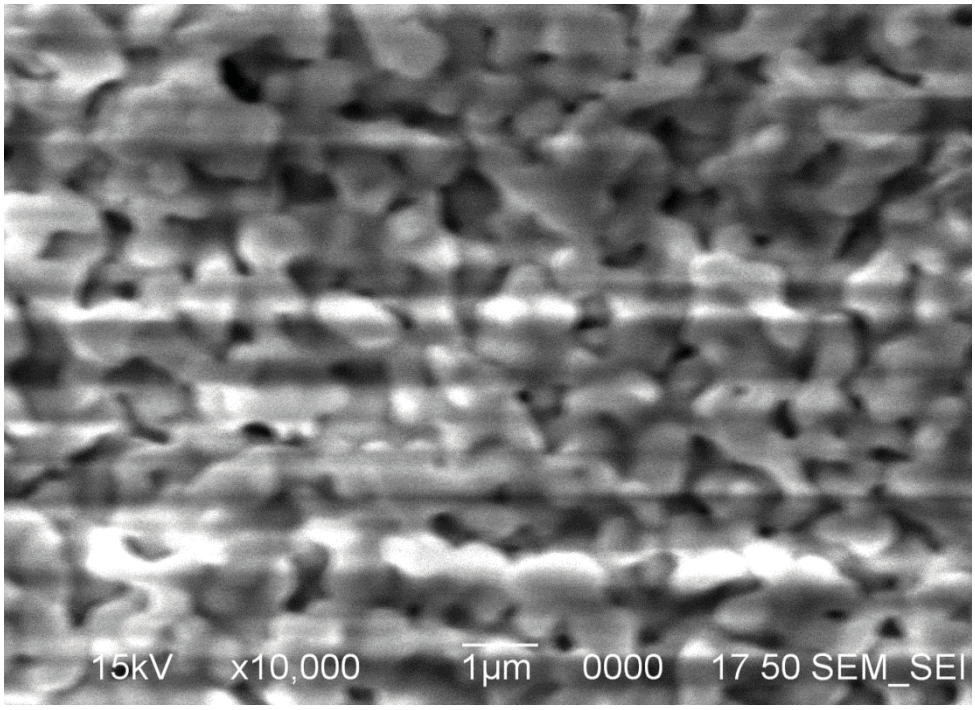

Figure B.3. Sample with 1 % Binder content and 5.5 g of solvent

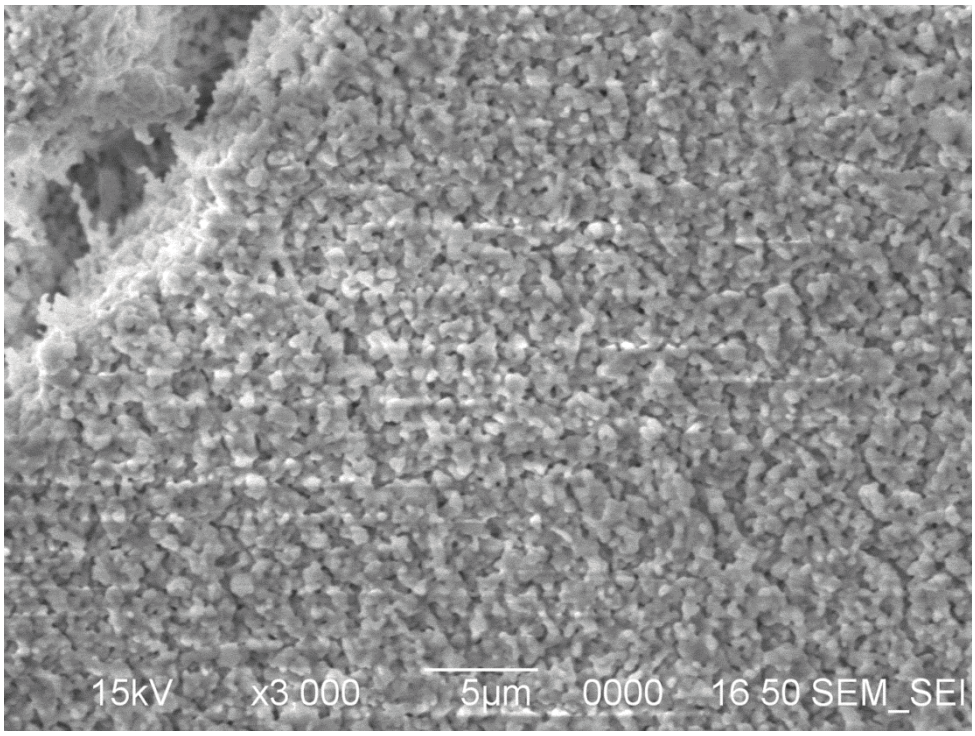

Figure B.4. Sample with 3 % Binder content and 5.5 g of solvent

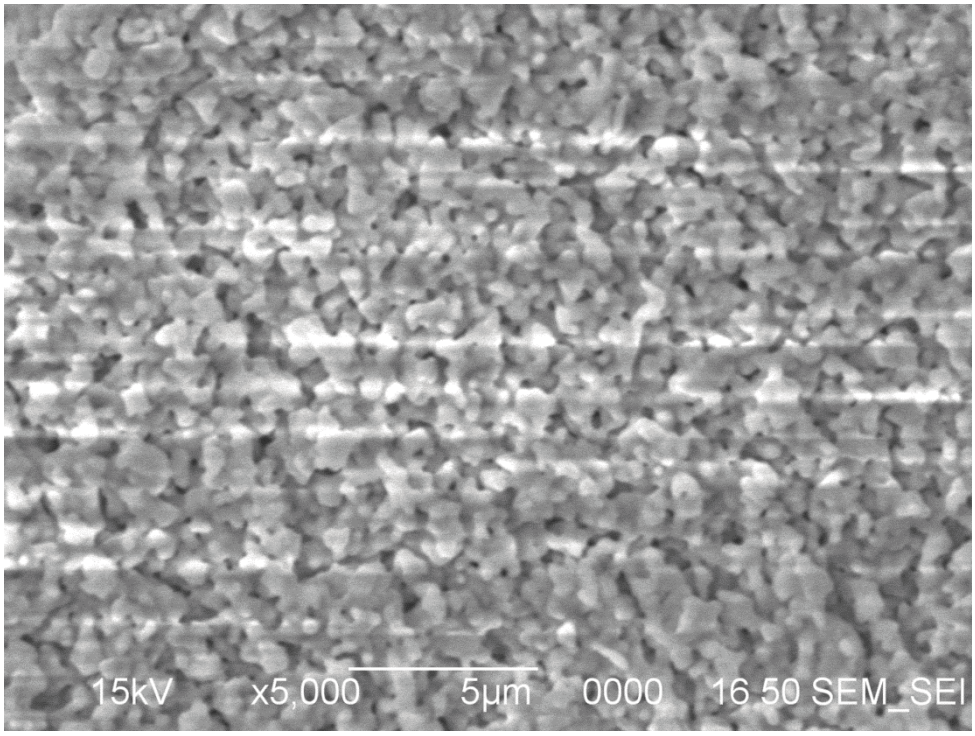

Figure B.5. Sample with 3 % Binder content and 5.5 g of solvent

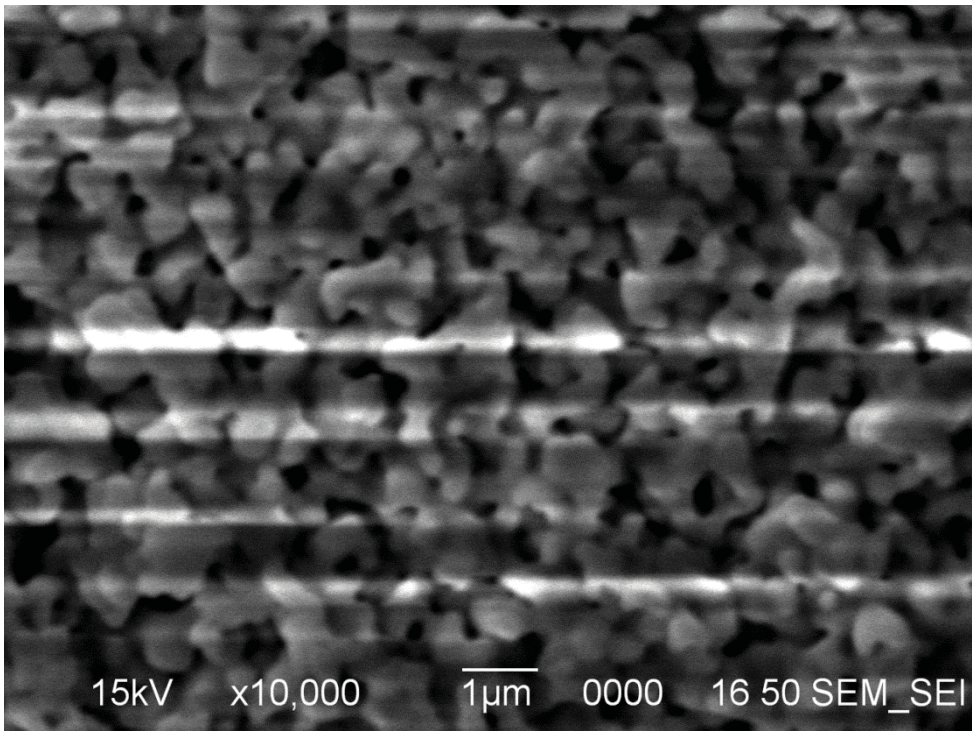

Figure B.6. Sample with 3 % Binder content and 5.5 g of solvent

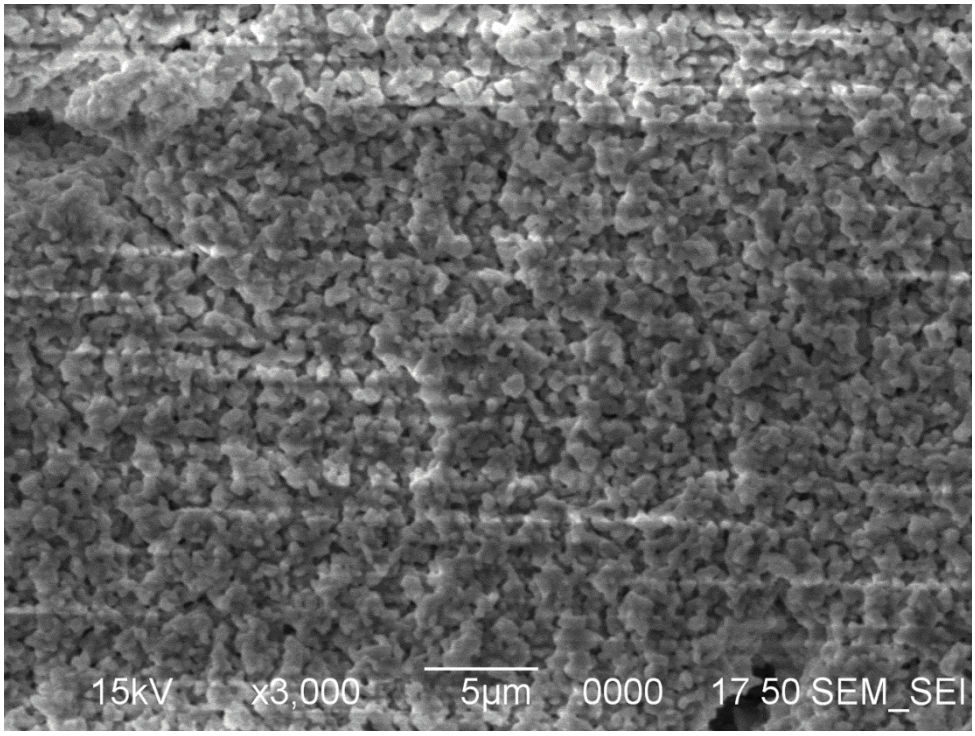

Figure B.7. Sample with 5 % Binder content and 5.5 g of solvent

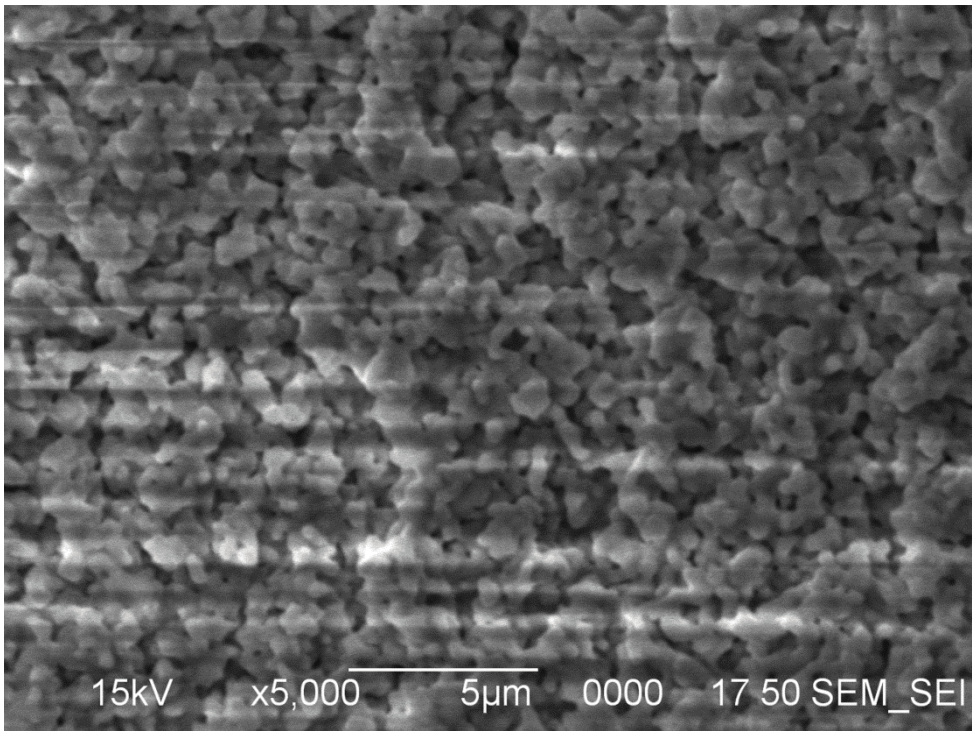

Figure B.8. Sample with 5 % Binder content and 5.5 g of solvent

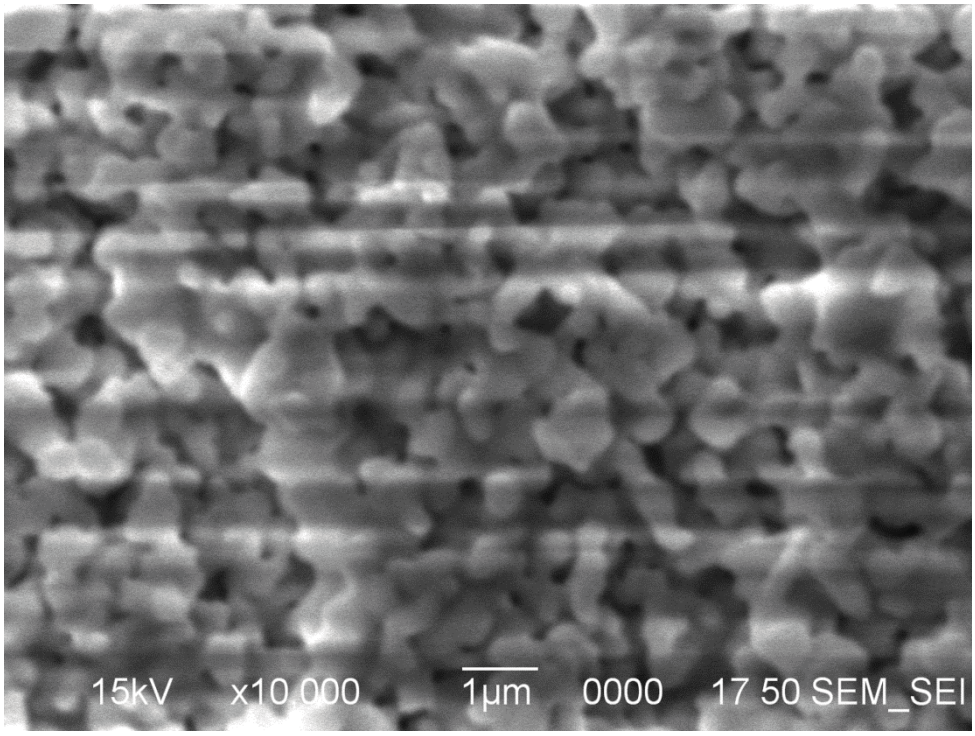

Figure B.9. Sample with 5 % Binder content and 5.5 g of solvent

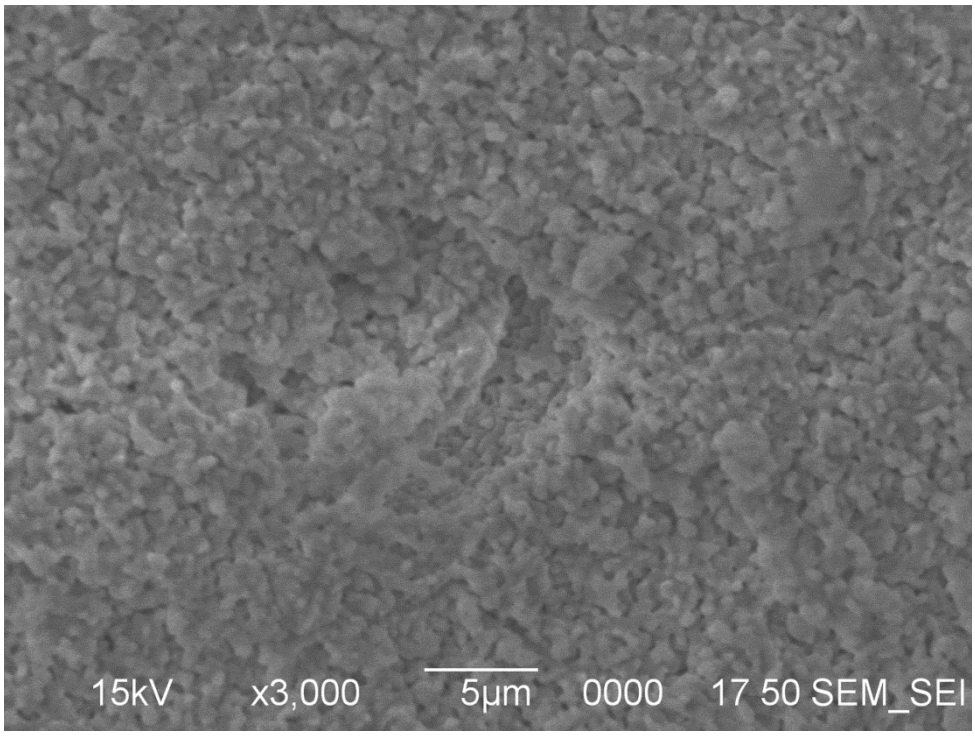

Figure B.40. Sample with 7 % Binder content and 5.5 g of solvent

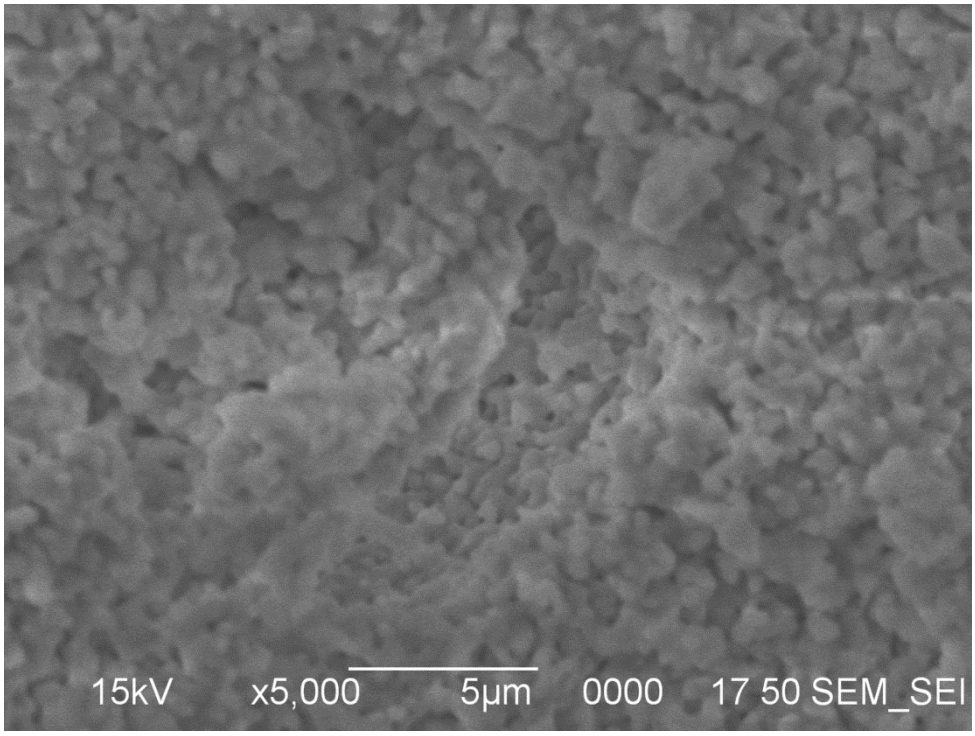

Figure B.51. Sample with 7 % Binder content and 5.5 g of solvent

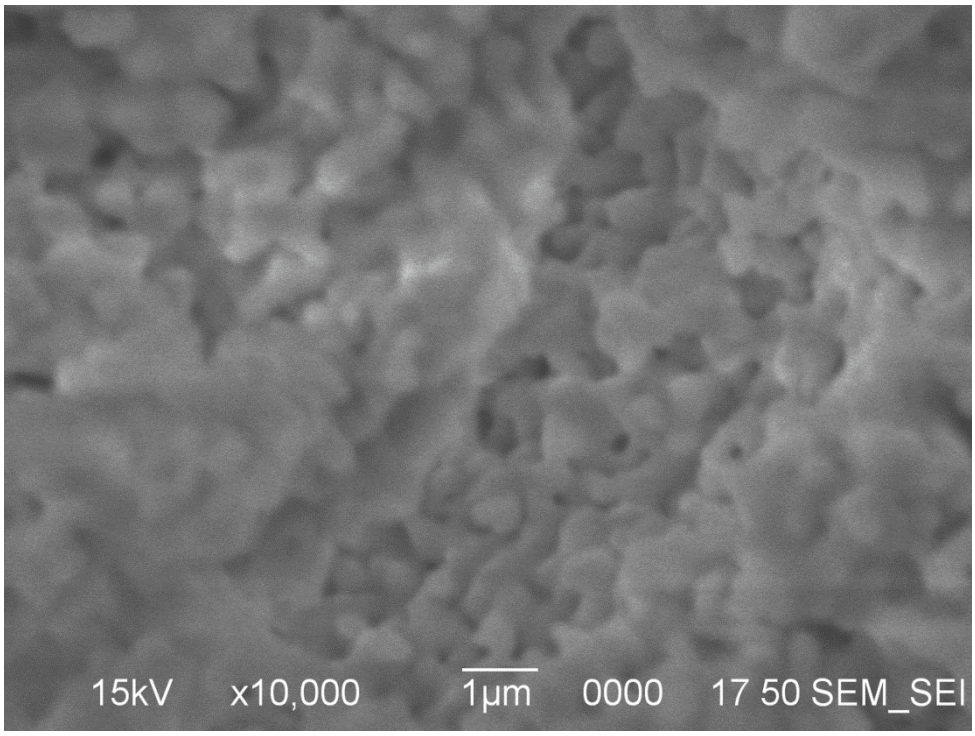

Figure B.62. Sample with 7 % Binder content and 5.5 g of solvent

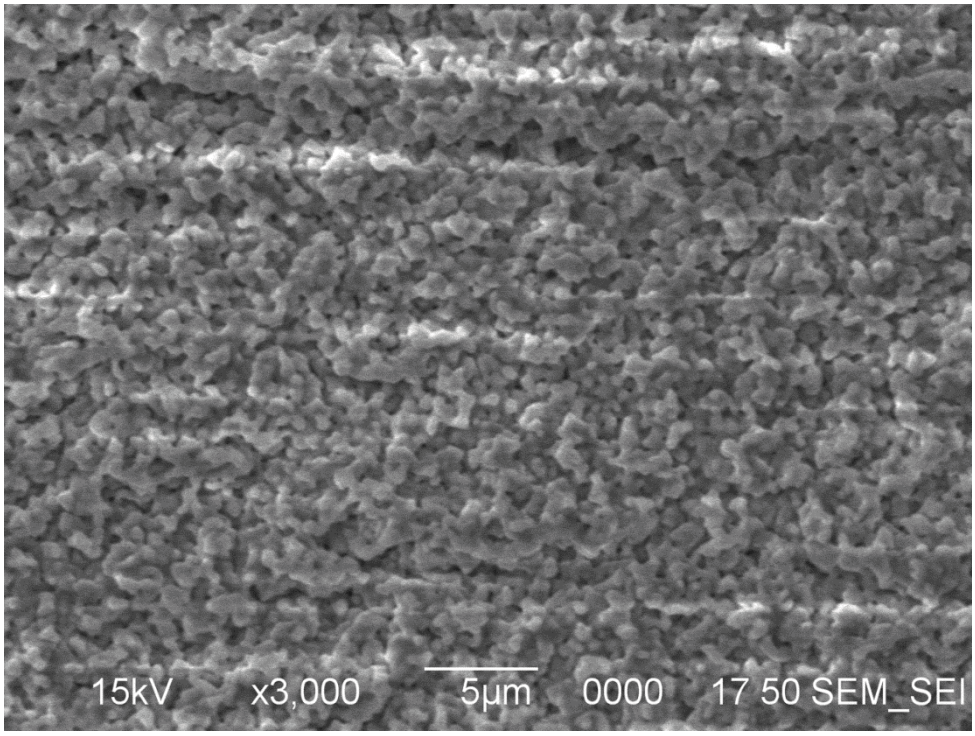

Figure B.73. Sample with 9 % Binder content and 5.5 g of solvent

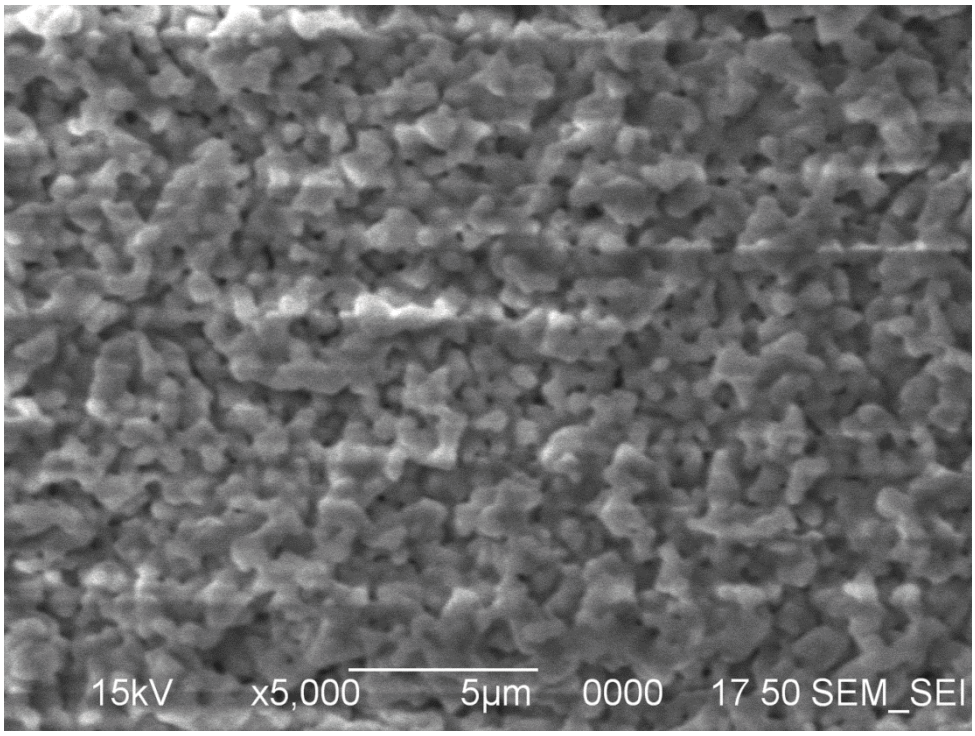

Figure B.84. Sample with 9 % Binder content and 5.5 g of solvent

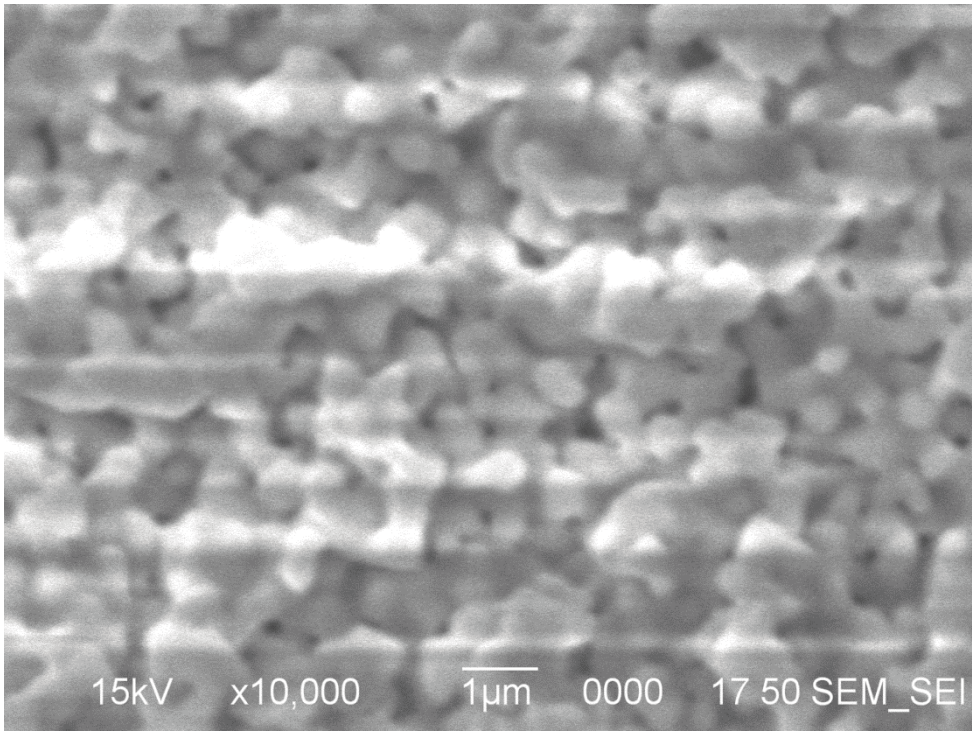

Figure B.95. Sample with 9 % Binder content and 5.5 g of solvent

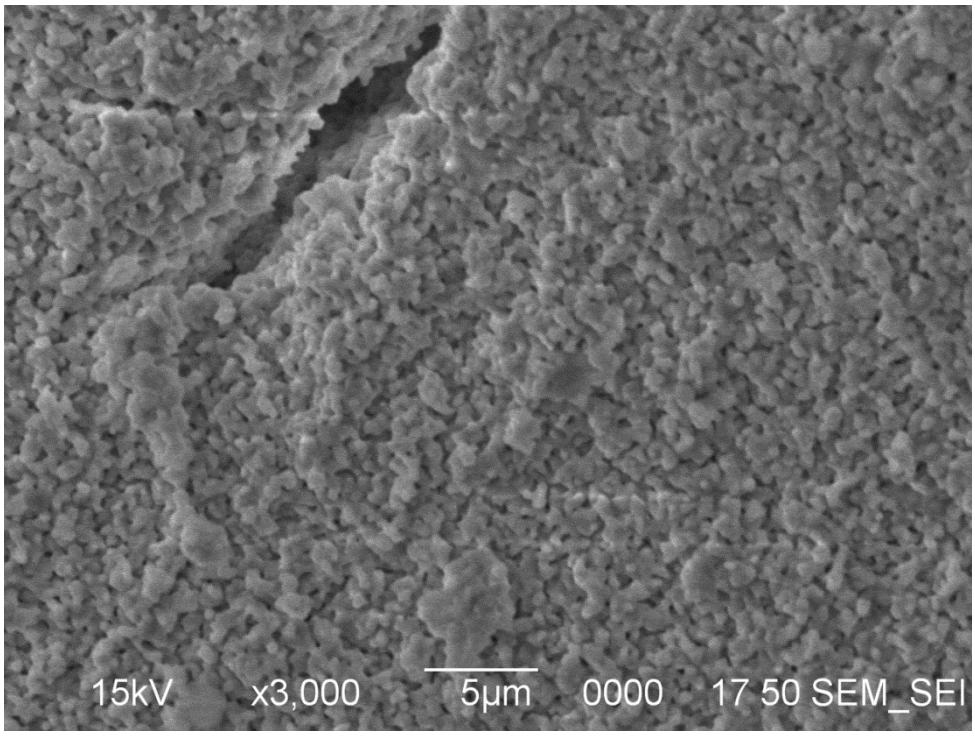

Figure B.106. Sample with 3 % Binder content and 4.0 g of solvent

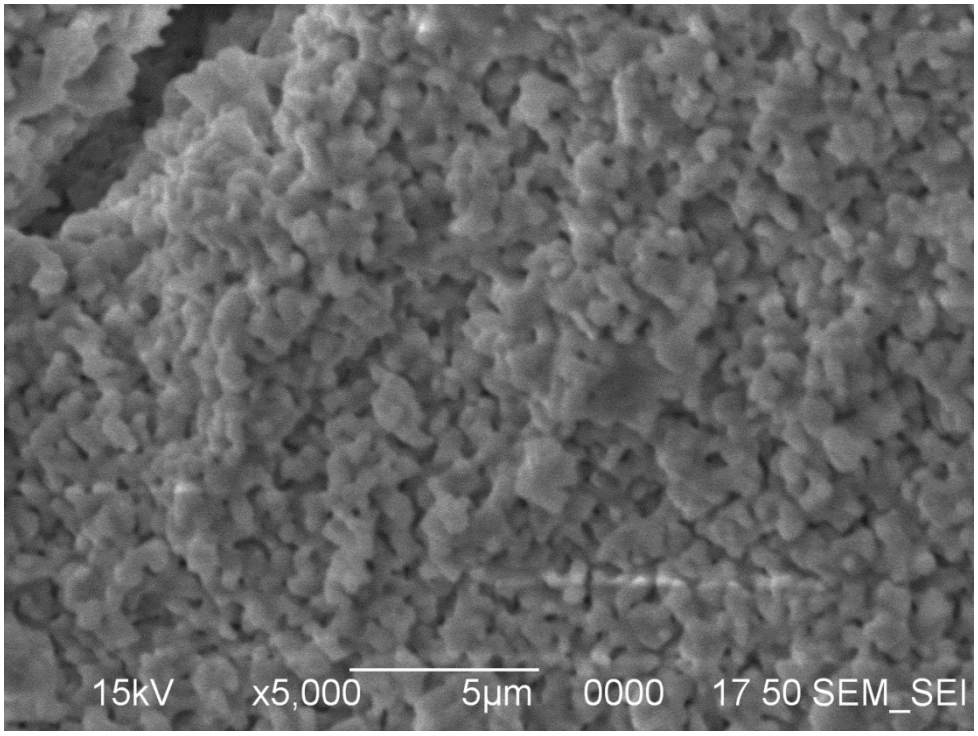

Figure B.116. Sample with 3 % Binder content and 4.0 g of solvent

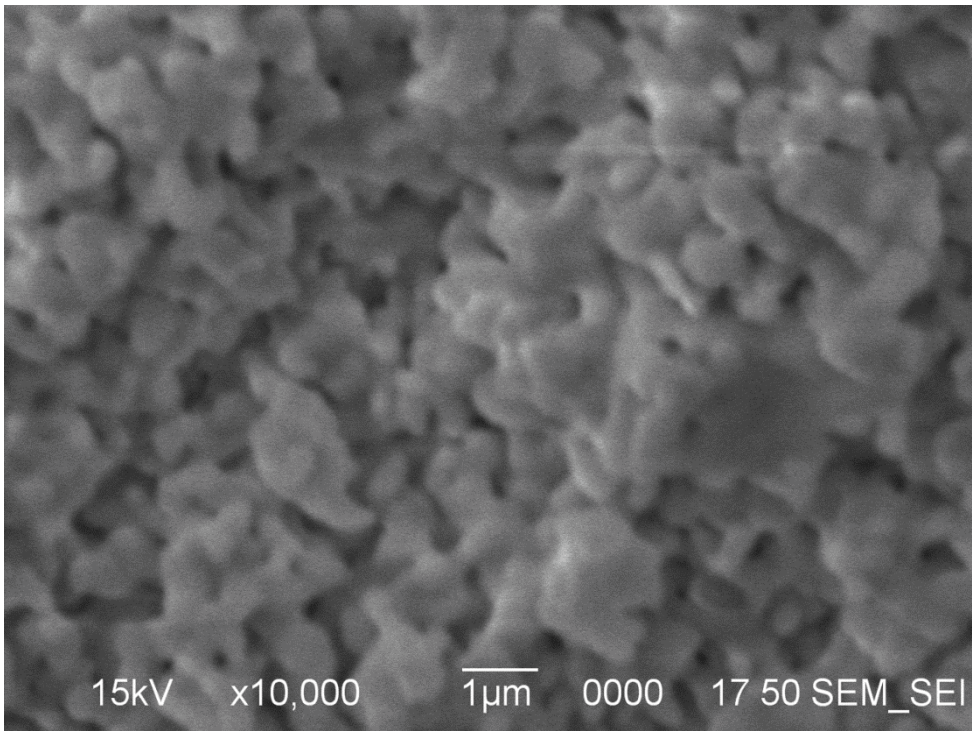

Figure B.126. Sample with 3 % Binder content and 4.0 g of solvent

APPENDIX C

INTERCONNECT STUDY

A-site deficiency of the LSM improves the sinterability and results in improved lamination to the electrolyte. A site deficiency of 0.5 % prevents the formation of the insulating layer of lanthanum zirconate to be formed. A-site deficiency in LSM enhances its densification. $(La_{.65}Sr_{.35})_{.95}MnO_3$ when sintered at 1385 ^0C showed high densification. The conductivity of LSM is about 200 S/cm.

LSM samples were prepared by using salts of lanthanum, strontium and manganese. Several methods were analyzed by Sefir et al. (2) for the preparation of LSM and Bell et al. (1) studied the effect of those methods on the catalytic activity of LSM. These studies both implied that the carbonate co-precipitation synthesis route delivered a more homogenous finer powder.

In this study, attempts were made to copercipitate LSM with various salts, calcined and analyzed using XRD.

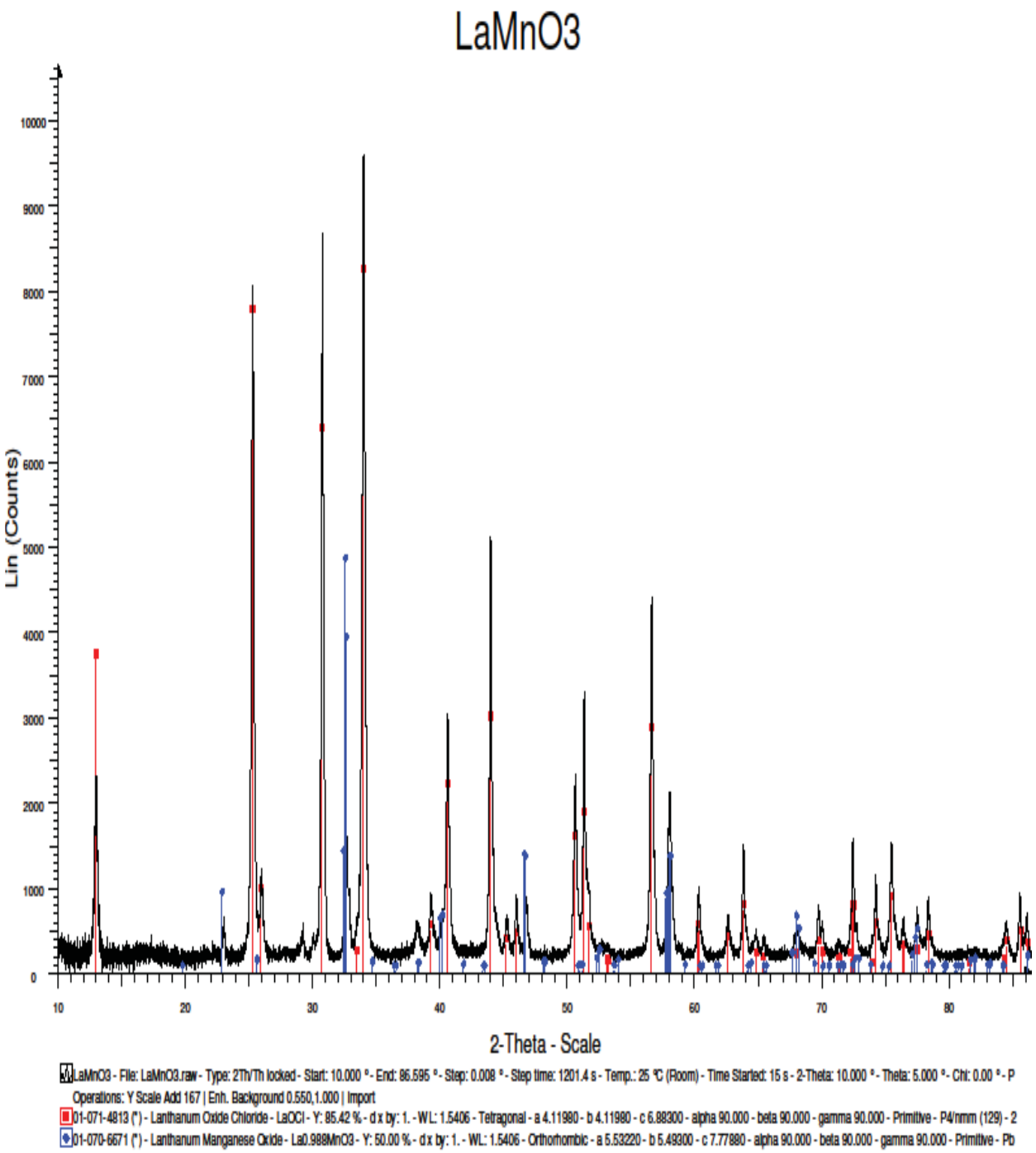

Figure 13. The presence of LaOCl phases when chloride salts were used for precipitation

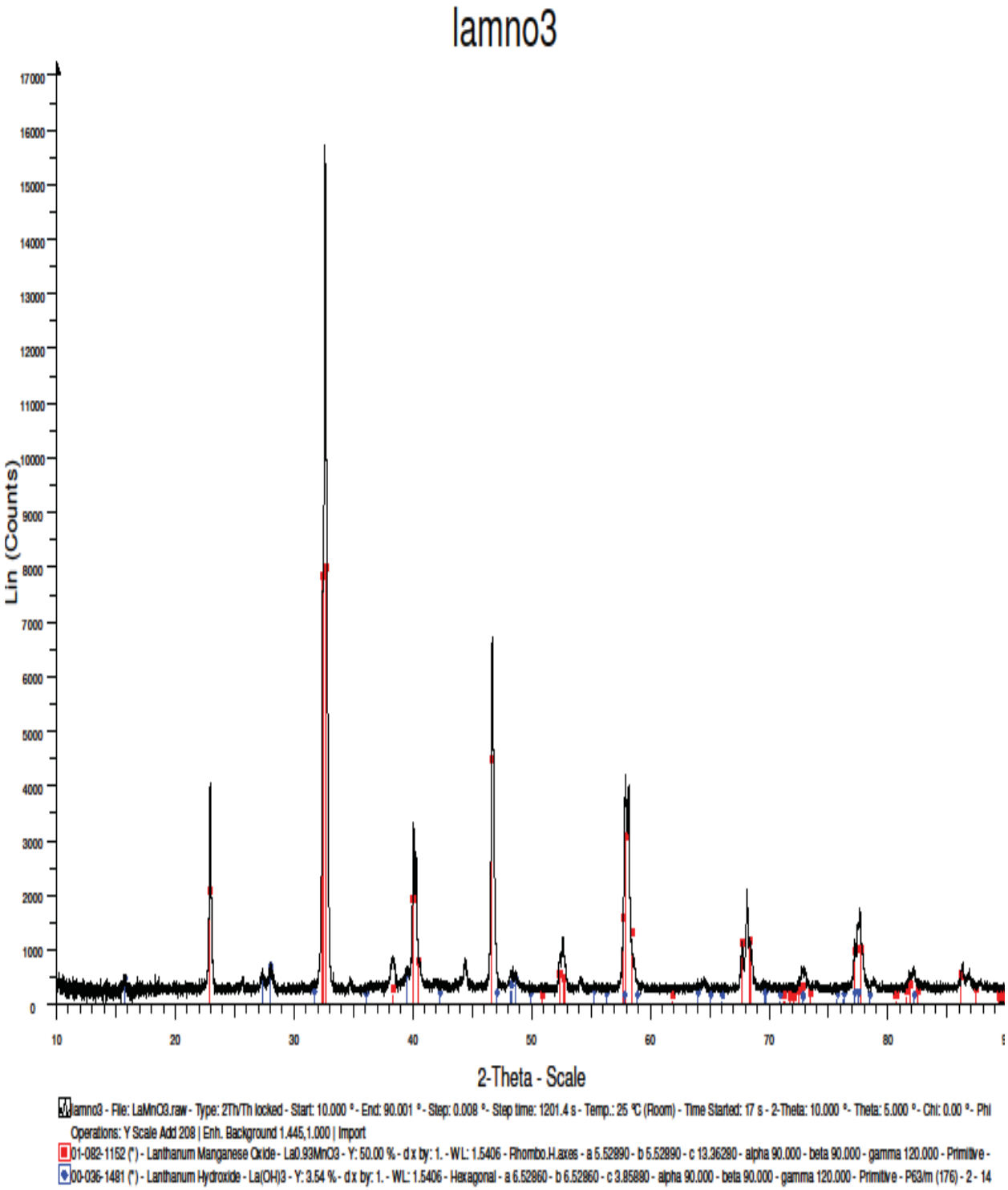

Figure 14. Presence of La(OH) at 1000 °C

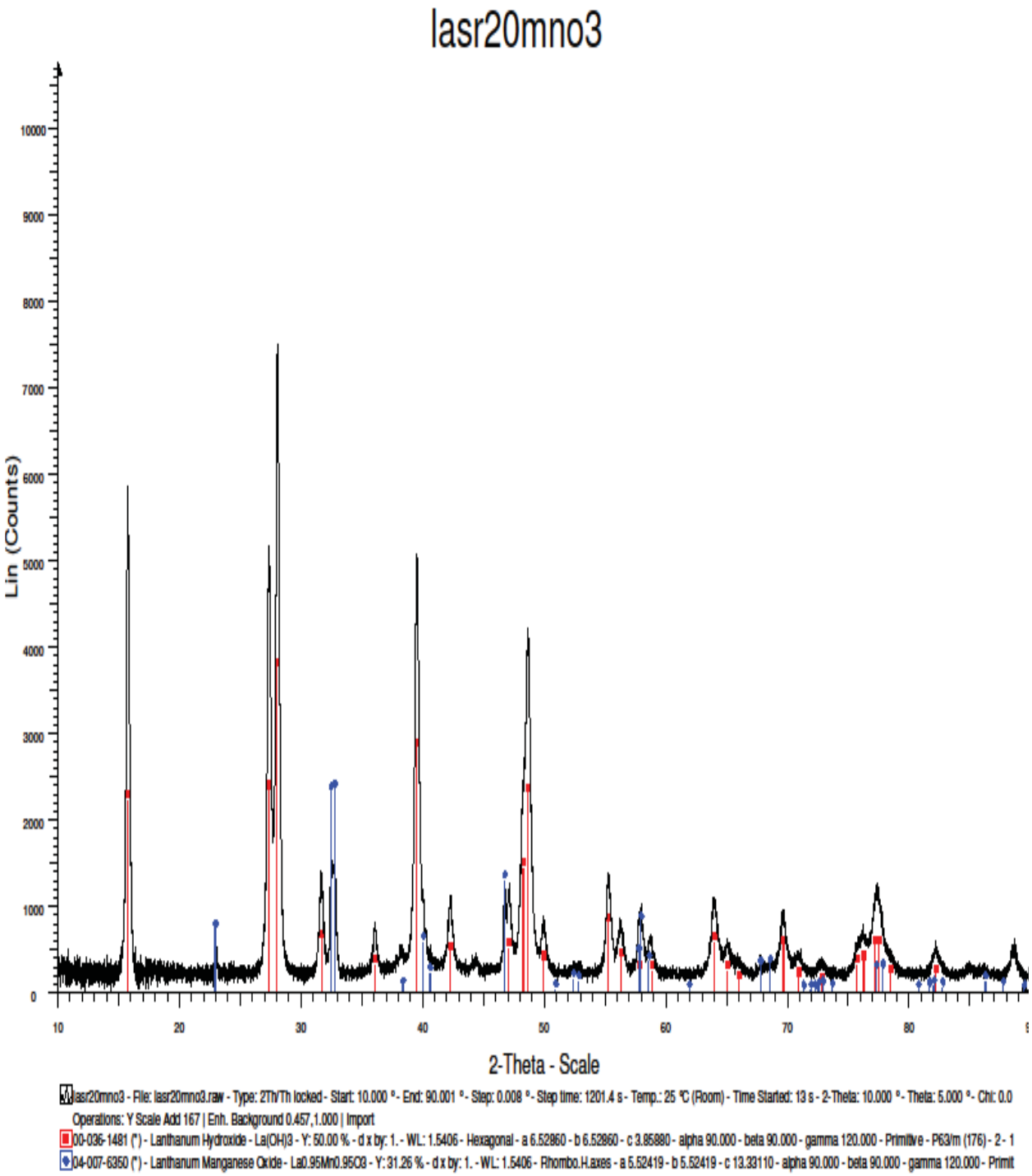

Figure 15. La(OH) present in sample, calcined at 1100 °C

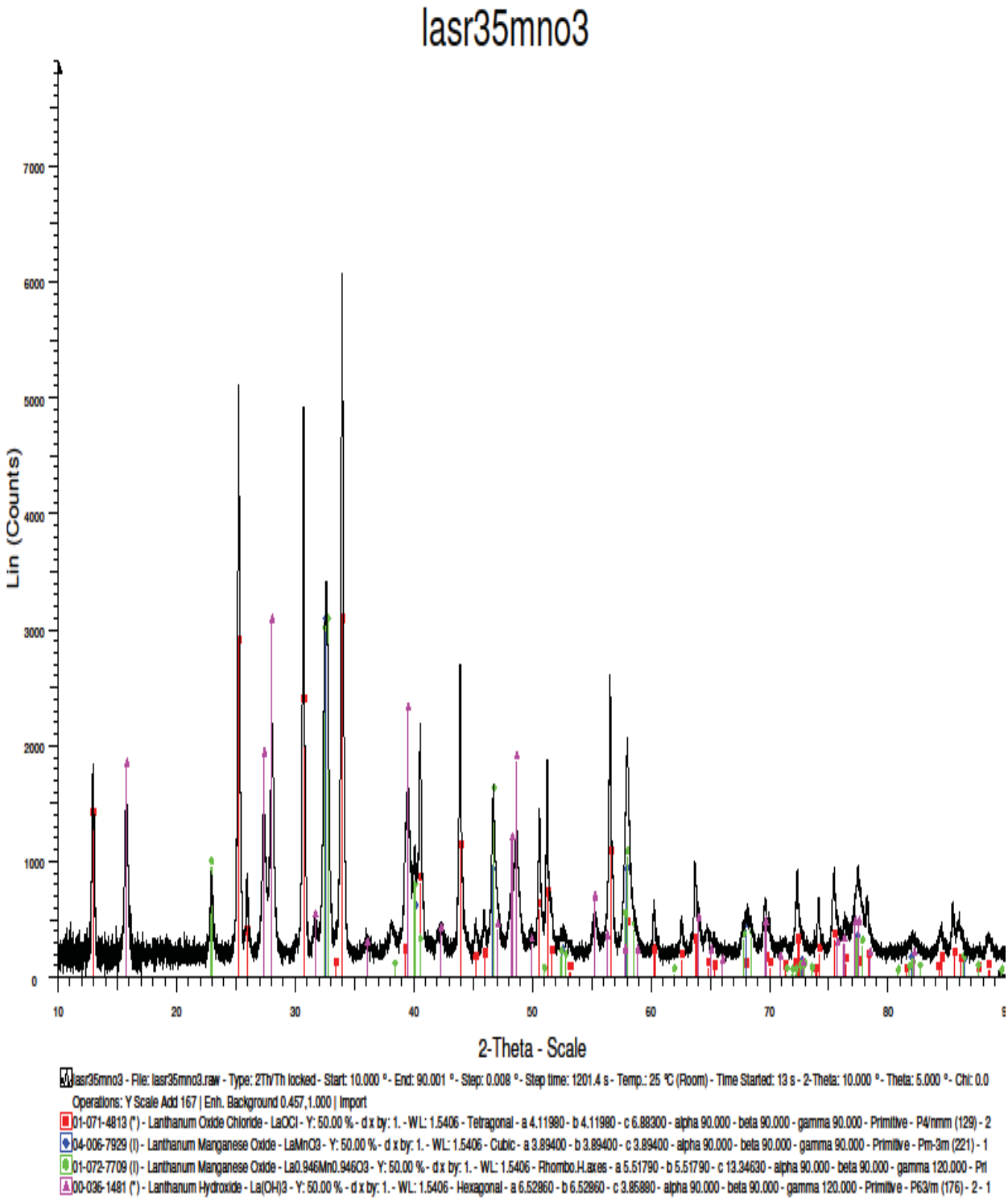

Figure 16. Presence of $La(OH)_3$ at calcination temperature of 1200 ^oC

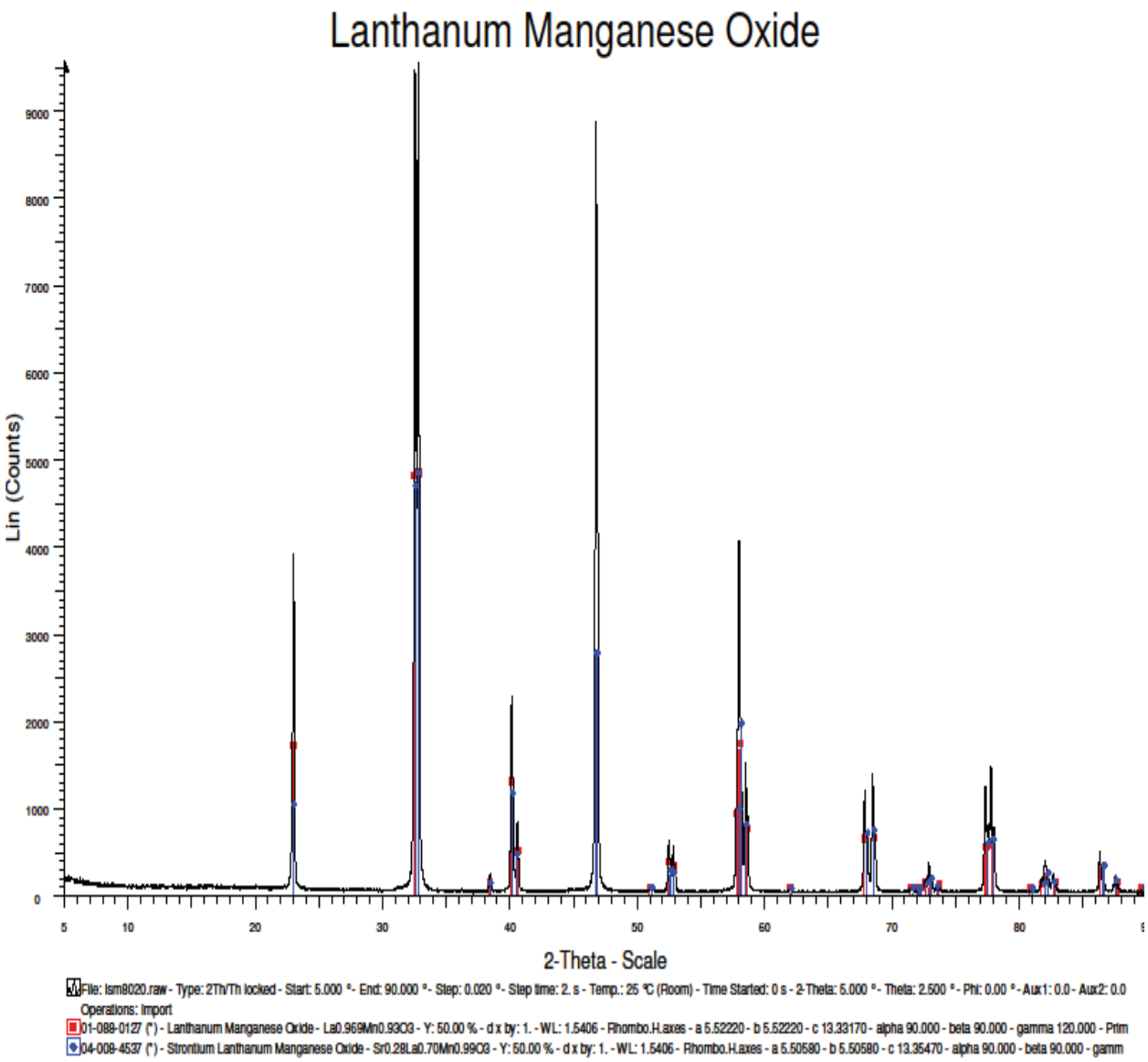

Figure 17. No unwanted phases present when calcination temperature was increased to 1300 °C

APPENDIX C

REFERENCES

1. Influence of Synthesis Route on the Catalytic Properties of La1−xSrxMnO3." Influence of Synthesis Route on the Catalytic Properties of La1−xSrxMnO3.
2. Sfeir, J., S. Vaucher, P. Holtappels, U. Vogt, H.-J. Schindler, J. Van Herle, E. Suvorova, P. Buffat, D. Perret, N. Xanthopoulos, and O. Bucheli. "Characterization of Perovskite Powders for Cathode and Oxygen Membranes Made by Different Synthesis Routes." Journal of the European Ceramic Society 25.12 (2005): 1991-995